Properties of the nanocrystalline layers obtained by methods of severe plastic deformation in metals and alloys for biomedical applications

Konrad Skowron

Thesis submitted for the Degree of Doctor of Philosophy
in Physics Prepared under the supervision of:

dr hab. Ewa Dryzek The Henryk Niewodniczański Institute
of Nuclear Physics Polish Academy of Sciences

and

dr hab. Michał Mosiałek Jerzy Haber Institute of Catalysis
and Surface Chemistry Polish Academy of Sciences

Kraków 2021

InterDokMed

Rozprawa doktorska powstała w trakcie realizacji
Środowiskowych Studiów Doktoranckich
w ramach Projektu nr POWR.03.02.00-00-I013/16,
"Interdyscyplinarność dla medycyny innowacyjnej" InterDokMed,
realizowanych w ramach Programu Operacyjnego Wiedza Edukacja Rozwój 2014-2020,
współfinansowanego ze środków Europejskiego Funduszu Społecznego

Fundusze Europejskie
Wiedza Edukacja Rozwój

Unia Europejska
Europejski Fundusz Społeczny

Acknowledgments

Foremost, I would like to express my sincere gratitude to my thesis supervisor dr hab. Ewa Dryzek for her patience, constructive criticism, and motivation. Her guidance helped me in all the time of research and writing of this thesis.

I would also like to thank my co-supervisor, dr hab. Michał Mosiałek, for his help, comments, and expertise that greatly assisted the research.

I would like to express my deep gratitude to prof. Paweł Nowak for acquainting me with the subject of metal corrosion and for his invaluable help in creating this dissertation.

I am also grateful to dr hab. Mirosław Wróbel for recording EBSD images and carrying microhardness tests.

I would thank my family, especially my bellowed wife Kinga and son Jan for their patience during the last months of my Ph.D. studies when the dissertation preparation was consuming all my time.

Abstract

Due to the increasing demand for durable materials that can be used in the production of prosthetics, biometals have been attracting much interest in recent years. There can be seen great scientific activity in the field of improving the properties and service time of human body implants. Implant failure usually begins on its surface as a result of fatigue, wear, or corrosion. However, the destruction process can be slowed down by the application of appropriate surface modification techniques which lead to the formation of a nanocrystalline structure on the surface of the implant. Especially, those based on severe plastic deformation are popular nowadays. The application of these methods results in the creation of an ultrafine-grained structure, as well as, a great number of crystal lattice defects which introduction greatly changes the properties of the material. Despite continuous efforts in understanding the corrosion process, the impact of the presence of crystal lattice defects is still not understood completely. That is why there is a need for interdisciplinary research which combines physics, materials science, and electrochemistry for better understanding the corrosion response of nanocrystalline materials.

The main objective of the presented thesis is to study how the presence of crystal lattice defects introduced during severe plastic deformation is correlated with the properties of biometals, especially their corrosion resistance. The subject of the present research are gradient microstructures with nanocrystalline top layers generated by surface mechanical attrition treatment (SMAT) and laser shock peening (LSP) in biometals such as magnesium, titanium, and 316L stainless steel. The thesis has got an interdisciplinary character and it combines physics with materials science and electrochemistry. The positron annihilation spectroscopy, which is the main research method of the present work, is combined with microhardness tests, electron backscatter diffraction, X-ray diffraction, surface roughness tests with an optical profilometer, and corrosion resistance tests to evaluate the impact of SMAT and LSP on the properties of the materials studied.

The use of positron annihilation spectroscopy allowed obtaining defect depth distributions in the deformed surface layers which were compared with the observed microstructure, microhardness profiles, and residual stresses. It was demonstrated that SMAT improved corrosion resistance of magnesium and titanium and the correlation between the defect concentration and corrosion resistance of the materials studied was found. The temperature stability measurements of the SMATed titanium samples and the ultrafine-grained ones prepared with the use of hydrostatic extrusion revealed two stages of defect annealing.

Streszczenie

Ze względu na rosnące zapotrzebowanie na trwałe materiały, które mogą zostać wykorzystane do produkcji protez, biometale cieszą się w ostatnich latach dużym zainteresowaniem. Można zaobserwować dużą aktywność naukową w zakresie poprawy właściwości i trwałości implantów stosowanym w ludzkim ciele. Uszkodzenie implantu zwykle zaczyna się na jego powierzchni w wyniku zmęczenia, zużycia lub korozji. Proces niszczenia można jednak spowolnić poprzez zastosowanie odpowiednich technik modyfikacji powierzchni, które prowadzą do powstania struktury nanokrystalicznej na powierzchni implantu. Szczególnie popularne stały się dziś te oparte na silnym odkształceniu plastycznych. Zastosowanie tych metod skutkuje powstaniem ultradrobnoziarnistej struktury, a także dużej liczby defektów sieci krystalicznej, których wprowadzenie znacznie zmienia właściwości materiału. Pomimo ciągłych wysiłków zmierzających do zrozumienia procesu korozji, wpływ defektów sieci krystalicznej wciąż nie jest do końca poznany. Dlatego potrzebne są badania interdyscyplinarne, łączące fizykę, materiałoznawstwo i elektrochemię w celu lepszego zrozumienia odporności korozyjnej materiałów nanokrystalicznych.

Głównym celem niniejszej pracy jest zbadanie, w jaki sposób obecność defektów sieci krystalicznej wprowadzanych podczas silnego odkształcenia plastycznego jest skorelowana z właściwościami biometali, a zwłaszcza ich odpornością korozyjną. Przedmiotem badań są gradientowe mikrostruktury z nanokrystalicznymi warstwami wierzchnimi, wytworzonymi przy pomocy powierzchniowej obróbki mechaniczno ściernej (SMAT) oraz peeningu laserowego (LSP) w biometalach takich jak magnez, tytan i stal nierdzewna 316L. Praca ma charakter interdyscyplinarny i łączy fizykę z materiałoznawstwem i elektrochemią. Spektroskopię anihilacji pozytonów, która jest główną metodą badawczą niniejszej pracy, połączono z badaniami mikrotwardości, dyfrakcją wstecznie rozproszonych elektronów, dyfrakcją rentgenowską, badaniami chropowatości powierzchni za pomocą profilometru optycznego oraz badaniami odporności na korozję w celu oceny wpływu SMAT oraz LSP na właściwości badanych materiałów.

Zastosowanie spektroskopii anihilacji pozytonów pozwoliło uzyskać głębokościowe rozkłady defektów w zdeformowanych warstwach powierzchniowych, które porównano z obserwowaną mikrostrukturą, profilami mikrotwardości oraz wartościami naprężeń. Wykazano, że SMAT poprawia odporność korozyjną magnezu i tytanu oraz stwierdzono korelację między koncentracją defektów, a odpornością korozyjną badanych materiałów. Pomiary stabilności temperaturowej próbek tytanu poddanemu SMAT i przygotowanych metodą wyciskania hydrostatycznego ujawniły dwa etapy wyżarzania defektów.

Table of contents

List of abbreviations

AMP - amplifier
ARB - accumulative roll-bonding
CE - counter electrode
CFD - constant fraction discriminators
cp - commercial purity
CPE - constant phase element
CVD - chemical vapor deposition
DB - Doppler broadening
DL - delay line
EBSD - electron backscatter diffraction
ECAP - equal channel angular pressing
EDS - energy dispersive spectroscopy
EEC - equivalent electric circuits
EIS - electrochemical impedance spectroscopy
fcc - face-centered cubic
FWHM - Full Width at Half Maximum
hcp - hexagonal close-packed
HE - hydrostatic extrusion
HpGe - High-purity Germanium
HPT - high-pressure torsion
HRWB - high-speed rotation wire-brushing
LSP - laser shock peening
LSPwC – laser shock peening without coating
LSV - linear sweep voltammetry
MCA - multichannel analyzer
MGXID - multireflection grazing-incidence X-ray diffraction
NC - nanocrystalline
Nd: YAG - Neodymium-doped Yttrium Aluminum garnet
OCP - open circuit potential
PALS - positron annihilation lifetime spectroscopy
PAS - positron annihilation spectroscopy
PET - positron emission tomography
PM - photomultiplier tubes
PVD - physical vapor deposition
RE – reference electrode
PEO - plasma electrolytic oxidation
SC - scintillation counter
SCE - saturated calomel electrode
SEM - scanning electron microscopy
SMAT – surface mechanical attrition treatment
SN - surface nanocrystallization
SPD - severe plastic deformation
SSMR - super short multi-pass rolling
SSN - surface self-nanocrystallization
TAC - time-amplitude converter
TEM - transmission electron microscope

USSP - ultrasonic sonic shot peening
VEP - variable energy positron
WE - working electrode
W-H - Williamson-Hall

Introduction

In the face of an increasingly aging society, there is a growing interest in safe and durable materials, as well as, the methods of their production, that can be used in prosthetics. The surface properties of orthopedic implants are very important for clinical reasons. Implant failure usually begins on its surface as a result of fatigue, wear, or corrosion. The destruction process can be slowed down by the application of various surface modification methods, i.e., those that lead to the formation of a nanocrystalline structure on the implant surface. These types of layers can be obtained by methods such as physical vapor deposition (PVD), chemical vapor deposition (CVD), or plasma electrolytic oxidation (PEO), but the strength of their bonding with the substrate may be not sufficient.

The methods of producing nanocrystalline layers that have been gaining popularity in recent years are those based on severe plastic deformation (SPD). In contrast to the layers obtained by the methods mentioned above, layers obtained by the SPD are better bonded to the substrate. These methods consist of introducing large plastic deformation into the material to create an ultrafine-grained layer. It is well known that the production of fine-grained microstructure in metals can improve their overall physical and mechanical properties. The main purpose of the application of SPD-based methods is the production of durable materials with a high strength-to-weight ratio. Various techniques based on SPD that modify the entire volume of the processed material, such as equal channel angular pressing (ECAP) or hydrostatic extrusion (HE), as well as those based on the shot peening (SP) of the target surface have been developed. These methods are carried out without changing the chemical or phase composition of the material and can be called self-nanocrystallization methods. In recent years, SP-based methods have become popular due to their simplicity and ease of use. Examples of such methods are the surface mechanical attrition treatment (SMAT) and the laser shock peening (LSP) which have been developed in the last few years.

Application of SMAT allows the creation of a hard gradient nanocrystalline microstructure underneath the treated surface. The method has the same features as conventional SP. However, differences such as, e.g., the size and shape of the shots and the device used to propel the shots in the SMAT result in different characteristics and mechanical properties of the surface microstructure produced in comparison to conventional SP.

In LSP, laser pulses are used to heat and ionize the surface of the workpiece or the ablative layer on its surface. Repeated laser pulses on the surface of the workpiece or the ablation layer convert them into rapidly expanding plasma, which generates high pressure on the surface, and as a consequence, a shock wave in the target material. The application of the method leads to the formation of an ultrafine-grained gradient structure under the treated surface.

A great scientific effort is being put into researching and collecting the most accurate information on the influence of the treatment methods on the structure and properties of metals used in biomedicine. For this purpose, a variety of methods are used, e.g., a scanning or transmission electron microscope, X-ray diffraction (XRD), or methods based on neutron scattering. Application of the SPD methods leads to changes in the density and type of defects inside the workpiece, which spatial distribution after deformation is heterogeneous. Defects, especially vacancies, and their clusters or dislocations can be tracked and distinguished using the positron annihilation spectroscopy (PAS) techniques, which are the main measurement methods in this work.

The thesis has got an interdisciplinary character and combines physics and chemistry with materials science. The subject of the present research are metals used in biomedical applications. Gradient microstructure in magnesium, titanium and 316L stainless steel were generated using SMAT at the University of Technology of Troyes in France. Additionally, in cooperation with the Faculty of Metals Engineering and Industrial Computer Science AGH University of Science and Technology in Krakow, LSP was used to generate gradient microstructure in 316L steel. The positron annihilation lifetime spectroscopy (PALS), Doppler broadening (DB) spectroscopy, and variable energy beam (VEP) beam measurements were used to study defect distribution related to this gradient microstructure. The results obtained with these methods have been combined with microhardness tests, electron backscatter diffraction (EBSD), XRD, surface roughness tests with an optical profilometer, and tests of electrochemical properties, in particular corrosion resistance, using methods such as electrochemical impedance spectroscopy (EIS) or linear sweep voltammetry (LSV).

Chapter 1 of the dissertation introduces the subject of materials used in biomedicine, i.e., biometals. Chapter 2 discusses the defects of the crystal lattice structure and issues related to plastic deformation, recovery, and recrystallization. Chapter 3 is devoted to the classification and discussion of SPD methods in metals. This Chapter introduces also SMAT and LSP methods. The next Chapter describes the interaction of positron with the matter, as well as, the standard trapping model and PAS techniques, incl. DB spectroscopy, PALS, and VEP measurements. Chapter 5 shows the most important issues related to the phenomenon of corrosion in metals and methods of its evaluation. Chapter 6 presents the usefulness of PAS for tracing the microstructural changes introduced in the subsurface layer of metal during mechanical treatments. Chapters 7, 8, 9 are devoted to the interdisciplinary studies of gradient nanocrystalline microstructures created in magnesium, 316L stainless steel, and titanium respectively. These Chapters combine the results obtained with the PAS with the results of complementary methods and corrosion tests. The last Chapter shows the results of studies of the thermal stability of nanocrystalline titanium and stainless steel produced by SPD techniques.

Chapter 1: Biometals

The materials that are the subject of studies in this are introduced in this Chapter. A broader view of some possible applications of these materials, in particular, magnesium and titanium is also briefly discussed.

Bone-related disorders are one of the major human health problems, which leads to disability, increased morbidity, and reduction of the quality of life, especially among elder patients [1]. Hard tissues are often damaged in accidents or due to aging and are commonly substituted with artificial replacements made of biomaterials. One of the most frequently performed surgical procedures are bone-related, e.g., knee replacements and total hip replacements [2,3]. It is expected that development efforts on biomaterials will accelerate in the upcoming years [1 4]. Biomaterials can be defined as artificial or natural materials, which are used as implants, to replace lost or damaged soft and hard tissues to restore their primary functionality or form [4 5].

For the production of human body implants, different metals and alloys, ceramics (e.g. alumina, zirconia, hydroxyapatite), polymers (e.g. polyamides, polyesters, hydrogels), and composites (e.g. glass fibers) are used. It has been estimated that approximately 70%–80% of implants are made of metallic materials [6]. The first attempts of applications of metal-made implants can be dated to the end of the 19th century [4]. The brief history of development efforts on metal-made implants can be found in the work of Navarro et al. [7].

Properties of metals, such as thermal and electrical conductivity, the ease of their shaping in desired forms, made them excellent candidates for biomedical uses. According to Kiaie et al. [8], the following examples of metals for biomedical applications can be given: elements such as iron (Fe), chromium (Cr), cobalt (Co), nickel (Ni), titanium (Ti), tantalum (Ta), niobium (Nb), molybdenum (Mo), and tungsten (W) and their alloys such as 316 L stainless steel, titanium-based alloys such as [Ti 6%Al 4%V], cobalt-chromium alloys such as [Cr (27–30%), Mo (5–7%), Ni (2.5%)] and [Cr (19–21%), Ni (33–37%), and [Mo (9–11%)], shape memory alloys such as [Ti 45%-55%Ni]. Biometals serve mainly as base materials for hard tissue substitutions, and they dominated orthopedics, used as permanent (e.g., total joint replacement) and temporary (e.g., screws) implants [9,10]. Metals are also used in dental and orthodontic applications, e.g. braces and tooth fillings [11]. Concurrently, metals have also found applications in reconstructive surgery of organs, e.g., NiTi alloy is used in the production of vascular stents [12]. One more group that is gaining great interest lately is biodegradable, temporary implants [13]. The implant slowly dissolves while healed tissues regain their primary functionality. Their application in specific cases may eliminate the need and the risk for a patient of a second surgery to remove the implant. Hence, resorbable materials, such as magnesium and its alloys are gaining significant attention.

Metal-made implants used in orthopedics, should have a wide range of properties and provide the desired service life. The materials intended for biomedical applications should possess excellent biocompatibility, appropriate mechanical properties such as, e.g., high wear and fatigue resistance, high ductility, high strength-to-weight ratio, and low cytotoxicity [14-16]. The human body environment contains electrolytes, organic acids, enzymes, etc., which makes it a highly corrosive environment. Corrosion and degradation consequently lead to weakening and as a consequence failure of the implanted device. Hence, metallic implants should have got acceptable corrosion rate. What is more, rejection of an orthopedic implant, due to the release of toxic ions can lead to implant loosening and potential reoperation. Hence, metal-made implants are expected to be made of non-toxic elements. High corrosion resistance enables the preservation of biocompatibility and intended mechanical properties of implant material. Materials used to production of bone implants not only should fulfill mentioned biomedical application criteria but in many cases, also have an elastic modulus as close as possible to that of a human bone and good osseointegration [17-19]. Hence, biometals used for orthopedics, usually undergo a wide range of surface and structure modifications to meet all mentioned criteria required to apply them in the human body environment.

The vast majority of metallic implants can be classified based on their major alloying element and chemical composition: titanium alloys, cobalt-based alloys, stainless steels, and miscellaneous, e.g., shape-memory NiTi or resorbable ones. Typical materials used for the production of bone implants are stainless steels, cobalt-based alloys, and titanium-based alloys [7,20]. Although 316L grade stainless steel and cobalt-based alloys are generally used, titanium-made implants are becoming the first choice for the production of hard-tissue implants. However, due to corrosion in the human body, toxic and carcinogenic elements such as Ni, Cr, and Co are released from stainless steel and cobalt-based alloys implants [21-26]. What is more, steel or chromium-based hard tissue implants exhibit a much higher Young's modulus (e.g., 210 GPa for 316L stainless steel and 240 GPa for chromium-cobalt alloys) in comparison to the value for a human bone which ranges 10–30 GPa [27-29]. If a bone implant modulus is much higher than bone a stress shielding may occur [30]. Due to this, steel and chromium-based hard-tissue implants tend to fail after long-term use [31-33]. Among the aforementioned materials used in orthopedics, titanium, and its alloys are considered as one of the best materials for hard-tissue implants due to a combination of mechanical properties, good biocompatibility, and osseointegration. Nonetheless, in the case of traditional implants, their low degradation rate has made them inadequate for the production of temporary implants. Hence, materials that corrode in a controlled manner are gaining significant interest in past years. At this moment, polymer-based implants, made of natural or synthetic polymers (e.g., collagen, alginate, polyvinyl alcohol, and polylactides) are used commercially [34,35]. Their undoubted advantage is the ease of adjusting their degradation speed in a physiological environment. On the other hand, they may be unsuitable in load-bearing applications due to the possibility of deterioration of their mechanical properties in a human body environment [36]. In the load-bearing condition, magnesium-based implants may prove to be a better choice. However, their rate of corrosion in a human body environment is of great concern.

1.1 Magnesium

Magnesium is the ninth most abundant element in the universe. It is a relatively abundant element on Earth. However, magnesium in a metallic form does not occur in nature, but it can be found in a form of compounds. A large amount of magnesium is dissolved in the seawater [37].

1.1.1 Magnesium properties

Magnesium is a chemical element with the symbol Mg and atomic number 12 and the atomic mass is 24.32. Magnesium is a divalent metal, silvery-white in approach. The density of magnesium and its alloys are approximately 1.7 g/cm^3 at room temperature. Magnesium has a close-packed hexagonal (hcp) structure with the lattice constants a_{RT} = 0.321 nm and c_{RT} = 0.521 nm. The melting point is 649.5 °C and the boiling point is 1107 °C [38].

1.1.2 Industrial applications of Magnesium

In its industrial applications, magnesium is used mainly as an alloying element in aluminum, zinc, lead, and other nonferrous alloys or as a reducing agent, oxygen scavenger, and desulfurizer [39]. The density of magnesium is significantly lower than that of steel, titanium, and aluminum alloys. It is even lower than the density of most of the glass-fiber-reinforced polymers and similar to that of much more expensive carbon–fiber composites [40,41]. Magnesium is one of the lightest metals that can be used as a structural material. A combination of good stiffness and mechanical stability and high thermal and electrical conductivity, as well as good vibration and shock absorption ability, are desired in engineering design. However, magnesium is difficult to form at room temperature as a result of an insufficient number of deformation modes (slip systems) due to its hexagonal structure.

The mechanical properties and versatility of cast magnesium improve when it is alloyed with other metals. These properties made magnesium willingly used in car and aerospace engineering where the use of light and durable materials allows a significant reduction in fuel consumption. For example, each 100 kg reduction in vehicle weight reduces fuel consumption by 0.38 liter per 100 kilometers and CO_2 emission by 8.7 g per kilometer [42]. The reduction of mass is also accompanied by improvement of vehicle performance attributes such as acceleration, braking, and handling. However, due to some manufacturing, assembly, and service lifetime problems, as well as, economic factors, it is used only in the production of specific parts of vehicles. Nowadays, magnesium alloy-made parts make up less than 0.5% of the total mass of an average vehicle [43]. In automotive, magnesium alloys are used to produce, e.g., gearboxes, steering wheels, engine elements, and parts that have got very complex geometries by high pressure die casting. One of the most famous applications of magnesium is the air-cooled engine crankcase and gearbox of the Volkswagen Beetle made in the second half of the twentieth century. The magnesium-made parts can also be found in many portable electronic devices such as laptops, cell phones, and cameras. Due to its theoretical energy density and relatively low price, there are attempts to use magnesium as an electrode material [44]. However, there is no commercialization of Mg-based battery technology yet.

1.1.3 Medical applications of Magnesium

Magnesium is seen as a rapidly corroding metal which is not entirely true. Corrosion due to poor design, surface contamination, or use under inappropriate conditions can be avoided as with other metals by, e.g., use of suitable coatings or anodizing. The correct ways of application of magnesium-based materials in aggressive environments had been already established and implemented in the automotive and aerospace industries [45-47]. Among other uses, medical applications of magnesium constitute a highly profitable niche market [48]. Compared with traditional metallic biomaterials, i.e., stainless steel, cobalt-chromium-based alloys, titanium alloys, etc. magnesium has many advantages. The ability of magnesium to dissolute harmlessly and its great biocompatibility make magnesium and its alloys a convenient choice for a temporary implant. Elastic modulus (45 GPa) and density (1.74 g/cm^3) of magnesium are close to those of natural bone (20–57 GPa and 1.75-2,1 g/cm^3, respectively) [49,50]. Compressive and tensile strength of magnesium (20–115 MPa and 90–190 MPa, respectively) are also similar to those of bones (160–240 MPa and 35–283 MPa, respectively) [51]. Despite its many advantages, the application attempts to use magnesium as a biomaterial have proved to be challenging due to its relatively high corrosion rate in a human body environment. It has been already noticed after its application to leg bone fractures at the end of the 19th century [52-54]. It limits the field of practical applications of the implants because they may dissolve before the healing process is completed. Hence, both alloying and different treatments including various surface modification techniques (along with those based on severe plastic deformation), and conversion coatings are tried to eliminate those drawbacks, i.e., to decrease its degradation speed and increase its strength [55-59]. These attempts have resulted in the development of a new generation of functional resorbable biomaterials, among them, biodegradable magnesium-calcium alloys tested as a potential material for orthopedic implants [60-62].

1.2 Titanium

Titanium is a chemical element with the symbol Ti and atomic number 22 and the atomic mass is 47.867 g mol^{-1}. It is a lustrous transition metal with a silver color. The earth’s crust contains approximately 0.6% of Titanium, making it the fourth most common structural metal after aluminum, iron, and magnesium. Most often it can be found in minerals ilmenite ($FeTiO_3$) and rutile (TiO_2).

1.2.1 Titanium properties

The density of pure titanium is approximately 4.5 g cm^{-3} at room temperature. The melting point is 1650 °C and the boiling point is 3287 °C. Pure titanium has got two allotropic forms. At low temperatures, pure titanium has hcp structure, called α titanium. At 882±2°C, pure titanium changes its crystal structure from hcp structure (α phase) to body-centered cubic (β phase) [63]. This temperature greatly depends on the amount of impurities. At room temperature, the lattice parameters of the α phase are a = 0.295 nm and c = 0.468 nm. For pure β titanium at 900 °C, the value of the lattice parameter a is equal to 0.332 nm.

1.2.2 Industrial applications of Titanium

Titanium is available as commercially pure (cp) and as alloys. Despite the great number of titanium alloys, they can be categorized into three major groups: α alloys, β alloys, and α + β alloys; and their properties greatly depends on their microstructure, especially on impurities content, volume fractions, and arrangement of α and β phases [63]. Depending on production technology and type of alloys, the degree of impurities varies. The higher fraction of impurities translates to higher mechanical strength and lower material plasticity.

Properties such as high strength, low density, and excellent corrosion resistance make titanium useful for plenty of applications. Titanium-made elements are generally used in systems and parts where its selection is based essentially on corrosion resistance and/or high strength to weight ratio. In the last several decades, titanium-based materials attracted interest in a variety of industries in such areas as aerospace, automotive, power generation or biomedical devices, and biomedical implants. However, the relatively high cost of titanium production deters its broad use for example in automotive. Titanium cannot be straightforwardly produced by a simple reduction of titanium dioxide. Titanium is produced in the Kroll process that involves the reduction of $TiCl_4$ with magnesium [64]. This process has hardly changed for years and it is the main process used for titanium sponge production today [65]. The production of high purity titanium is costly mainly due to its high reactivity with oxygen and nitrogen.

As it was mentioned, due to high production costs, titanium is usually used in applications where it is needed. A good example is the titanium-made landing gear beams of Boeing 747 and 757 [66]. It could be made of a much cheaper aluminum alloy, but the required size of the part that is capable of carrying the required loads will be too big to fit inside the wing envelope. Steel could be used as well but at the cost of the expense of weight and greater fuel consumption. The combination of low density, high strength, and high creep resistance makes titanium usable material for the construction of airframes and aero-engines. For example, β titanium alloys make about 10% of the Boeing 777 airframe total weight [67]. Applications based on corrosion resistance of titanium in the chemical and power industries such as chemical processing apparatus, tanks, heat exchangers use cp titanium normally. In the case of the automotive industry, titanium is generally too expensive for the general consumer market. It is rather used in specific applications where the benefit-cost ratio is acceptable. Titanium is usually used in applications for high-strength performance, e.g., some parts of car engines such as outlet and intake valves (cp-titanium and Ti-6Al-4V), turbochargers rotors (TiAl) [68]. Cp-titanium (grade 2) as well as its alloys are used also as weight-saving material, e.g., used as a base material for exhaust systems of sports cars and motorcycles [69]. Titanium can be used as well as a structural material in building applications such as walls or roofing material [70]. Other miscellaneous, industrial applications of titanium are, e.g., coatings for pharmaceuticals, food additives, and paints. Titanium can be found in some consumer products such as cameras or jewelry. The large application field is the sports equipment market, especially golf club heads.

1.2.3 Medical applications of Titanium

Due to its mechanical strength, biocompatibility, and long service lifetime, titanium is commonly used as an implant material within the medical and dental fields [71]. The most used titanium-made materials are cp-Ti and Ti-6Al-4V. Titanium is considered as one of the best biocompatible metals. Great biocompatibility, combined with easy shaping, excellent strength to weight ratio, and great corrosion resistance (compared to Co-Cr-based alloys) in a human body environment make titanium a first choice material for the production of long-term hard tissue implants and braces. Typical values of the modulus of elasticity are about 105 GPa for cp-titanium, 115 GPa for commercial α+β, and 70-90 GPa for the as-quenched condition, and 100- 105 GPa for the annealed condition of commercial β alloys [72]. For comparison, the value of elastic modulus for human bones varies between 20 and 57 GPa. However, the tensile strength of titanium-made materials is much higher than those of human bones (35 to 283 MPa) and varies from about 200 MPa for pure titanium to about 1400 MPa for near α titanium alloys. The value for popular Ti-6Al-4V varies from 900 to 1200 Mpa [73]. The main challenges in the development of new titanium alloys for medical applications are the elimination of potentially harmful elements such as Al and V and lowering elastic modulus to the values closer to those for human bones. However, there are reports about the toxicity of titanium itself. A systematic deposition of titanium ions and particles in tissues due to the corrosion and wear of implants can lead to toxic and allergic reactions [74]. In the literature, the correlation between titanium-based implant surface treatments and their toxicity behavior can be found [75,76].

1.3 Stainless steels

Austenitic chromium-nickel stainless steels are alloy steels characterized by high corrosion resistance. Steel is defined as an iron-based alloy in which the carbon content ranges up to 2 percent. Austenitic steels have a face-centered cubic crystalline structure of austenite (γ phase Fe) which makes them non-magnetic and prevents them from being hardenable by heat treatment. The ‘stainless’ means that steel is resistant to staining, rusting, or corroding in environments where normal steels are susceptible to them. The low carbon content reduces the susceptibility to intergranular corrosion caused by the precipitation of chromium carbides at the grain boundaries. Stainless steels have better retention of strength and stiffness at elevated temperatures compared with carbon steels [77].

To receive such rust-resistant steels, the steel must contain at least about 11wt% of chromium. The addition of chromium enables the formation of self-healing, and resistant to environmental conditions chromium oxide on the surface of the alloy. The Fe and Cr are the base for stainless steels, other alloying elements such as Ni, Si, Cu, Ti, Mn, Mo, and others, are added to design desired properties. For example, Cu is added to improve the hardness of steel, i.e., Cu forms strengthening precipitates. The addition of Mo improves the pitting resistance of the alloy. The addition of nickel provides an austenitic structure. Despite a large number of alloying elements their total content in stainless steel is below the iron content.

Austenitic stainless steels are the most widely used stainless steels. Among them, the most popular are those from the AISI300 series based on a system of Fe-Cr-Ni alloys. The applications of stainless steel are plentiful and range from low-end, like kitchenware, e.g., knives or furniture, to very advanced like cars, ships, and medicine. For example, the most common stainless steel used in dental applications and the production of coronary stents is 316L. It is also used in temporary devices in orthopedic surgeries due to its low cost and relatively good biocompatibility [78]. 316L type stainless steels are still the most common material used for production implants for cardiovascular and otorhinology applications [79]. However, in load-bearing applications, where high wear resistance is required, Co-Cr-Mo alloys are a better choice.

References

1. A. Ode, GN. Duda, S. Geissler, S. Pauly, JE. Ode, C. Perka, P. Strube, PLoS One. 9 (2014) e106462.
2. J. Gage, A. Liporace, A Egol, M McLaurin, Bull Hosp Jt Dis. 76 (2018) 4.
3. ID. Learmonth, C. Young, C. Rorabeck, Lancet 27 (2007) 1508.
4. S. Bauer, P. Schmuki, K. von der Mark, J. Park, Prog. Mater. Sci. 58 (2013) 261.
5. J.B. Park, R.S. Lakes, Biomaterials: An Introduction, Springer, New York, 2007.
6. Y. Li, C. Yang, H. Zhao, S. Qu, X. Li, Y. Li, Materials, 7 (2014) 1709.
7. M. Navarro, A. Michiardi, O. Castaño, J.A. Planell, J. R. Soc. Interface 5 (2008) 1137.
8. N. Kiaie, F. Aavani, M. Razavi, 2 - Particles/Fibers/Bulk, in M. Razavi, A. Thakor (eds.): Nanobiomaterials Science, Development and Evaluation, Woodhead Publishing, 2017, 7-25.
9. A.D. Mazzocca, J.P. DeAngelis, A.E. Caputo, et al., Principles of internal fixation, in B.D. Browner (Ed.): Skeletal Trauma, W.B. Saunders Company, Philadelphia, 2008.
10. Long, M., Rack, H.J. Biomaterials 19 (1998) 1621.
11. F. Rupp, J. Geis Gerstorfer, K.E. Geckeler, Adv. Mater. 8 (1996) 254.
12. V. Biehl, T. Wack, S. Winter, U.T. Seyfert, J. Breme, Biomol. Eng. 19 (2002) 97.
13. P. Chakraborty Banerjee, S. Al-Saadi, L. Choudhary, S.E. Harandi, R. Singh, Materials 12 (2019) 136.
14. F.H. Jones, Surf. Sci. Rep. 42 (2001) 75.
15. BD. Ratner, A perspective on titanium biocompatibility, in D.M Brunette, P. Tengvall, M. Textor, P. Thomson (eds.): Titanium in medicine material science, surface science, engineering, biological responses and medical applications. Berlin, Springer, 2001. 2–12.
16. S. Bauer, P. Schmuki, K. von der Mark, J. Park, Prog. Mater. Sci. 58 (2013) 261.
17. DW. Hoeppner, V. Chandrasekarn, Wear 173 (1994) 189.
18. B.S. McAllister, K. Haghighat, J. Periodontol. 78 (2007) 377.
19. K. Miura, N. Yamada, S. Hanada, T.K. Jung, E. Itoi, Acta Biomater. 7 (2011) 2320.
20. Q. Chen, G.A. Thouas, Mater. Sci. Eng. R Rep. 87 (2015) 1.
21. KL. Wapner, Clin. Orthop. Relat. Res. 271 (1991) 12.
22. Y. Okazaki, E. Gotoh, Biomaterials 26 (2005) 11.
23. R.B. Tracana, J.P. Sousa, G.S. Carvalho, J. Mater Sci: Mater Med 5 (1994) 596.
24. F.W. Sunderman, in: H.F. Hildebrand, M. Champy (eds.) NATO ASI Series (Series A: Life Sciences) 171, Springer, Boston, MA, 1988.
25. K. Arvidson, M. Cottler-Fox, E. Hammarlund, U. Friberg, Scand. J. Dent. Res. 95 (1987) 356.
26. DB. McGregor, RA. Baan, C. Partensky, JM. Rice, Wibourn. Eur J Cancer 36 (2000) 307.
27. JY. Rho, RB. Ashman, CH. Turner, J. Biomech. 26 (1993) 111.
28. J. Lawrence Katz, Nature 283 (1980) 106.
29. M. Niinomi, Mater. Sci. Eng. A 243 (1999) 231.

30. DL. Millis, Canine Rehabilitation and Physical Therapy (Second Edition), Elsevier 2014.
31. M.I.Z. Ridzwan, S. Shuib, A.Y. Hassan, A.A. Shokri, M.N. M. Ibrahim, J. Med. Sci. 7 (2007) 460.
32. N. Sumitomo, K. Noritake, T. Hattori, K. Morikawa, S. Niwa, K. Sato, M. Niinomi, J Mater. Sci. Mater. Med. 19 (2008) 1581.
33. SH. Teoh, Int. J. Fatigue 22 (2000) 825.
34. H.-Y. Cheung, K.-T. Lau, T.-P. Lu, D. Hui, Compos. Part B Eng. 38 (2007) 291.
35. G. Dolete, C.F. Ilie, I.F. Nicoară, et al. Understanding dental implants, in A.M Grumezescu (ed.): Nanobiomaterials in Dentistry, William Andrew Publishing, 2016, 27-47.
36. N.M. Neves, A. Kouyumdzhiev, R.L. Reis, Mater. Sci. Eng. C 25 (2005) 195.
37. G.L. Maker, J. Kruger, Int. Mater. Rev. 3 (1993) 138.
38. E. Ghali, Magnesium and Magnesium Alloys, in R.W. Revie (ed.): Uhlig's Corrosion Handbook, Third Edition, John Wiley & Sons, Ltd, 2011, 809-836.
39. F. Cardarelli, Materials Handbook; Springer: London, UK, 2008.
40. B.R. Powell, P.E. Krajewski, A.A. Luo, Magnesium alloys for lightweight powertrains and automotive structures, in P.K. Mallick (ed.): Materials, Design and Manufacturing for Lightweight Vehicles; Woodhead Publishing Limited, UK, Sawston, 2010, 114–173.
41. I. Polmear, Light Alloys, in: From Traditional Alloys to Nanocrystals, 4th ed. Butterworth-Heinemann, UK, Oxford, 2005.
42. T. B. Abbott, Corrosion 71 (2015) 120.
43. Oak Ridge National Laboratory, Transportation Energy Data Book, 34th ed. Oak Ridge, TN, Oak Ridge National Laboratory, 2015
44. Z. Guo, S. Zhao, T.Li, D. Su, S. Guo, G. Wang, Adv. Energy Mater. 10 (2020) 1903591
45. Magnesium Alloys and their Applications. K.U. Kainer (ed.), John Wiley & Sons, Ltd, 2000.
46. A.A. Luo, Mater. Sci. Forum 419 (2003) 57.
47. Z. Yang, J.P. Li, J.X. Zhang, G.W. Lorimer, J. Robson, Acta Metall. Sin-Engl 21 (2008) 313.
48. G. Patzer, The magnesium industry today: the global perspective, in S.N. Mathaudhu, A.A. Luo, N.R. Neelameggham, E.A. Nyberg, W.H. Sillekens (eds.): Essential readings in Magnesium Technology, Springer International Publishing, Germany, Heildeberg, 2010, 13–18.
49. M. Razavi, M.H. Fathi, M. Meratian, Mater. Sci. Eng. A 527 (2010) 6938.
50. A. Feng, Y. Han, J. Alloys Compd. 504 (2010) 585.
51. G.E.J. Poinern, S. Brundavanam, D. Fawcett, J. Biomed. Eng. 2 (2012), 218.
52. P. Chakraborty Banerjee, S. Al-Saadi, L. Choudhary, S.E. Harandi, R. Singh, Materials 12 (2019) 136.
53. P. Hou, P. Han, C. Zhao, et al. Sci. Rep. 7 (2017) 41924.
54. F. Witte, Acta Biomater. 23 (2015) 28.
55. C.-J. Li, H.-F. Sun, S. Cheng, H.-M. Tan, T.-H. He, W.-B Fang, Mater. Res. Express 6 (2019) 026539.
56. A. Millenin, P. Kustra, D. Byrska-Wójcik, M. Wróbel, M. Paćko, J. Sulej-Chojnacka, S. Matuszyńska, B. Płonka, Arch. Civ. Mech. Eng. 20 (2020) 60.
57. X. Zhang, X.-W. Li, J.-G. Li, X.-D. Sun, Appl. Mater. Interfaces 6 (2014) 513.
58. M.A.F. Zaludin, Z.A.Z. Jamal, M.N. Derman, M.Z. Kasmuin, J. Mater. Res. Technol. 8 (2019) 981.

59. S.J. Zhou, J.F. Li, J.P. Long, H.Q. Du, Mater. Sci. Forum 814 (2015) 389.
60. N.T. Kirkland, N. Birbilis, Magnesium Biomaterials, Design, Testing and Best Practice, Springer International Publishing, Germany, Heildberg, 2014.
61. N. Erdmann, N. Angrisani, J. Reifenrath, A. Lucas, F. Thorey, D. Bormann, A. Meyer-Lindenberg, Acta Biomater 7 (2011) 1421.
62. N. Li, Y.D. Li, Y.X. Li, Y.H. Wu, Y.F. Zhen, Y. Han, Mater. Sci. Eng. C 35 (2014) 314.
63. Y. Luo, Biotribology of Titanium Alloys, in J.P. Davim (ed.): Biotribology, ed. by ISTE-Wiley, UK, London, 2010.
64. C.R.V.S. Nagesh, C.S. Rao, N.B. Ballal, P. Krishna Rao, Metall. Mater. Trans. B 35 (2004) 65.
65. W. J. Kroll, Trans. El. Soc. 78 (1940) 35.
66. R.R. Boyer, Mater. Sci. Eng. A 213 (1996) 103.
67. R.R. Boyer, J. of Metals 44 (1992) 23.
68. O. Schauerte, Adv Eng Mater 5 (2003) 411–418.
69. Y. Kosaka, K. Faller, S.P. Fox, JOM 56 (2004) 32.
70. T. Moriyasu, Titanium ‘95, Science and Technology, UK, Cambridge, The University Press, 1996, 21.
71. AT. Sidambe, Materials (Basel) 7 (2014) 8168.
72. R. Boyer, G. Welsch, E.W. Collings (eds.): Materials Properties Handbook: Titanium Alloys, ASM, Materials Park, USA, (1994).
73. C. Veiga, J.P. Davim, A.J.R. Loureiro, Rev. Adv. Mater. Sci. 32 (2012) 133.
74. K.T. Kim, M.Y. Eo, T.T.H. Nguyen, S.M. Kim, Int J Implant Dent. 11 (2019) 10.
75. T. Albrektsson, B. Chrcanovic, J. Molne, A. Wennerberg, Eur. J Oral Implantol. 11 (2018) 37.
76. R. Shah, D.S.L. Penmetsa, R. Thomas, D.S. Mehta. Eur J Prosthodont Restor Dent. 24 (2016) 171.
77. L. Gardner, N.R. Baddoo, J Constr Steel Res 62 (2006) 532.
78. M. Fellah, M. Labaïz, O. Assala, A. Iost, L. Dekhil, Tribology - Materials, Surfaces & Interfaces Volume 7 (2013) 135.
79. H. Hermawan, D. Ramdan, J.R.P. Djuansjah, Metals for Biomedical Applications, in R. Fazel-Rezai (ed.): Biomedical Engineering: From Theory to Applications, IntechOpen, 2011.

Chapter 2: Crystal lattice defects, plastic deformation, and recrystallization

Metals are one of the most widely used materials in the world. Many metallic materials are produced initially as large castings which are then subjected to various mechanical treatments such as, e.g., forging, rolling, or extruding into a final product with desired properties. These procedures may be hot or cold and may include intermediate annealing referred to as a thermomechanical treatment. Recovery, recrystallization, and grain growth are essential elements of this process. Recrystallization can be carried out already during the deformation of the material at elevated temperatures in a process called dynamic recrystallization.

Although the art of metalworking, involving deformation and heating, has been known for thousands of years, the processes of structural changes that accompany them have been understood relatively recently. Plastic deformation induces changes in the number and type of defects that are present inside a workpiece. The spatial distribution of defects in the material after deformation is more or less heterogeneous. Those defects, especially vacancies, and their clusters or dislocations can be tracked and distinguished using PAS techniques.

Summing up, it is worth mentioning that defects determine many properties of materials which are called structure-sensitive properties. They change remarkably with the heat treatment and mechanical treatment of metals and depend on the detailed composition of alloys. They are, e.g., yield and tensile strength, ductility, fracture toughness, and creep and fatigue strength. Some other properties like diffusion-related ones, which may appear intrinsic, are also defect controlled. Only a few properties are not at all or only slightly affected by defects (the melting point or the elastic modulus). Creating imperfect crystalline materials allows materials scientists to tailor their properties.

2.1 Defects of the crystalline structure

Crystal lattice defects can be classified by their dimension in the following categories:

- point defects,
- line defects, i.e., dislocations,
- planar defects, e.g., grain boundaries.

In addition to defects on the atomic scale, macroscopic or bulk defects can be included, e.g., pores, cracks, inclusions, and voids.

2.1.1 Point defects

Point defects can be defined as crystal lattice defects of zero dimensionality, i.e., they do not possess lattice structure in any dimension. They disturb the crystal lattice pattern at an isolated site. [1]. Two types of point defects can be distinguished, i.e., intrinsic and extrinsic. Fig. 2.1 shows a schematic diagram of examples of point defects that are present in a perfect crystal lattice.

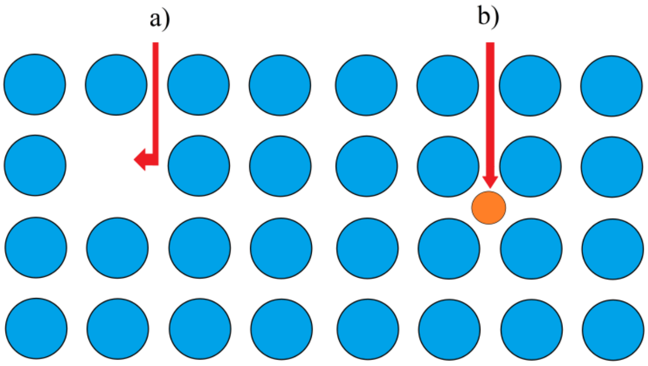

Figure 2.1 Point defects in a crystal lattice: a) an intrinsic defect – a vacancy, b) an extrinsic defect – an interstitial atom.

An intrinsic defect is a defect present in a pure material. It is an atom missing from a position that should be filled in the crystal, i.e., a vacancy; or it is an atom shifted between the correct structural positions, creating an interstitial atom. The interstitial sites are usually small hence interstitial atoms are high-energy defects that are relatively uncommon. On the other hand, vacancies are much more common in all crystalline solids [2].

During deformation, point defects may appear such as interstitial atoms or substitutional atoms and vacancies whose density may increase by several orders. Their generation is connected to dislocation movements which will be explained in Chapter 2.2. Vacancies can be created as well by rapid cooling from high temperatures or the impact of radiation on the crystal lattice. Vacancies may form clusters up to several defects. Vacancies and vacancy-related defects (i.e., dislocation loops and stacking faults) may influence mechanical properties in metals [3,4].

Vacancies can move through the crystal lattice by exchanging positions with their neighbors. The presence of vacancies influences the migration and diffusion of atoms in solid-state matter, in particular at high temperatures.

An extrinsic defect is an atom of a different type than the bulk atoms, which has replaced one of the bulk atoms in the lattice. They are called solutes if they are intentionally added to the material, or they are called impurities if not. They can be present at interstitial sites (interstitial solute/impurity) or they can replace bulk atoms on their correct positions (substitutional solute). Substitutional impurity atoms are usually close in size to the bulk atom. Atoms such as, e.g., hydrogen, carbon, or nitrogen can fit into spaces between the bulk atoms forming interstitial solute [2].

2.1.2 Line defects

Line defects or dislocations are line imperfections, causing discontinuities in the lattice in areas larger than a single atom. Two types of dislocation can be distinguished, i.e., edge and screw dislocations. However, the most common dislocations that are present in metals are hybrids of the edge and the screw forms. The formation of dislocation and their influence on the mechanical properties of metals is discussed further in Chapter 2.2.

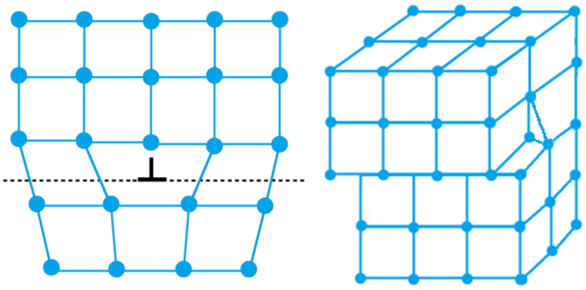

a) b)

Figure 2.2 Schematic diagram of an: a) an edge dislocation in 2D in a simple cubic structure, the dotted plane is a slip plane, b) a screw dislocation in 3D in a cubic structure.

An edge dislocation is an additional plane of atoms crammed into a crystal lattice. The part with extra atoms is under compressive stresses, and that with the correct number of atoms is exposed to tensile stresses.

A screw dislocation is a displacement in form of a step or a ramp of atoms in a plane in the crystal, which creates a boundary between the slipped and unslipped atoms in the crystal lattice. A schematic illustration of edge and screw dislocations are shown in Figure 2.2.

A dislocation that has an extra plane of atoms or neither it misses one is called a dislocation loop, and it has a circular shape usually due to its results in the lowest dislocation energy.

2.1.3 Planar defects

Planar or two-dimensional defects can be categorized into three types: free surfaces, intercrystalline boundaries, and internal defects [2]. Free surfaces are surfaces at which the solid terminates at a vapor or liquid and determines the behavior and shape of solids, i.e., the shape of crystals. The vast majority of crystalline solids are polycrystalline, which means they are constructed from small crystallites called grains. One of the most important internal interfaces are grain boundaries. In a grain boundary, atoms are shifted from their positions in comparison to the ones inside the crystal interior. Grain boundaries are defects that separate grains of different orientations or distinct phases from each other [5]. The misorientation of crystal grains influences the shape and structure of grain boundaries, i.e., the small misorientation causes low-angle boundaries formation. A low-angle boundary is a planar array of dislocations. Low-angle tilt grain boundaries consist of edge dislocations, while screw dislocations form low-angle twist boundaries. When the misorientation inside crystals is larger high-angle grain boundaries are formed [6]. A high-angle grain boundary can be defined in a simplified way, i.e., its structure can be understood by matching two crystals that are misoriented by the angle of the boundary [2]. Generally, it can be assumed that low-angle boundaries are those with misorientation angles lower than 15 degrees, while the high-angle boundaries are those with 15 and more degrees of misorientation, as shown in Fig. 2.3 [7].

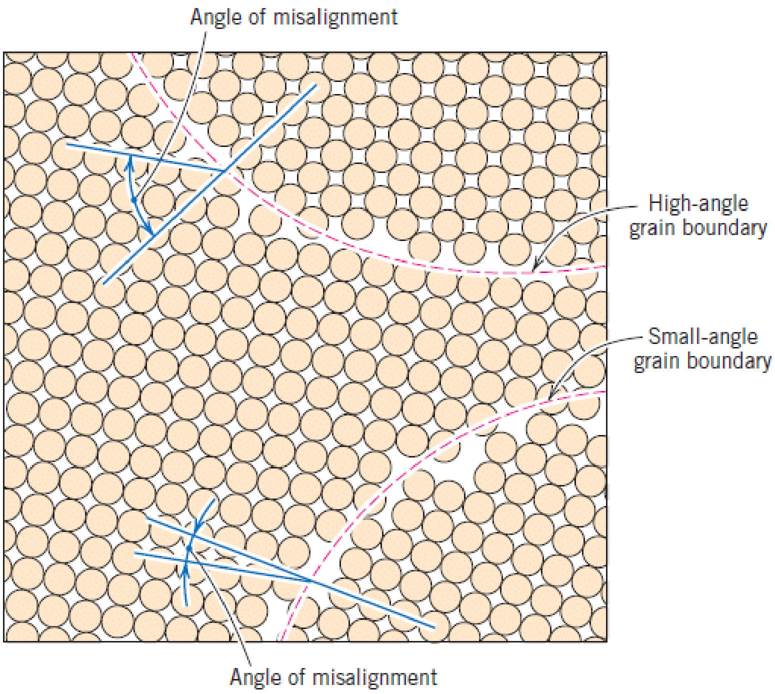

Figure 2.3 Schematic of a low and high angle grain boundary and the angle of misorientation [8].

Stacking faults and twin boundaries belong to internal defects which disrupt the internal structure of crystals. Stacking faults are errors in the order of the sequential layering of crystallographic planes and are usually surrounded by partial dislocations [9]. Three types of stacking faults can be distinguished, extrinsic and intrinsic, and twin boundaries. The first one is created when an extra plane is inserted into a lattice, while the intrinsic is formed when a plane of atoms is removed. A twin boundary divides two identical areas (that are mirror images of one another) of crystal. They are usually introduced during the change of the volume of a crystal, e.g., during plastic deformation.

2.2 Plastic deformation

External forces acting on the crystalline solids can cause their deformation. Depending on their magnitude, a crystal may undergo elastic or plastic deformation. During the elastic deformation, the material is experiencing stresses lower than its elastic limit, which means after removing the external force atoms of the material return to their equilibrium position resulting in the recovery of an original shape of the material. Plastic deformation occurs when the crystal is subjected to stresses greater than its elastic limit hence after the stress is removed material does not restore its original shape. Extending the value of force can lead to reaching the end of the plastic deformation range of material resulting in a fracture.

The microstructure of metals changes during the plastic deformation, and thus their properties also change. First, the grains change their shape and the total surface area of the grain boundaries increases significantly. A new grain boundary area must be created during deformation and this is done by attaching certain dislocations that are constantly produced during the deformation process. Shapes and dimensions of the grains and their boundaries depend on the limitations imposed by changes in the shapes of their neighboring grains. The grains of the polycrystalline metal change their shape in a manner corresponding to the macroscopic change of workpiece shape. For example, uni-axial pressing of the workpiece causes elongation of grains, and the grain boundary area increases. Grains deformation is accompanied by changes in their internal structure as well, i.e., the creation of subgrains. The shape and sizes of grains have a significant impact on metals’ mechanism of fracture, depending on the working temperature, i.e., at relatively low temperatures, grain boundaries have more strength than the interior of grains. On the other hand, at higher temperatures, grain boundaries are weaker regions, and fractures can happen through them. The growth rate of the grain boundaries depends largely on the type of deformation.

Another phenomenon visible after deformation is the change in the orientation of individual crystals and individual grains of polycrystalline metal according to the direction of the applied stress. As a result, the grains acquire a preferred orientation or texture as they deform.

Dislocations are generated and move when stress is applied to the material. Plastic deformation leads to a rapid increase in the density of dislocations, which is caused by the attachment of newly formed mobile dislocations to the existing ones during deformation. The dislocation's density in metals before plastic deformation is of an order of 10^6-10^8 cm^{-2} after plastic deformation it can raise to 10^{15}-10^{16} cm^{-2} (values for deformed Cu [10]). As it was mentioned, dislocations influence the microstructure of the material, e.g., the shape of the grain boundaries. The dislocation movement through the crystal lattice can create new lattice areas such as twins. A deformation twin can be defined as a region of a crystalline body that had undergone a homogeneous shape deformation in such a way that the resulting product structure is identical to that of the parent but oriented differently [11]. The motion of dislocations allows slip—plastic deformation to occur. Dislocations move along the densest planes of atoms in a material. Moving through the crystal lattice, dislocations encounter obstacles in the form of defects - mainly: dislocation systems or other moving dislocations, and, e.g., vacancies and impurity atoms. Slip and twinning are the basic mechanisms of the plastic deformation of crystals.

The increase in dislocation density during deformation causes that moving dislocations more often encounter dislocation systems with which they can form dislocation tangles. These processes lead to the reduction of the free dislocation path and so-called strengthening - an increase in the value of yield stress caused by deformation of the material. It increases the value of stresses needed to induce a dislocation movement. As the number of dislocations increases, plastic strength increases, and ductility decreases. Strengthening takes place until a certain maximum dislocation density is reached, depending on the type of the deformed material, method of deformation, and temperature. For example, the stretched material experiences tensile stresses, and if the critical dislocation density is exceeded, its continuity is broken. Material compressed, e.g., using a hydraulic press, experiences compressive stresses. Due to this process, dislocation systems can create new grain boundaries. The newly formed sub-grain boundaries are also obstacles to moving dislocations. If the hardened material is then annealed at an appropriate temperature, the number of dislocations will be reduced, which results in a decrease in strength and an increased ductility of the material.

2.3 Cold working

Cold working can be defined as a process of a material deformation that occurs below the 0.4 of its melting temperature. During cold working, the energy used for deformation is mainly converted into heat. The rest of the energy is converted into the energy of the dislocation fields. The delivered energy is stored in a form of the elastic energy of the atoms shifted from equilibrium positions around various defects. The amount of accumulated energy depends on the density of defects (mainly dislocations) in the deformed material. Therefore its amount is influenced by all the factors determining the density of dislocations. The value of free energy of deformed crystals is increased and hence they are thermodynamically unstable. Relatively large deformation of the material can lead to the release of some of the stored energy. Heating in the appropriate temperature range starts greater energy release.

2.4 Recovery and recrystallization

The number of defects, e.g., dislocations, increases during deformation which makes the material thermodynamically unstable. Thermally activated processes can remove those defects and reduce the energy of the system. The energy stored inside the material during plastic deformation is responsible for strengthening the deformed material and its loss during annealing leads to changes in the properties of the material. The basic processes leading to the rebuilding of the crystal structure after plastic deformation are recovery and recrystallization. Those processes can be considered static and have been well known and widely used [12-14].

These processes involve the removal of excess energy introduced into the material during its deformation and cause a reduction in the density of defects and the formation of new grains. Appropriate annealing can restore the material to its pre-deformation state.

2.4.1 Recovery process

Material recovery is carried out at a lower temperature than recrystallization [10]. During the recovery process, the density of point defects and dislocations is reduced. The diffusion of atoms occurs and their recombination with vacancies results in the reduction of the number of this type of imperfections. A dislocation movement occurs as well, during which dislocations with opposite orientations are annihilated. As the temperature rises, the grain boundaries consisting of dislocations of the same sign become polygonized, i.e., grouped in certain planes. Heating leads to a partial annihilation of defects inside the grains and the shapes of the inter-grain boundaries become more regular. Those processes result in the reduction of the energy stored in the material during its deformation, as well as, residual stress reduction, and the increase in the plasticity of the material.

2.4.2 Recrystallization

During the recrystallization process, subgrains are formed in the material, which then increase in size. The recrystallization process can be divided into two stages: primary and secondary recrystallization [10].

During the first step of recrystallization, a process called nucleation occurs, during which small regions with an almost perfect crystal structure are created. Sub-grains that have boundaries which are fragments of wide-angle boundaries of the original grain can form new grains. These new grains are formed in places of increased energy and can grow. At the basis of this process, there is the movement of grain boundaries accompanied by the release of stored energy. Nucleation continues until new grains appear throughout the whole volume of the material and the boundaries of newly formed grains meet each other.

Secondary recrystallization takes place at a higher temperature than primary recrystallization. The structure formed during primary recrystallization may be thermodynamically unstable and under appropriate conditions, it may lead to the so-called abnormal growth of some of the grains. The reason for the growth of the grains is the difference in energy accumulated within the boundaries of the adjacent grains of the material and forces that comes from the difference in dislocation density in newly formed grains, which causes the stress fields in the grains. As these grains expand, they absorb smaller grains and subgrain boundaries. The increase in the grain size causes deterioration of the physical properties of the material. Therefore, it is avoided to keep materials at high temperatures longer than necessary to complete recrystallization.

References

1. H.J. Wollenberger, Chapter 18 - point defects, in R.W. Cahn, P. Haasen (eds): Physical Metallurgy (Fourth Edition), North-Holland, 1996, 1621-1721
2. Jr.J.W. Morris, Defects in Crystals, in: Materials Science and Engineering: An Introduction. Wiley, 2013.
3. Y. A. Chang, L. M. Pike, C. T. Liu, A. R. Bilbrey, D. S. Stone, Intermetallics, 1 (1993) 107.
4. X. Ou, W. Anwand, R. Kogler, H.-B. Zhou, A. Richter, J. Appl. Phys. 115 (2014) 123521
5. D. Wolf, Structure and Energy of Grain Boundaries, in S. Yip (eds.): Handbook of Materials Modeling. Springer, Dordrecht 2005.

6. H. Gleiter, Microstructure, in R.W. Cahn, P. Haasen (eds.): Physical Metallurgy (Fourth Edition), North-Holland, 1996
7. G. Faraji, H.S. Kim, H.T. Kashi, Effective Parameters for the Success of Severe Plastic Deformation Methods, Editor(s): G, Faraji, H.S. Kim, H.T. Kashi (eds.): Severe Plastic Deformation, Elsevier, 2018.
8. W.D. Callister, D.G. Rethwisch, Materials science and engineering: an introduction 7, Wiley New York, 2007.
9. R.L. Wise, K.J. Lindberg, L.D. Dyer, H.R. Huff, Silicon Epitaxial Layers: Defects, in K.H. Jürgen Buschow, Robert W. Cahn, Merton C. Flemings, Bernhard Ilschner, Edward J. Kramer, Subhash Mahajan, Patrick Veyssière (eds.): Encyclopedia of Materials: Science and Technology, Elsevier, 2001.
10. F. J. Humphreys, M. Hatherly, Recrystallization and Related Annealing Phenomena, 2nd ed., Elsevier, Amsterdam, 2004.
11. A. Bilby, A. G. Crocker, Proc. Roy. Soc. 288 (1965) 240.
12. M.J. Avrami, Chem Phys 7 (1939) 1103.
13. M.J. Avrami, Chem Phys 8 (1940) 212.
14. W.A. Johnson, R.F. Mehl, Trans AIME 135 (1939) 416.

Chapter 3: Severe plastic deformation techniques

The comprehensive properties, performance, and lifespan of metal-made elements are determined by their microstructure. In the past decade, a growing interest in nanocrystalline (NC) materials, or nanomaterials, with greatly refined structures has been observed [1]. This class of materials arouses considerable interest due to their existing and potential applications in almost every technological area. Meanwhile, a large variety of machining processes has been developed to produce nanomaterials.

Special types of metal processing techniques based on SPD are receiving great attention due to their simplicity and ease of applicability for plentiful classes of materials. SPD is a generic term for a group of metal-machining techniques. They can be defined as metal forming techniques consisting of introducing large plastic strain into a bulk material to create ultra-fine grained structure without imposing significant changes in the dimensions of a workpiece [2]. The underlying mechanism of SPD is an increase in the polycrystals' free energy and the generation of a great number of defects and interfaces, i.e., dislocations and grain boundaries, respectively, in the workpiece. The main goal of SPD applications is to produce durable parts with a high strength to mass ratio. It is well known that producing a fine-grained microstructure in metals can enhance their overall physical and mechanical properties [3,4].

During SPD, the grain size reduction accompanied by reorganization of the dislocation structure, as well as large plastic stains introduction into a workpiece occur. As the decrease in the size of grains continues to a finer scale, the number of crystalline defects arises significantly, especially planar defects such as grain boundaries and other interfacial regions. The distances between the wide-angle grain boundaries significantly decrease, and the misorientation angle of those boundaries increases. Those processes result in the production of the structure containing small grains, called ultrafine grains, with large misorientation angles.

Various techniques based on SPD such as, e.g., ECAP, uniaxial pressing, SP, grinding, modified rolling, high-pressure torsion (HPT), super short multi-pass rolling (SSMR), or accumulative roll-bonding (ARB) have been developed [5-11]. SMAT and LSP are SPD methods that can produce a hard layer of gradient NC microstructure in the treated bulk material surface [12-14].

3.1 Nanocrystalline materials

While ultrafine-grained materials can be produced by most of the SPD techniques, NC materials can be obtained only by methods that are based on non-homogeneous deformation methods with large strain gradients [15]. NC materials can be defined as single or multiphase polycrystalline solids with an average crystallite size usually less than 100 nm. [1,16]. There have been developed several methods of production of bulk NC materials based on chemical deposition, magnetron sputtering, crystallization of amorphous solids, consolidation of ultrafine powders, or SPD. Bulk nanostructured metals can be defined as bulk solids whose structure is partly or fully nanostructured.

Due to a significant reduction in grain size, NC materials have physical and chemical properties that fundamentally differ from coarse-grained polycrystalline materials. Ultrafine grains can be defined as those with sizes ranging from 100 to 500 nm [16]. It is worth mentioning, that grain refinement is possible only to some minimum level characteristic for each material, which depends, inter alia, on the material's possibility to the annihilation of deformation defects. During significant grain refinement materials may even lose crystallinity due to an extreme increase in the number of grain boundaries [17].

Modern engineering benefits from the application of NC materials. Nanostructured bulk metals, as well as, alloys offer superior properties in comparison to their conventional counterparts, such as better fatigue and corrosion resistance [1]. The elastic properties of NC materials are generally the same as those of coarse-grained, while they exhibit increased hardness and yield strength.

However, NC materials have got some drawbacks, e.g., their thermal stability is of great concern. This problem limits their potential applications and narrows possible processing techniques. This is mainly the case of pure metals, e.g., Al, Zn, Mg, and even those with higher melting points such as Ni or Fe, while nanostructured metal alloys are less affected by this problem. Those materials may experience drastic grain size growth even at room temperature [18]. What is more, under applied stress the grain size can also increase in those materials. In some polycrystalline materials with greatly refined grains, a change from dislocation-based plasticity to grain boundary sliding mechanism and diffusion deformation may occur, which can lead to their softening [19,20]. This effect is called an 'inverse Hall-Petch effect' however the existence of this phenomenon has not been clearly proven to this day.

Properties of NC materials are utilized in many industries including, e.g., aerospace, automotive, power generation, and medicine. However, the production of bulk, artifact-free and without porosity or contamination relatively big parts with

NC structure is still a challenge. Among the vast number of applications, there can be found those including, e.g., corrosion-resistant coatings, sensors, permeable membranes, hydrogen storage materials, prosthetics, drug delivery systems, and diagnostic imaging [21-24].

3.2 Surface nanocrystallization

Fatigue, wear and corrosion that originate from the surface of metallic materials often shorten their service life. The magnitude of those factors is extremely sensitive to the microstructure and the properties of the surface of materials, while the grain size distribution beneath its surface has got a huge impact on its mechanical properties. Surface nanocrystallization (SN) processing technologies can be used to greatly enhance the durability of polycrystalline materials. Methods of SN of crystalline materials have been gaining popularity in recent years since their conceptualization by K. Lu and J. Lu in 1999 [25]. The methods enable the production of materials with the desired internal and surface structure, as well as, enhanced mechanical properties. In those methods various physical and chemical methods are utilized to refine the surface and a layer beneath it to the nanometer regime. SN is much cheaper and easier to carry out in comparison to bulk nanocrystallization.

SN methods can be categorized, as proposed by K. Lu and J. Lu, in three categories based on the mechanism of formation of the nanostructure, i.e., nanocrystallization by surface coating/deposition, surface self-nanocrystallization (SSN), and hybrid surface nanocrystallization, as shown in Fig. 3.1.

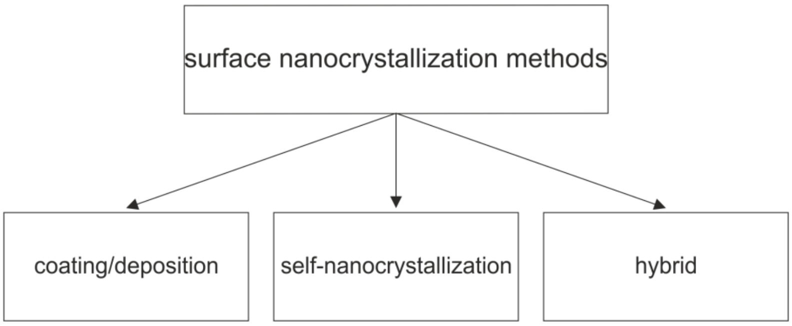

Figure 3.1 Surface nanocrystallization methods.

The first methods are based on coating deposition technologies such as, e.g., magnetron sputtering or PVD [26,27]. The obtained coating, can be made of the same material as the substrate or not and consists of nano-particles or powders with nano-sized grains. Those methods are usually used to obtain coatings with desired properties without changing the properties of the substrate.

The second type of methods are used to refine the material surface to a NC regime. Those processes may be referred to as self-nanocrystallization and they are carried without changing the chemical or phase composition of the substrate. The structure refinement can be induced through mechanical processing techniques, based on, e.g., SPD, or it can be induced thermally by melting and/or solidification. During the treatment, the top layer of the base material experiences microstructural changes. Those changes may include recombination of grain boundaries and change of grains orientation, creation of dislocation arrays, and their annihilation. Those processes result in the refinement of grains of the matrix into the gradient microstructure containing nano- and ultra-fine grains, as well as deformed coarse grains. The obtained nano-layer often strengthens the material to a much greater extent than the base bulk material. The nanostructured surface is usually resistant to fatigue crack growth and often induces the formation of a corrosive resistant passivation layer. The common methods of SSN include, e.g., ultrasonic sonic shot peening (USSP), high-speed rotation wire-brushing (HRWB), SMAT, and LSP [28,29]. The last two methods, i.e., SMAT and LSP are discussed further.

The last category of techniques combines the production of the nanostructured layer with chemical, or metallurgical processes [30]. These processes are used to create a compound with the different chemical composition of phases from those of the matrix [31].

In comparison to other methods of SN, the SSN is much simpler in use and the cost of equipment needed is relatively low. The created nano-layer is dense and has an identical chemical composition as the matrix. The gradual transition from nano- to coarse grains eliminates the problem of potential detaching of the deposited layer from the matrix as it could occur in the case of the coating deposition methods. What is more, the nano-layer created via SSN has superior mechanical properties and can greatly enhance the performance of polycrystalline materials.

3.3 Shot peening methods

Among methods of SN, SPD methods based on variations of high-frequency multidirectional impacts of shots or peens are quite popular. The concept of material peening is not new. People discovered long ago that work-hardening makes the metal harder and more durable. It is worth mentioning that originally the English word peening meant hitting with a small hammer. The process was already used in forging to strengthen armor, swords, and tools in the Early Bronze Age. If we look at the history of cold working, the oldest known example of such metal forming (in this case hammering) is a golden helmet believed to have been made for king Meskalamdug from 2600-

2300 BC found in the ancient Sumerian city of Ur [32]. It is clear that peening processes evolved during the past century, however, the idea remained the same. Nowadays SP methods consist of hitting the surface of the workpiece with high-velocity shots, peens, and in some sense, laser beams just like it used to be with a hammer.

SP methods are cold working processes widely used in automotive and aerospace industries to create compressive residual stresses close to the surface and the work hardening on the surface of the workpiece [33]. They owe their popularity to the ease and the low cost of their applicability, as well as, plentiful classes of materials whose properties can be enhanced. By using SP methods, it is possible to obtain a nanostructured layer with enhanced properties on the surface of polycrystalline materials. Those methods are well known to increase the lifetime and performance of mechanical components and structural elements [34].

3.3.1 Surface mechanical attrition treatment

SMAT or USSP is SPD method that can produce a hard layer of gradient NC microstructure in the treated surface [35,36]. The method shares the same features with conventional air blast shot peening, i.e., the surface microstructure modification is induced by repeated impacts of high-velocity spherical shots of a few millimeters in diameter on the treated surface. In both methods, the shots randomly hit the sample surface causing plastic deformation of the material and the entire process is an example of a cold working process. Multidirectional impacts induce grain refinement to the nanometer scale near the target surface. The main differences are the size of the shot (from 0.25 mm to 1 mm for SP and 1 mm to 8 mm for SMAT) and speed (from 20 m/s to 150 m/s for conventional SP and from 3 m/s to 20 m/ s for SMAT) [37]. Also, the shape of the shot is not the same - the one used for SMAT is spherical, while in the SP the shot used is often different and has irregular shapes. Another difference is in the device used to propel the shot. In SMAT, the shots and the processed material are placed in a closed chamber made of steel and are vibrated with a very high frequency using a vibration generator. The vibration frequency of the chamber is in the range from 50 Hz to 20 kHz. While in conventional SP pneumatic, centrifugal, or vapor blast machines are used to accelerate shots. These differences result in different characteristics and mechanical properties of surface microstructure produced.

The principles and the equipment used in SMAT are shown in Fig. 3.2. The equipment consists of the ultrasonic generator – sonotrode which sets in motion the steel chamber which as a result propels the shots. The sample is securely attached to the wall of the chamber as seen in Fig. 3.2.

The residual stresses introduced and the structure of the created nanostructured layer depend strongly on the chosen parameters of the process, such as shot size, velocity, and material which they are made of, as well as surface coverage during the process. While the choice of these parameters depends on the chosen vibration amplitude. What is more, the effects of SMAT strongly depend on the type of workpiece material and its mechanical and physical properties. SMAT generates a large number of defects such as dislocation and deformation twins and as a consequence refines the topmost layer of the sample to the nanometer scale. SMAT introduces local SPD to a target surface without changing the properties of the whole volume of the workpiece hence it requires less energy in comparison to the methods of bulk nanocrystallization. For example, ECAP requires the use of large loads and specially designed dies [38]. Due to this fact, SMAT can be considered environmentally friendly [39].

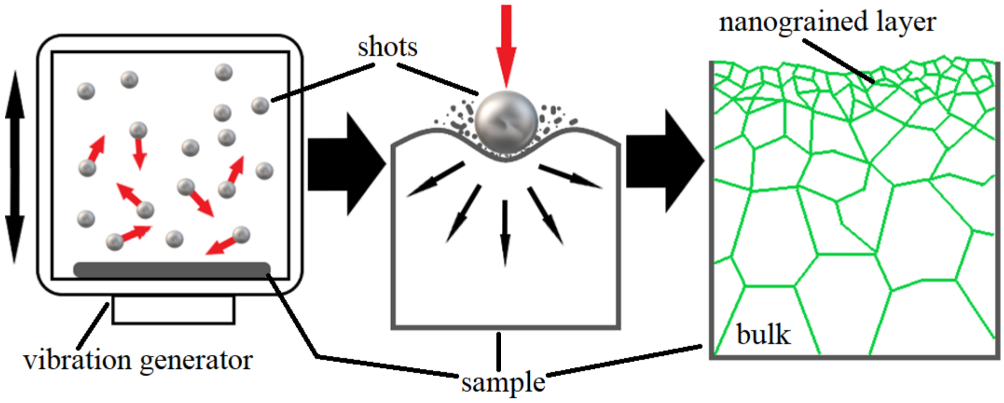

Figure 3.2 A conceptualization of the SMAT method.

3.3.2 Laser shock peening

LSP is a cold working technology where laser pulses hit the surface of the workpiece resulting in shock wave generation inside it [40-42]. The application of the method leads to the production of refined gradient structure beneath the treated surface [43]. The method is known to improve significantly fatigue performance, resistance to fretting, and resistance to corrosion of metallic components [44].

In the LSP method, laser pulses are used to heat and ionize the target surface or ablative layer covered with a thin layer of transparent material, usually, water or glass, turning it into rapidly expanding plasma which generates a high pressure on the surface, and consequently a shockwave in the target material [45]. When the pressure exceeds the dynamic yield strength of the material, there occur plastic deformation and the introduction of uniaxial compressive residual stresses beneath the treated surface, in the direction of the shock wave propagation. The plastic deformation results in the production of a great number of dislocations, as well as, their movement, which greatly affects the microstructure and through this the properties of the material [46]. To increase the magnitude of introduced compressive residual stresses in the workpiece, it is not enough to simply increase the laser power. Instead, the target is irradiated with repeating laser impacts that overlap. The reason for this is the fact that above a certain laser pulse energy level the plasma is not generated on the surface of the target but in the overlay layer. The principle of the LSP method is shown in Fig. 3.3.

Usually, Nd: YAG (Neodymium-doped Yttrium Aluminum garnet) Q-switched laser systems are used for the material surface modifications, with 1064 nm (near infra-red), but also 532 (green) and 355 (ultraviolet) nm wavelength. Laser pulse length ranges from 10 to 100 ns, with energies of 1-100 J [46]. The different laser spot geometries, including, circular, elliptical, rectangular, and square with the size ranging from 1 to 6 mm are used [47]. A frequency of less than 1 kHz is preferred. The transparent confining layer ensures that plasma is kept near the surface of the target. Those layers can be water, quartz, or glass, and their choice depends on the substrate material [47]. The protective coating vaporizes during the process instead of the underlying material [46]. It prevents thermal exposure, surface melting, and laser ablation, which may result in the development of undesirable tensile residual stresses, as well as poor surface finish. This layer can be made of aluminum, vinyl tape, zinc, copper, or black paint [47]. However, the application of protective coatings is not always easy due to the shape of the workpiece or during in-situ applications. Hence, the laser shock peening without coating (LSPwC) method was developed [48]. In this method, the protective coating is not used and much smaller energies of laser pulses and an increased number of pulses over the peened area are used.

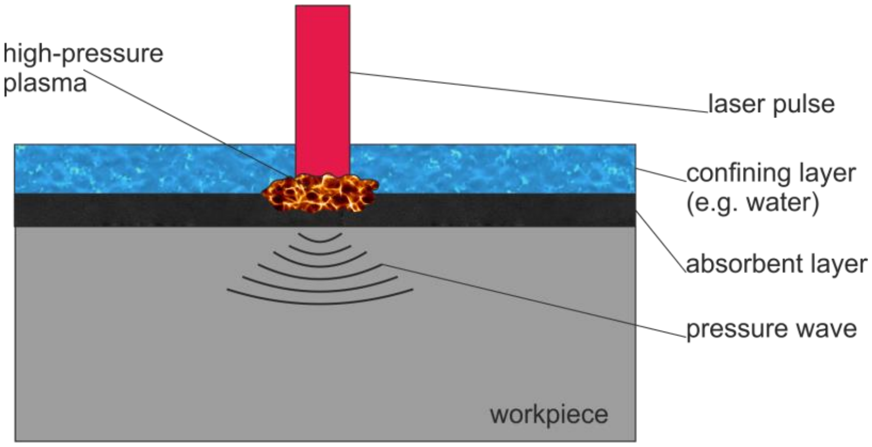

Figure 3.3 A schematic diagram of the mechanism of the LSP procedure.

LSP can be used to modify different materials, including hard and soft metals, and thin films. It is a relatively new surface modification process used in the aerospace and automotive industries [47,49]. It is extensively used in aerospace, e.g., to enhance the service time of wide-chord fan blades for commercial aircrafts [50]. An interesting application of LSP in the aerospace industry is the in-situ repair of the Lockheed Martin F-22 Raptor wing lug instead of replacing it [51,52]. The technology has been also applied, i.e., LSPwC, as a maintenance method to Japanese BWRs (boiling water reactor) and PWRs (pressurized water reactor) nuclear power reactors to prevent stress corrosion cracking of steel-made elements since 1999 [53,54].

The effects of LSP application on the metal microstructure can be compared to those that can be obtained by SMAT or USSP. LSP technique is considered as a potential substitute to SP. In comparison to a conventional SP, much higher, as well as, deeper compressive residual stresses can be introduced inside the target material and a much better, uniform surface finish can be obtained [55]. What is more, the distinctive benefit of LSP is that the method is capable of treating workpieces with complex geometries that are not accessible to SP, which makes it useful for specialized applications, such as, e.g., prosthetics [56-58]. The undoubtful advantage of LSP, compared to methods based on peening the surface with blasting material, is that it does not introduce eventual surface contamination [59]. Extensive commercial and scientific efforts are being put into the optimization and the standardization of LSP technology [60].

References

1. K.V. Rajulapati, C.C. Koch, Nanocrystalline Materials: Mechanical Properties, Reference Module, in: Materials Science and Materials Engineering, Elsevier, 2016.
2. R.Z. Valiev, R.K. Islamgaliev, I.V. Alexandrov, Prog. Mater. Sci. 45 (2000) 103.
3. K. Lu, Science 345 (2014) 1455.
4. Y. Estrin, A. Vinogradov, Int. J. Fatigue 2010, 32 (2010) 898.
5. S.M. Fatemi-Varzaneh, A. Zarei-Hanzaki, H. Paul, Mater. Charact. 87 (2014) 27.
6. N. Birbilis, K.D. Ralston, S. Virtanen, et al. Corros. Eng. Sci. Techn. 2010, 45 (2010) 224.
7. B. Chen, G. Zhang, L. Zhang, T. Xu, Int. J. Adv. Manuf. Technol. 94 (2018) 2659.
8. P. Chui, K. Sun, C. Sun, et al. Appl. Surf. Sci. 257 (2011) 6787.
9. A.P. Zhilyaev, T.G. Langdon, Progress in Materials Science 53, (2008) 893.
10. K. Miyata, M. Wakita, S. Fukushima, M. Eto, et al. Mater. Sci. Forum 539 (2007) 4698.
11. M. Cheepu, S. Haribabu, T. Ramachandraiah, et al. Appl. Mech. Mater. 877 (2018) 183.
12. Y. Samih, B. Beausir, B. Bolle, T. Grosdidier, Mater. Charact. 83 (2013) 129.
13. K. Lu, J. Lu, Mat. Sci. Eng. A 375 (2004) 38.
14. R. Sundar, P. Ganesh, R.K. Gupta, et al. Mater. Process. 6 (2019) 424.
15. S. Bagheri, M. Guagliano, Surface Engineering, 25 (2009) 3.
16. M., Z. Issaabadi, M. Sajjadi, S.M. Sajadi, et al. Types of Nanostructures, in M. Nasrollahzadeh, S.M. Sajadi, M. Sajjadi, Z. Issaabadi, M. Atarod (eds.): Interface Science and Technology, Elsevier, Volume 28, 2019.

17. A.K. Mukherjee, R.S. Mishra, Superplasticity, in K.H. Jürgen Buschow, R.W. Cahn, M.C. Flemings, B. Ilschner, E.J. Kramer, S. Mahajan, P. Veyssière (eds.): Encyclopedia of Materials: Science and Technology, Elsevier, 2001, 8977.
18. A.K. Giri, K.A. Darling, S.M. Walsh, Structural power, energy, actuation, and mobility in intelligently directed systems enabled from nanocrystalline metals, in S.M. Walsh, M.S. Strano (eds.): Woodhead Publishing in Materials, Robotic Systems and Autonomous Platforms, Woodhead Publishing, 2019, 449.
19. S.N. Naik, S.M. Walley, J. Mater. Sci. 55 (2020). 2661.
20. C.S. Pande, K.P. Cooper, Prog Mater Sci 54 (2009) 689.
21. P.B. Koli, K.H. Kapadnis, U.G. Deshpande, J. Nanostruct. Chem. 9 (2019) 95.
22. A.A. Agrawal, B.J. Nehilla, K.V. Reisig, T.R. Gaborski, et al., Biomaterials 31 (2010) 5408
23. L. Zhang, N. Yan, Z. Yao, Z. Sun, et al. Int. J. Hydrogen Energy 45 (2020) 28134.
24. N. Barkalina, C. Charalambous, C. Jones, K. Coward, Nanomedicine: NBM 10 (2014) 921.
25. K. Lu, J. Lu, J. Mater. Sci. Technol. 15 (1999) 193.
26. M. Qadir, Y. Li, C. Wen, Acta Biomateriali 89 (2019) 14.
27. A. Baptista, F. Silva., J. Porteiro, J. Míguez, G. Pinto, Coatings 8 (2018) 402.
28. F. Yin, M. Rakita, Sh. Hu, Q. Han, Surf. Eng. 33 (2017) 651.
29. D. Song, A. Ma, W. Sun, J. Jiang, et al., Corros. Sci. 82 (2014) 437.
30. R. Zhang, Y. Wan, X. Ai, T. Wang, B. Men, Trans. Nonferrous Met. Soc. China 26 (2016) 1019,
31. F.L. Yang, D. Song, A.B. Ma, J.H Jiang, Z.J. Cheng, MSF 956 (2019) 160.
32. M. Molina Martos, The royal tombs of Ur revealed Mesopotamia’s golden splendor https://www.nationalgeographic.com/history/world-history-magazine/article/mesopotamia-ur-royal-tombs accesed on 20.02.2021
33. A. Azhari, S. Sulaiman, A.K. Prasada Rao, IOP Conf. Ser.: Mater. Sci. Eng. 114 (2016) 012002
34. S. Bagheri, M. Guagliano, Surf. Eng. 25 (2009) 3.
35. Y. Samih, B. Beausir, B. Bolle, T. Grosdidier, Mater. Charact. 83 (2013) 129.
36. K. Lu. J. LuJ. Mat. Sci. Eng. A 375 (2004) 38.
37. D. Gallitelli, D. Retraint, E. Rouhaud, AMR 996 (2014) 964.
38. S. Bagherzadeh, K. Abrinia, Q. Han, Mater Lett. 169 (2016) 90.
39. G. Gupta, S. De, A. Franco, A.M. Balue, et al., Molecules. 21 (2016) 1.
40. B.P. Fairand, A.H. Clauer, J. Appl. Phys. 50 (1979) 1497.
41. A.H. Fairand, B.P. Clauer, Interaction of laser-induced stress waves with metals, in: Proceedings of the ASM Conference Applications of Lasers in Materials Processing, USA, Washington, DC, 18–20 April 1979, ASM International: Materials Park, OH, USA, 1979.
42. C.A. Askaryan, E. Moroz, Theor. Phys. 43 (1962) 2319.
43. W. Zhou, X. Ren, F.Liu, Y. Ren, L. Li, Metals 6 (2016) 297.
44. J.L. Hu, J. Lou, H.C. Sheng, S.H. Wu, et al. Open J. Adv. Mater. Res. 347 (2011) 1596.
45. M. Ebrahimi, S. Amini, M. Mahdavi Seyed, Int. J. Adv. Manuf. Technol. 88 (2017) 1557
46. C. Montross. T. Wei, L. Ye, G. Clark, Y. Mai, Int. J. Fatigue 24 (2006) 1021.
47. A.K. Gujba, M. Medraj, Materials 7 (2014) 7925.
48. D. Karthik, S. Swaroop, Mater. Manuf. Process. 32 (2017) 1565.
49. P. Ganesh, R. Sundar, H. Kumar, R. Kaul, et al. Opt Lasers Eng. 50 (2012) 678.

50. S. Mannava, A.E. McDaniel, W.D. Cowie, Laser shock peened rotor components for turbomachinery. US Patent 5,492,447, 20 Feb 1996, General Electric Company (Cincinnati, OH).
51. K. MacGillivray, et al. F-22 Laser Shock Peening Depot Transition and Risk Reduction, USAF ASIP Conference, San Antonio, TX, Dec 2010. http://meetingdata.utcdayton.com/agenda/asip/2010/proceedings/presentations/P4237.pdf, (accesed on 01.03.2021)
52. M. Hill, et al. Design and Analysis of Engineered Residual Stress Surface Treatments for Enhancement of Aircraft Structure, USAF ASIP Conference, San Antonio, TX, Nov 2012. http://meetingdata.utcdayton.com/agenda/asip/2012/proceedings/presentations/P6614.pdf, (accesed on 01.03.2021).
53. Y.J. Sano, N. Mukai, I. ChidaI, et al. Applications of laser peening without protective coating to enhance structural integrity of metallic components. The 2nd international laser peening conference, San Francisco CA, 19–22 April 2010.
54. Y. J. Sano, M. Obata, T. Kubo , N. Mukai, M. Yoda, K. Masaki, et al. Mater. Sci. Eng. A 417 (2006) 334.
55. P. Peyre, X. ScherpereelX. L. Berthe, C. Carboni, R. Fabbro, G. Béranger, C. Lemaitre, Mater. Sci. Eng. A 280 (2000) 294.
56. Y. Guo, M.P. Sealy, C. Guo, CIRP Annals 61 (2012) 583.
57. K. Gurusami, K.S. Sundaram, D. Chandramohan, et al. Int. J. Ambient Energy (2019) 1614987
58. M.P. Sealy, Y.B. Guo, R.C. Caslaru, J. Sharkins, D. Feldman, Int. J. Fatigue 82 (2016) 428.
59. D. Fabijanic, A. Taylor, K.D. Ralson, et al. Corrosion 69 (2013) 527.
60. A.H. Clauer, Metals 9 (2019) 626.

Chapter 4: Principles of positron annihilation spectroscopy

The first experiments with the use of positrons concerned the study of the Fermi surface in metals and alloys [1]. Measurements of the angular correlation curve of annihilation quanta in gold carried out in 1949 by De Benedetti and his colleagues [2] and registration of DB of the 511 keV annihilation line by DuMond and his team [3] are considered as the beginning of the application of PAS for condensed matter studies. Since then, the method has found application in the study of various materials.

PAS techniques provide a non-destructive and unique way to study open volume defects, the porosity of the material, and the surface layer. Due to their low mass, positrons can penetrate larger volumes of the samples without damaging them in comparison to heavier particles. Positrons are sensitive to sites with lower electron density such as crystal lattice defects and may become trapped by them. PAS is a good method that allows a qualitative and quantitative description of changes (such as, for example, the density of defects or their type) in the microstructure of the material. What is more, it can be successfully used to determine pores sizes and their distribution inside molecular media. The undoubted advantage of the PAS methods is that they enable in situ measurements of the changes of the material properties, e.g., during annealing. So-called slow positron beams are popular amongst solid-state researchers. The method enables the implantation of positrons with precisely defined energies into the sample.

Nowadays, positrons found applications in several, different areas of science. One of the most well-known is Positron Emission Tomography (PET) [4]. PET is a medical imaging technique that has found applications in important areas of clinical diagnosis such as cancer diagnosis and management, cardiology and cardiac surgery, neurology, and psychiatry.

4.1 Positron sources

In 1928, English theoretician Paul Adrien Maurice Dirac predicted the possibility of the existence of an electron antiparticle – positron [5,6], which was later observed by the American physicist Carl David Anderson [7,8]. A positron is an antimatter elementary particle. It is a lepton, denoted with the e^+ symbol. The positron electric charge is equal to the elemental electric charge and its mass is the same as an electron. Positron belongs to fermions and it has a spin equal to 1/2.

4.1.1 β+ Radioisotopes

Isotopes that undergo β^+ decay are the most conveniently available sources of positrons that are used in laboratories. During the β^+ decay, under the influence of weak interactions, one of the protons in the atomic nucleus is transformed into a neutron. It is accompanied by the emission of fast energetic positron and neutrino: $p \rightarrow n + e^+ + \nu_e$. The positron emitted in the β^+ decay has a continuous energy spectrum, ranging from zero to the end-point energy which is typical of the order of 0.1 – 1 MeV. Hence its energy is in a certain range that characterizes a given isotope. In nature, there are about 200 radioactive isotopes that decay through the β^+ process with the emission of positrons. Despite this, only a few of them are used as positron sources in the PAS method. The isotopes such as, e.g., ^{22}Na, ^{44}Ti/^{44}Sc, ^{68}Ge/^{68}Ga, are commonly used. In selecting sources for PAS purposes, a key role plays their efficiency and relatively long half-life time $T_{1/2}$.

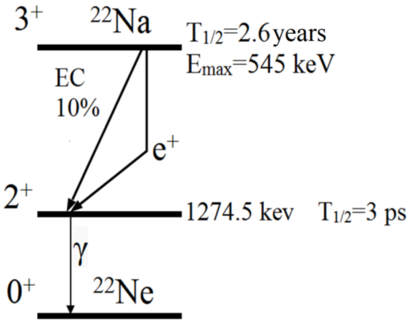

Figure 4.1 ^{22}Na isotope decay scheme

A convenient positron source used in PAS measurements is ^{22}Na. It can be produced by irradiating aluminum or magnesium targets with high energetic protons [9-11]. ^{22}Na isotope has $T_{1/2}$ = 2.62 y and the decay efficiency with positron emission of 90.6% [12]. The maximum energy of positron emitted from ^{22}Na is 0.545 MeV [12]. The ^{22}Na decay scheme is shown in Fig. 4.1. The decay can go straight to the ground state and by the excited state of the nucleus of ^{22}Ne. In the case of ^{22}Na, 99.94% of positrons are emitted through the excited state of ^{22}Ne. This state is stable for about 3 ps followed by the emission of a gamma photon with an energy of 1274.5 keV. Due to its properties, this isotope is widely used in PAS techniques, especially in positron annihilation lifetime spectroscopy (PALS), which is discussed in Chapter 4.4.1.

4.1.2 Pair production

It is worth mentioning that, positrons can be produced in pair production phenomena in which a gamma ray interacts with a nucleus of an atom. In the process, pairs of matter and antimatter particles are produced [13]. The incoming gamma ray must have the energy equivalent to at least the rest mass of the resultant particles. The required energy for positron-electron pair production has to be equal to 1.02 MeV or higher.

4.2 Positron interaction with matter

4.2.1 Thermalization

A positron that has been implanted into solid matter loses its kinetic energy in a process called thermalization. During this process, positrons lose information about the initial direction of their motion. High-energy positrons (over 100 keV) lose their energy the fastest – 1 MeV/s; in the range between 100 eV and 100 keV, the energy loss rate is about 100 keV/ps [14]. Such energetic positrons lose their energy through elastic and non-elastic collisions with electrons, ionization, and emission of Bremsstrahlung radiation. For energies lower than 100 eV, positrons lose their energy via excitation of valence electrons, plasmon excitations, and the production of electron-hole pairs. If the positron energy is less than 2 eV, it slows down mainly due to scattering on acoustic phonons. Positron loses its energy until it is in thermal equilibrium with its environment, reaching energy E_{kin} = 3/2 kBT ≈ 40 meV at room temperature, which is smaller than the average Fermi energy, i.e, 10 eV, in metals. In spite of a massive change in the kinetic energy of positron, the time of the thermalization process usually takes less than a few picoseconds.

It is worth mentioning that, some amount of positrons annihilate without reaching thermal equilibrium, i.e., in-flight [15]. However, this phenomenon is of minor importance in this study.

4.2.2 Positron implantation range

Relatively high-energetic positrons emitted from β+ sources that have been implanted to the sample traverse a significant distance inside it. For positrons emitted from a radioactive source, the positron intensity $P(z)$, i.e., the number of positrons at the depth between z and z + dz, decreases with the depth z as follows:

$$P(z) = P(0)\exp(-\alpha_{+}z), \tag{4.1}$$

where z is the depth below the surface of target material, ρ stands for the target's density, α_{+} is the linear absorption coefficient which for positrons emitted from ^{22}Na can be denoted in the following form, proposed by Dryzek and Singleton [16]:

$$\alpha_+ = 12.6\rho Z^{0.17}/E_{max}^{1.28}\ [\mathrm{cm}^{-1}], \tag{4.2}$$

where ρ is the density of material in which the positron travels expressed in g/cm^3, E_{max} is the maximal energy of emitted e$^+$, and Z is the atomic number of the target material. As it can be seen, $P(z)$ depends on material density and the maximum energy of positrons characteristic for a given β$^+$ source. Table 4.1 shows values of α_+ for chosen metals.

Table 4.1 Sample values of linear absorption coefficient α_+ [16,17].

material	**density [g/cm^3]**	**α_+ [cm^{-1}]**
Mg	1.74	75.7 (1.1)
Ti	4.5	222.4 (6.9)
Cu	8.96	387.9 (36)
Fe	7.87	322.6 (5.6)

The mean implantation range for positrons emitted from ^{22}Na source $\bar{z}$ can be defined as [18]:

$$\bar{z} = \frac{1}{\alpha_+}. \tag{4.3}$$

For mono-energetic positrons produced by variable energy positron (VEP) beams, the implantation profile can be described by the Makhov function [19-21]:

$$p(z,E) = \frac{mz^{m-1}}{z_0^m} exp\left[-\left(\frac{z}{z_0}\right)^m\right], \tag{4.4}$$

where z is the depth from the surface, m and z_0 are the parameters. The shape parameter m is nearly constant (~1.9), it slightly decreases as a function of the atomic number of the target. The penetration parameter z_0 is a function of the incident energy E of positrons and can be described as:

$$z_0 = \frac{A}{\rho\Gamma(1+1/m)}E^n = \frac{A_{1/2}}{\rho(ln2)^{1/m}}E^n, \tag{4.5}$$

where n is a parameter, Γ is a gamma function, which in most cases is almost equal to 2. The Makhovian profile parameters n, m, A, obtained from Monte Carlo simulations using GEANT 4 code are reported in ref. [22]. The average range of positrons implanted with the incident energy E into a material with a density of ρ is determined according to the following formula:

$$\bar{z} = \frac{AE^n}{\rho}. \tag{4.6}$$

It is worth mentioning that, in the case of low implantation energies, i.e., lower than 1 keV, some fraction of partially thermalized positrons can exit probed material. Those positrons are called epithermal [23].

4.2.3 Positron diffusion

After reaching thermal equilibrium with the host, the positron diffusion process starts, during which, the positron undergoes scattering mainly on acoustic phonons, but also electrons, ions, or crystal lattice defects. At this stage, the positron traverses an area of about 10^7 atoms [24].

The average positron diffusion length L, which can be interpreted as the mean square path that the positron randomly traverses in the material until its annihilation can be defined as follows:

$$L = \sqrt{6D_+\tau_\mathrm{f}}, \tag{4.7}$$

where D_+ is the positron diffusion coefficient, τ_f is the lifetime of free positrons, i.e., positrons that annihilate in a perfect crystal lattice from a delocalized state. During the diffusion process, the positron traverses a much shorter distance in comparison to that during thermalization. Positron diffusion is a particularly important process, it enables the positron, to form a bound state in one of the defects in the crystal lattice where it annihilates with electron.

4.2.4 Positron annihilation

As an anti-particle of an electron, positron annihilates with an electron resulting in the conversion of electron-positron mass into the equivalent energy of gamma photons. During the process, the energy, parity, charge, and momentum of the annihilation pair are conserved.

The positron-electron pair annihilation can be done in several ways. The most likely process is annihilation resulting in the production of two gamma quanta with specific energies equal to 510.995 ± 0.012keV. About 99.7% of all cases are processes in which two gamma quanta are emitted. Annihilation with the production of more than two quanta is also possible however a cross-section for this phenomenon is far lower than for a two-quantum process [25]. The cross-section $\sigma_{2\gamma}$ calculated by Dirac for the process of annihilation of the positron-electron pair with the production of two gamma photons shows the following formula:

$$\sigma_{2\gamma} = \frac{\pi r_0^2}{\gamma+1}\left(\left(\frac{1+4\gamma+\gamma^2}{\gamma^2-1}\right) ln\left(\gamma + \sqrt{\gamma^2-1}\right) - \frac{3+\gamma}{\sqrt{\gamma^2-1}}\right), \quad (4.8)$$

where, $\gamma = \frac{1}{\sqrt{1-\frac{v^2}{c^2}}}$, v is the speed of the positron, and c is the speed of light, r_0 is classical electron radius, m_0 is electron rest mass. In the range of low speeds, the above formula can be simplified and expressed in the following form:

$$\sigma_{2\gamma} = \frac{\pi c r_0^2}{v}. \quad (4.9)$$

For the annihilation rate λ with two γ quanta the following relationship applies:

$$\lambda_{2\gamma} = \sigma_{2\gamma} v = \pi c r_0^2 n_e, \quad (4.10)$$

where $\sigma_{2\gamma}$ is the cross-section for two γ annihilation, v is the positron velocity, n_e is the electron density, c is the speed of light, r_0 is the radius of the electron, $r_0 = e^2/m_0c^2$. The positron lifetime defined as the reciprocal of the annihilation rate, $\tau = 1/\lambda$ depends only on the electron density at the positron location. In general, this is valid for the unpolarized material.

4.2.5 Doppler broadening

As it was mentioned, the annihilation of a positron-electron pair results in the production of two identical 511 keV photons that are emitted in opposite directions in the center of mass frame. Nevertheless, in the laboratory frame of reference, there is a deviation from the gamma emission collinearity. This phenomenon results from the momentum in the new frame of reference, as shown in Figure 4.2. This is caused by the same Doppler shift effect that also applies to the phenomenon related to the change of the frequency of the waves emitted by a moving source relative to an observer. In the case of PAS, such a moving source is an annihilating positron-electron pair that has got some momentum that is approximately equal to the momentum of an electron. This assumption can be made because the value of momentum of a thermalized positron is even three orders smaller than the value of momentum of an electron. Hence, the distribution of the momentum and energy of the annihilation quanta carries information about the momentum and energy of the electrons. Due to this, it is possible to study the electron structure of solids and identify places, e.g., defects, in which electron density is lower than in defect-free lattice, i.e., defects.

In the center of mass reference frame, energies of annihilation quanta are equal to:

$$E_0 = m_0c^2 - \frac{1}{2}E_b, \qquad (4.11)$$

where E_b is positron-electron binding energy, relatively low in comparison to m_0c^2, which is equal to 511 keV. While in the laboratory frame of reference, the motion of the annihilating pair causes a Doppler shift. The positron-electron pair has a certain momentum p, therefore the observed direction and angle of gamma quanta emission changes. Annihilation quanta deviate from collinearity by a certain angle dθ which can be approximated by the formula [26]:

$$d\theta \cong \theta_1 - \theta_2 \cong \frac{p_\perp}{m_0c^2}, \qquad (4.12)$$

where $p_\perp$ is the projection of momentum of the positron-electron pair on the direction perpendicular to the direction of gamma quanta emission, as shown in Fig. 4.2. Assuming that the speed of the annihilating pair is much smaller than the speed of light c, the energies E_1 and E_2 in the laboratory frame of reference can be expressed by:

$$E_{1,2} \approx m_0c^2 - \frac{1}{2}E_b \pm \frac{cp_L}{2}, \qquad (4.13)$$

where p_L is the component of the momentum along the gamma quantum emission direction, ass seen in Fig. 4.2.

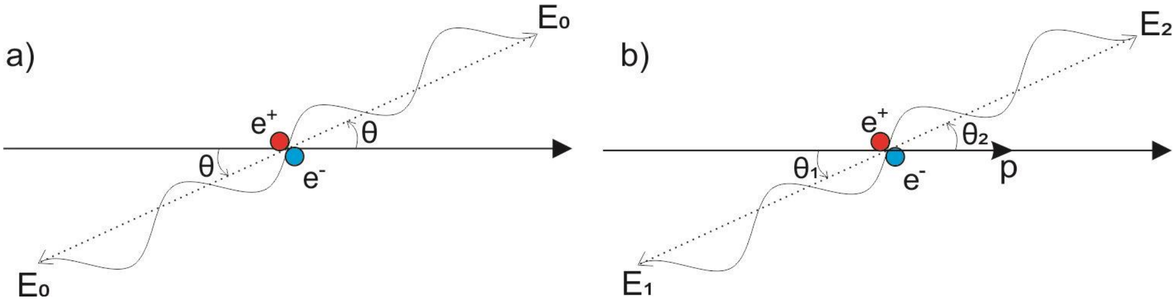

Figure 4.2 Positron-electron pair annihilation in a) the center of mass reference frame, b) in the laboratory frame of reference.

Measuring the angle of deviation from collinearity is the basis of one- and two-dimensional angular correlation spectrometry of annihilation quanta. As it was shown, the momentum component parallel to the direction of the emitted photons leads to an energy shift of the annihilation radiation in the laboratory frame of reference. This is the basis of DB spectroscopy, which is discussed in Chapter 4.4.2.

4.3 Positron trapping in defects

A positron implanted into an ideal crystal lattice will annihilate from the free-state, i.e., one that can be described by the Bloch function, which is a solution of the Schrödinger equation with periodic potential. However, this repeating pattern is not always preserved and as a result of various phenomena, crystal lattice defects may appear in it. Open volume defects, i.e., vacancies or their clusters are the dominant types of imperfections that can trap positrons. Due to a reduction in repulsion by the positive ions that are absent in this type of defects, they create an attractive potential for the thermalized positron. A positively charged positron interacts with vacancies in such a way that they are places of a lower potential for the positron than in an ideal, defect-free lattice. The positron wave function is localized in such defects if its energy is lower than in the delocalized state. Then a positron localized state is created. The transition between delocalized and localized to a point defect state is called trapping of the positron. The difference in energy between the initial and trapped state can be called the positron binding energy in the defect. In metals, the value of binding energy in vacancies and their clusters is typically around a couple of eV (1 to 5 eV), and a thermal escape of positron is not possible. Those defects can be called deep positron traps, from which positron cannot normally escape. Fig. 4.3 shows a schematic representation of the positron interaction potential with ions of the crystal lattice. The bottom of the band occupied by the thermalized positron is marked with a dotted line in Fig. 4.3. As it can be seen defect acts like deep positron traps because positrons can reach lower potential in them. What is more, open volume defects are places with lowered electron density n_e. Due to this, the annihilation rate is lower according to equation 4.10. This, in turn, increases the positron lifetime which is inversely proportional to the annihilation rate $\tau = 1/\lambda$. On the other hand, due to thermal excitation, a trapped positron can escape from so-called shallow traps in a process called detrapping. This type of defects includes, e.g., dislocation lines in metals and Rydberg states around negatively charged ions in semiconductors, where the positron binding energy is weak, i.e., less than 1 eV [27]. The standard trapping model provides a simple view of the effect of positron trapping by defects in the metal structure.

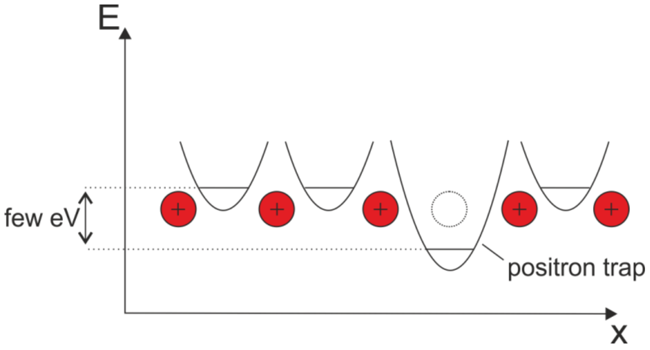

Figure 4.3 Schematic representation of the positron interaction potential with positively charged ions, and defects of the crystal lattice.

4.3.1 Standard trapping model

Description of the trapping process in solids is possible within the so-called trapping model [28-29]. The key assumptions of the model are given below:

- at the initial state (t = 0), positrons that are present in the system diffuse freely in the crystal, i.e., they are in Bloch states from which they can annihilate with the speed given by the equation:

$$\lambda_f = \frac{1}{\tau_f}, \tag{4.14}$$

  where τ_f is the positron lifetime in an ideal, defect-free crystal lattice,
- all defects are distributed homogeneously in the sample material,
- trapping of positrons in defects occurs with the trapping rate κ:

$$\kappa = \mu \cdot c_{trap}, \tag{4.15}$$

  where μ is a trapping coefficient, which characterizes a specific type of defect and it is expressed in s^{-1} [30]; c_{trap} stands for a defect concentration (number of defects / number of atoms in the lattice).

The crystal lattice of the sample contains N number of defects, at t = 0 the number of free positrons $n_f = n_p$ and the number of trapped positrons n_d = 0, j = 1,…,N. The number of positrons remaining in the Bloch state as a function of time is given by the equation:

$$\frac{dn_f(t)}{dt} = -\lambda_f n_f(t) - \sum_{j=1}^{N} \kappa_j n_f(t). \tag{4.16}$$

The number of positrons trapped in the jth type of defects as a function of time is given by:

$$\frac{dn_d(t)}{dt} = -\lambda_j n_d(t) + \kappa_j n_f(t), \tag{4.17}$$

where λ_j is the positron annihilation speed in the jth state

The least complicated variant of the model is the so-called two-state model, which can be used to describe the positron annihilation in case of one type of defect present in the medium. It can be used to describe trapping in thermally generated vacancies in ionic crystals and open volume defects in metals [31]. In this model, the positrons annihilate only from the free-state or from the state localized in the defects, and the positron escape from the localized state does not occur. The evolution of the number of positrons that are present in the medium can be given by:

$$\frac{dn_f(t)}{dt} = -\lambda_f n_f(t) - \kappa n_f(t), \tag{4.18}$$

$$\frac{dn_d(t)}{dt} = -\lambda_d n_d(t) + \kappa n_f(t), \tag{4.19}$$

Where n_f and n_d are the number of the positrons in the free state and trapped in the defect, respectively. While λ_f and λj are the positron annihilation speed in the free state and trapped in the defect, respectively. The total number of positrons present in the system decreases exponentially with time due to positron annihilation. After solving this differential system of equations, with all key assumptions of the standard trapping model, one can obtain:

$$n(t) = n_f + n_d = I_1 e^{-\lambda_1 t} + I_d e^{-\lambda_d t}, \tag{4.20}$$

where I_1 and I_d are the positron lifetime components and $\lambda_1 = \lambda_f + \kappa$. The total probability of positron annihilation can be given by:

$$P(t) = -\frac{dn}{dt} = I_1 e^{-\lambda_1 t} + I_d e^{-\lambda_d t}. \tag{4.21}$$

The model can be used to interpret the PALS measurement results. As it can be seen, the positron lifetime spectrum contains two components with the positron lifetimes $\tau_1 = 1/\lambda_1$ and $\tau_2 = 1/\lambda_d$; τ_1 is so-called reduced bulk lifetime, which is slightly shorter than τ_f, and τ_d is the positron lifetime in defects. The positron lifetime in defect-free material τ_f can be expressed by:

$$\tau_f = \frac{1}{\lambda_b} = \frac{1}{I_1\lambda_1} + \frac{1}{I_d\lambda_d}, \tag{4.22}$$

The lifetimes and their intensities can be obtained from measured spectra in PALS experiments, which is discussed further in Chapter 4.4.1.

A parameter that can be obtained in PALS experiments is the mean lifetime of positrons $\bar{\tau}$ defined as:

$$\bar{\tau} = \int_0^\infty dt\, n(t) = I_1\tau_1 + I_2\tau_2 = \frac{1+\kappa_d\tau_d}{1+\kappa_d\tau_f}\tau_f, \tag{4.23}$$

and

$$\tau_f = \frac{\tau_1\tau_2}{I_1\tau_1 + I_2\tau_2}, \tag{4.24}$$

where I_1 and I_2 are fractions of positrons annihilating from the free-state and the state trapped in the defect, respectively. The value of the mean positron lifetime higher than that for an ideal crystal lattice proves the presence of defects in the sample.

By decomposing the spectrum into its components, it is possible to calculate the parameters of the trapping model and thus identify the type of defects and determine their concentration. Determination of the lifetime values and their intensities makes it possible to distinguish the type of defects that are present in the media:

$$\kappa = \mu \cdot c_{trap} = I_2 \left(\frac{1}{\tau_1} - \frac{1}{\tau_d}\right), \tag{4.25}$$

where values of trapping coefficient μ can be found in the literature.

When there are two different types of defects, which means that a positron can annihilate from a free state or from a bounded state in one of the defect types that are present in the medium, a three-state model can be used. Similarly to the two-state model, the number of the positrons that are present in the media can be expressed by:

$$n(t) = n_f + n_{d1} + n_{d2} = I_1 e^{-\lambda_1 t} + I_{d1} e^{-\lambda_{d1} t} + I_{d2} e^{-\lambda_{d2} t}, \tag{4.26}$$

where λ_{d1}, λ_{d2} are positron lifetime values for a particular type of defect.

In the three-state model:

$$\tau_1 = \frac{\tau_f}{1+\tau_f(\kappa_{d1}+\kappa_{d2})}, \quad I_1 = 1 - I_2 - I_3, \tag{4.27}$$

$$\tau_2 = \tau_{D1}, \qquad I_2 = \frac{\kappa_{d1}\tau_{D1}\tau_f}{\tau_{D1}-\tau_f+(\kappa_{d1}+\kappa_{d2})\tau_{D1}\tau_f} \tag{4.28}$$

$$\tau_3 = \tau_{D1}, \qquad I_3 = \frac{\kappa_{d2}\tau_{D2}\tau_f}{\tau_{D2}-\tau_f+(\kappa_{d1}+\kappa_{d2})\tau_{D2}\tau_f} \tag{4.29}$$

$$\bar{\tau} = \frac{1+\kappa_{d1}\tau_{D1}+\kappa_{d2}\tau_{D2}}{1+\kappa_{d1}\tau_f+\kappa_{d2}\tau_f}\tau_f. \tag{4.30}$$

Same as in the two-state model, τ_1 is shorter than τ_f. Assuming that the third component differs significantly from the rest, which may occur in the presence of deep positron traps, e.g., when in the material studied vacancies and deeper traps - vacancy clusters are present, then measured $\tau_{1,\mathrm{exp}}$, and $\tau_{2,\mathrm{exp}}$ are expressed as follows:

$$\begin{gathered} \tau_{1,exp} = \frac{I_1}{I_1+I_2}\tau_1 + \frac{I_2}{I_1+I_2}\tau_2, \\ \tau_{2,exp} = \tau_{D2}, I_{2,exp} = I_3 \end{gathered} \tag{4.31}$$

Similar to the two-state model determination of lifetime values and their intensities makes it possible to distinguish the type of defects that is present in the medium.

As it can be seen, when τ_D values are longer than τ_f, hence, $\bar{\tau}$ is also longer, then it can be clearly stated that there are defects in the material studied.

4.4. Positron annihilation spectroscopy methods

4.4.1 Positron lifetime spectroscopy

The positron lifetime measurement consists of determining the time difference between the emission of the quantum resulting from the neon nucleus relaxation and the annihilation quantum. The radioactive sodium nucleus decays into the excited ^{22}Ne nucleus, which after about 3 ps is relaxed by the emission of a gamma quantum with the energy of 1275 keV. The moment of registering the quantum 1275 keV is attributed to the formation of the positron, and the registration of the 511 keV quantum - its annihilation. The idea of the measurement is shown in Fig. 4.4.

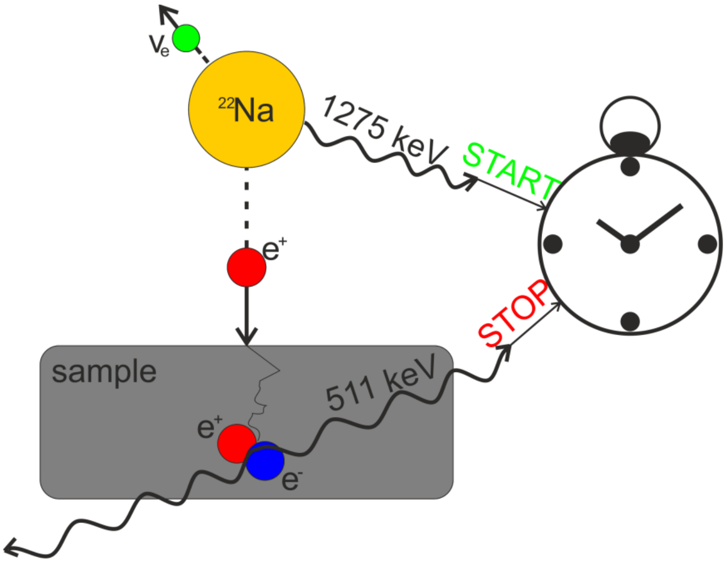

Figure 4.4 Scheme of positron lifetime measurement.

The schematic representation of the PALS setup is shown in Fig. 4.5. A positron source is placed between two identical samples and the sample-source system prepared in this way is placed in front of two scintillation counters (SC). One of the detectors registers the 1275 keV γ quantum, which is the signal to start counting the time. While the discriminator of the second one is set to register a 511 keV annihilation quantum which is the stop signal for the time counting. Electrical signals that are generated at the output of the photomultiplier tubes (PM) have amplitudes proportional to the energy of the registered quanta. These signals are processed by two differential constant fraction discriminators (CFDs) designed to transform the signals to be amplitude- and noise-independent. To shift the spectrum into the linear region of the time-amplitude converter (TAC), the pulse coming from the registration of the 511 keV quantum is sent to the delay line (DL). Then the multichannel analyzer (MCA) assigns pulses from the converter to appropriate channels, which are assigned to specific time segments. The number of counts in individual channels corresponds to the number of registered annihilation processes that took place at a given moment.

The experimentally obtained spectrum of positron lifetimes is a finite sum of Poisson distributions, which are determined by the average lifetimes τ_i in different states. A certain amount of positrons will annihilate in the source and the Kapton foil, in which the ^{22}Na source is enveloped, and this should also be taken into account when analyzing the spectrum. A number of counts in individual channels N(t) is the convolution of the obtained spectrum with the time resolution $g(t)$ of the spectrometer used and can be denoted as:

$$N(t) = \int_{-\infty}^{+\infty} dt' g(t - t' - \Delta t_0) \sum_{i=1}^{n} \exp\left(\frac{I_i}{\tau_i}\right), \tag{4.32}$$

where, I_i is the intensity of the individual components of the average lifetime τ_i in these states, while Δt_0 is a slight shift in the timeline of the lifetime spectrum. The resolution function $g(t)$ can be described using the Gaussian distribution. The time resolution of the spectrometer can be defined as the Full Width at Half Maximum (FWHM):

$$FWHM = 2\sqrt{2ln2\sigma} = 2.355\sigma, \tag{4.33}$$

where σ is the standard deviation of the Gaussian distribution g(t).

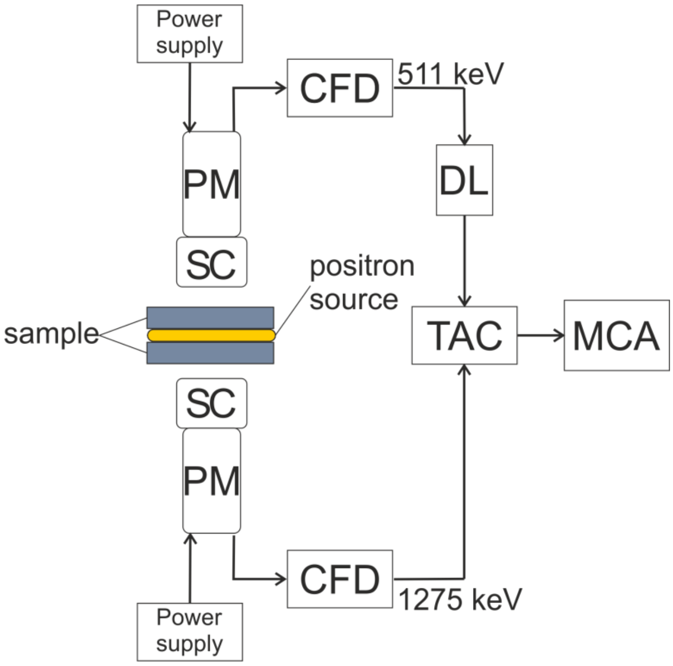

Figure 4.5 Scheme of a positron lifetime spectrometer.

The measured spectrum contains a certain amount of the positron lifetime originating from the source, approx. 15-20%, as well as in the sample and the background. After subtracting the background, a spectrum correction is performed due to a different percentage of annihilation in the source and the sample material itself. These depend on the construction of the source, i.e., its type and thickness of the foil in which the source is enveloped. A good method of determining the intensity of the positron lifetime components at the source is to measure the spectrum for a well-annealed sample with a known positron lifetime. Fig. 4.6 shows examples of positron lifetime spectra in a logarithmic scale as a function of time. There is a visible difference in the shape of the experimental spectra.

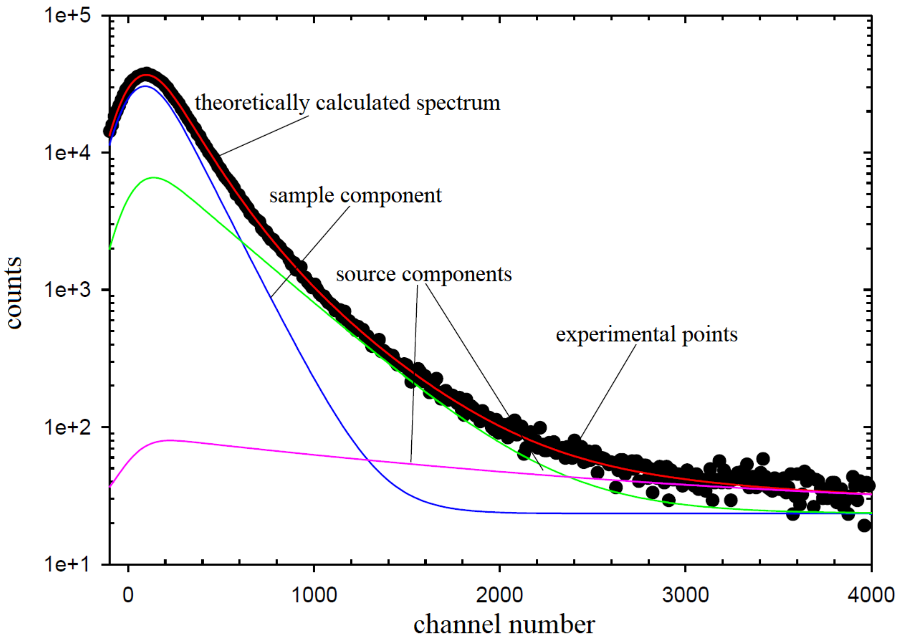

Figure 4.6 Positron lifetime spectrum in a logarithmic scale in a function of time, the channel number corresponds to the time.

4.4.2 Doppler broadening spectroscopy

In the DB spectroscopy, the source is aligned with the sample in the same way as in the lifetime measurements, and it is placed in front of the spectrometer used for registration of the 511 keV line. A schematic illustration of the spectrometer setup is shown in Fig. 4.7 Due to the relatively low energy-shift, high-resolution detector, which is the High-purity Germanium (HpGe) detector, is necessary. Its basic element, the Ge crystal requires cooling with liquid nitrogen. As a result of gamma radiation absorption in a pure Ge crystal, electron-hole pairs are created. A high voltage applied to the crystal causes that the products of the absorption process move to the electrodes located on the crystal surface. The amplitudes of the pulses generated on the electrodes are proportional to the energy of the registered quanta. Then the electrical impulses from the electrodes go to the amplifier (AMP) where their amplitude is increased. Ultimately, the signal goes to the MCA, which is an analog-to-digital signal converter.

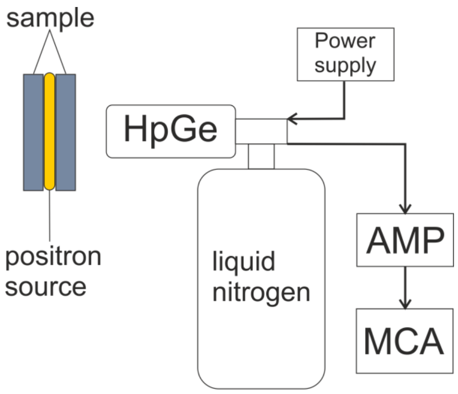

Figure 4.7 Schematic illustration of the detector setup used for DB spectroscopy.

As it was mentioned in Chapter 4.2.5, electrons in the matter have a certain distribution of momentum. It means that in the laboratory frame of reference, some shift of the energy of the registered quanta around the energy of 511 keV is observed. This phenomenon is called the DB of the annihilation line. The thermalized positron contributes to a negligible extent to the momentum of a positron-electron pair hence, the Doppler shift can be attributed only to the electron momentum. The measured annihilation line is a convolution of the distribution of electron momentum with the energy resolution of the spectrometer used. The registered annihilation quanta convey the information on the local electron momentum distribution, which changes in a specific way. These changes are reflected in the shape of the annihilation peak, which can be characterized by the so-called S- and W-parameters, as shown in Fig 4.8 [32]. The shape parameters considerably facilitate the analysis of the obtained spectrum. The S-parameter demonstrates the contribution of positrons annihilating with low momentum electrons that are present mostly in open volume defects. The W-parameter represents the contribution from annihilation with core electrons, which have higher momenta.

The S-parameter is defined as the ratio of the number of counts A_s in the middle of the annihilation peak to the number of all counts A under the entire line. Summation limits are selected arbitrarily and should remain the same during one measurement series. The limits are chosen symmetrically around the energy 511 keV so that the value of the S-parameter defined as:

$$S = \frac{A_S}{A}, \tag{4.34}$$

is approximately 0.5 for a defect-free sample. The value of the S parameter is positively correlated with the number of defects that are present in the sample. For example, as a result of the increased number of trapping events of positrons in vacancies, the number of counts in the central part of the annihilation line arises. More quanta with energies near 511 keV are registered due to their lower Doppler shift, and a narrowing of the registered annihilation line is observed.

The W-parameter is defined as the ratio of the sum of the number of counts from the areas $A_{\mathrm{w}1}$ and $A_{\mathrm{w}2}$ to the total number of counts under the peak A, as shown in Fig. 4.8:

$$W = \frac{A_{w1}+A_{w2}}{A}. \tag{4.35}$$

Usually, the areas $A_{\mathrm{w}1}$ and $A_{\mathrm{w}2}$ are chosen in such a way that the W-parameter value for a defect-free, reference sample is about 0.1.

If there is a high background for energies lower than 511 keV due to the Compton effect the $\mathrm{W_r}$-parameter is used instead of the W-parameter. The $\mathrm{W_r}$ parameter is defined as follows:

$$W_r = \frac{A_{w2}}{A}. \tag{4.36}$$

It is worth mentioning that there is no simple way to directly compare the S- and W- parameters obtained from measurements made with two different detectors, due to the different energy resolution of those detectors.

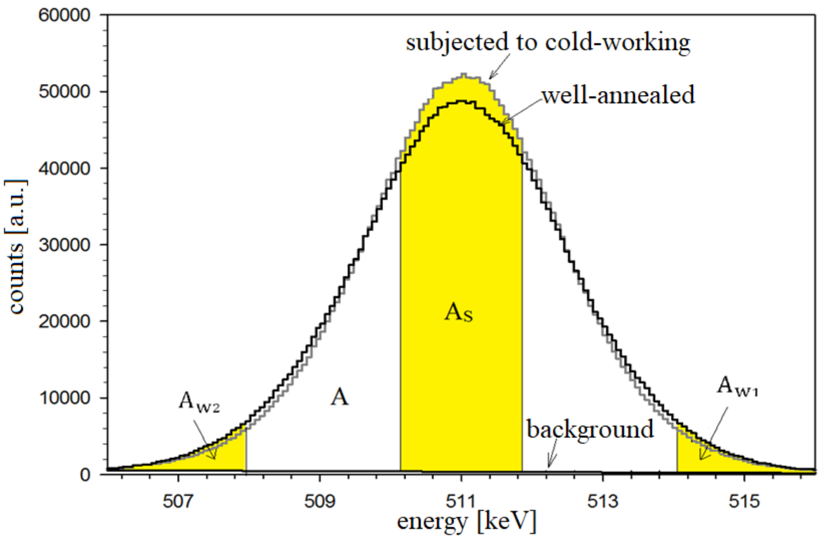

Figure 4.8 DB of the annihilation line. The marked areas denote the intervals used to calculate the S- and W-parameter.

4.4.3 Variable energy positron beam

To study surfaces, thin layers or film, and gradient structures, a VEP beam can be used. With the help of the device, it is possible to implant monoenergetic positrons with energy between a few dozen eV to a few dozens of keV into the material studied. The ability to control the energy of the implanted positrons makes it possible to precise implant them at a given depth up to several micrometers.

Positron emitted from helium-cooled ^{22}Na are moderated to a few eV on the frozen Ne. Fast and slow positrons that exit the moderator are separated and guided by the combination of the magnetic fields to a sample chamber. Only low-energy positrons are reaching the chamber with samples holder kept under electric potential that can be changed in the range between 0 and 35 kV. In this way, positrons can be accelerated to the desired energies. Then, the annihilation line is registered by HpGe detector. The scheme of the positron injector at the VEP facility at Joint Institute for Nuclear Research in Dubna is presented in Fig. 4.9.

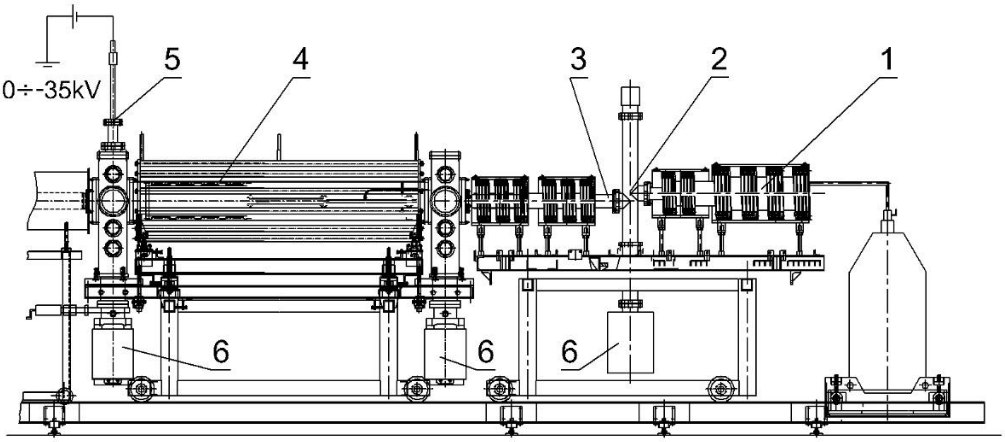

Figure 4.9 The scheme of positron injector at the VEP facility: 1-^{22}Na positron source; 2-diaphragm; 3-transfer channel; 4-Surko trap; 5-target insertion; 6-vacuum pumps [33].

References

1. S. Berko, Momentum Density and Fermi-Surface Measurements by Positron Annihilation, in Positron Solid-State Physics, (eds.) W. Brandt and A Dupasquier, North-Holland Publishing Company, Amsterdam, New York, Oxford 1983.
2. S. DeBenedetti, C.E. Cowan, W.R. Konneker, Phys.Rev. 76 (1949) 440.
3. J.W.M. Du Mond, D.A. Lind, B.B. Watson, Phys. Rev. 75 (1949) 1226.
4. M.N. Maisey, Positron Emission Tomography, Clinical Medicine, in D. L. Bailey, D. W. Towsend, P. E. Valk, M. N. Maisey (eds.) Positron Emission Tomography, Springer Verlag, London, 2003, 1.
5. P.A.M. Dirac, Proc. Roy. Soc 117 (1928) 610.

6. P.A.M. Dirac, Proc. Roy. Soc. 126 (1930) 360.
7. C.D. Anderson, Science 76 (1932) 238.
8. C.D. Anderson. Phys. Rev. 43 (1933) 491.
9. G.L Morgan, K.R Alrick, A Saunders, et al. Nucl. Instrum. Meth. B 211 (2003) 297.
10. H. Ravn, W.H. Schulte, C. Rolfs, et al. Nucl. Instrum. Meth. B 58 (1991) 174.
11. O.R. Frisch, Nature 136 (1935) 220.
12. I.K. MacKenzie, Experimental Methods of Annihilation Time and Energy Spectroscopy, in W. Brandt, A. Dupasquier (eds.): Positron Solid-State Physics, Proceedings of the international school of physics "Enrico Fermi" North-Holland, Amsterdam, New York, Oxford, 1983.
13. J.H. Hubbell, Radiat. Phys. Chem. 75 (2006) 614.
14. R.M. Nieminen, J. Oliva, Phys. Rev. B 22 (1980) 2226
15. T.J. Goronwy, Phys. Educ. 34 (1999) 276.
16. J. Dryzek, D. Singleton, Nucl. Instrum. Methods Phys. Res. B 252 (2006) 197.
17. J. Dryzek, Implantation to the solid https://ifj.edu.pl/private/jdryzek/pag_r131.html (accesed on 16.06.2021)
18. J. Dryzek, Acta Phys. Pol. A 107 (2005) 598.
19. A.F. Makhov, Sov.Phys. Solid State. 2 (1961)
20. S. Valkealahti, R. Nieminen, Appl. Phys A 32 (1983) 95
21. S. Valkealahti, R. Nieminen, Appl. Phys A 35 (1984) 51
22. J. Dryzek, P. Horodek, Nucl. Instrum. Methods Phys. Res. B, 266 (2008) 4000.
23. A. van Veen, H. Schut, J. de Vries, et al. AIP Conference Proceedings 218 (1991) 171.
24. F.A. Selim, D.P. Wells, J.F. Harmon, et al. J. Appl. Phys. 97 (2005) 11539.
25. R.N. West, Adv. Phys. 22 (1973) 263
26. R. Krause-Rehberg, H.S. Leipner, Positron Annihilation in Semiconductors, Solid-state sciences, Springer-Verlag, Berlin, 1999.
27. M.J. Puska, C. Corbel, R. M. Nieminen, Phys. Rev. B 41 (1990) 9980.
28. W. Brandt, in A.T. Steward, O. Roellig (eds.): Positron Annihilation, Academic Press, New York, 1967, 155.
29. W. Brandt, Appl. Phys. 5 (1974) 1.
30. M.J. Puska, M. Manninen, J. Phys. F: Met. Phys. 17 (1987) 2235.
31. A. Seeger, Appl. Phys. 4 (1974) 183.
32. M.J. Puska, R.M. Nieminen, Reviews of Modern Physics 66 (1994) 841.
33. P. Horodek, A.G. Kobets, I.N. Meshkov, A.A. Sidorin, O.S. Orlov, Nukleonika 60 (2015) 725.

Chapter 5: Basic corrosion science

The topic of the dissertation concerns metals for biomedical applications hence all discussed corrosion problems are related to metals. Corrosion is a relatively extensive and complex issue, therefore simply defining it is not an easy task. The process can be defined by the following broad definition. Corrosion is an irreversible interfacial reaction of a material with the surrounding environment resulting in deterioration of the material properties and its surface properties, and its dissolution to the environment [1]. Nevertheless, the aforementioned definition does not cover all aspects, e.g., it does not mention the formation of oxides on the surfaces of metals in some environments.

As it was mentioned in Chapter 1, corrosion of biometals accelerates their wear and ultimately leads to the loss of their integrity and surface properties. In the case of metallic implants, the products of corrosion alter their surrounding environment causing, e.g., change in pH, gas release, change in chemical components, i.e., the release of ions which may cause allergies or carcinogenesis. Hence, controlling the corrosion rate in the case of biomedical applications is even more important than in the case of other structural elements, e.g., buildings, pipes, bridges, etc. Corrosion aspects and the methods of protection against it are a major concern for mankind, generating tremendous economic costs to society [2].

Metallic corrosion processes are mostly electrochemical, hence it is important to understand basic electrochemistry, as well as basic information about the solid-state structure. The following Chapter introduces basic terminology to be used in the discussion and gives an overview of the basic electrochemical concepts which relate to the issue of corrosion of metals.

5.1 Principles of metallic corrosion in an aqueous environment

The corrosion of metals in an aqueous environment can be defined as the destructive electrochemical reaction of metal with water, oxygen, and ions that are present in the solution [3]. The driving force behind the corrosion process of metals is that the metallic form is not the most stable form for metal atoms. The corrosion of metals in aqueous solutions is inevitable because metal elements are more thermodynamically stable in the oxide state than in the metal state, while the only exceptions are noble metal elements. This is done by lowering the chemical potential of atoms through their dissolution from crystalline structure to the environment as ions until the potentials of both states are equal.

When homogeneous metal is immersed in an electrolyte the general corrosion takes place. General corrosion can be defined as the uniform dissolution of the metal surface, while localized attacks occur on some specific sites of a passive surface where a high local dissolution rate occurs [3]. The anodic reaction takes place on the metal surface. Metal atoms M are oxidized and dissolved into the solution in form of positively charged ions while leaving the electrons on the metal surface:

$$M \rightarrow M^{n+} + ne^{-}. \tag{5.1}$$

Opposite to the anodic reaction, the cathodic reaction takes place during which the reduction reaction of hydrogen ions, water, or dissolved oxygen with electrons released during anodic reaction occurs:

$$2H^{+} + 2e^{-} \rightarrow H_2, \tag{5.2}$$

It should be mentioned that the type of cathodic reaction depends on the electrolyte's pH and the standard potential of the corroding metal. Generally, in an acid or a neutral environment, the cathodic reaction consists in the reduction of H^+ and dissolved O_2, while in the neutral environment the reduction of water takes place:

$$O_2 + 2H_2O + 4e^{-} \rightarrow 4OH^{-}, \tag{5.3}$$

$$2H_2O + 2e^{-} \rightarrow 2OH^{-} + H_2. \tag{5.4}$$

The redox reaction of metal immersed in the solution of its salt is a single electrode reaction:

$$M \leftrightarrow M^{n+} + ne^{-}. \tag{5.5}$$

When the metal ions move into the electrolyte, the negatively charged surface makes them stay close to the surface which results in the creation of an electrical double layer [3].

5.2 Kinetics of corrosion

It is generally accepted that electrochemical processes are responsible for the corrosion of metals. The rate of dissolution reaction of metal can be described by the Nernst equation, which gives the electrode potential E of redox reactions:

$$E = E^0 - \frac{RT}{nF} ln\left(\frac{M^{n+}}{M}\right), \tag{5.6}$$

where R is the gas constant, T is the absolute temperature, E^0 is the standard electrode potential, n is the number of charges exchanged in the half-cell reaction, F is the Faraday constant, and M and M^{n+}, are activities or concentrations of metal and ions species, respectively. To estimate the corrosion behavior of metals in an aqueous environment, the Pourbaix diagram or Potential-pH diagram is used. It is based on the Nernst equation and it is a graphical representation of the equilibrium potential of the electrochemical reaction in the function of pH. More details and information on this issue can be found, e.g., in the original work of Pourbaix et al. [5].

The overall corrosion rate is controlled either by the anodic and cathodic process. When metal is at the equilibrium potential, the rates of anodic and cathodic reactions are equal. However when the potential of the metal is shifted by some small overpotential η from the equilibrium potential, the rate of anodic or cathodic reaction increases, as well as, corresponding current density value. The overpotential is equal to $\eta = E - E^0$, where E^0 is the equilibrium potential and E is the actual potential of the electrode. The value of the apparent current density at potential shifted by η is given by the Butler-Volmer equation [6]:

$$I = I_0 \left\{ \exp\left(\beta \frac{nF}{RT} \eta\right) - \exp\left(-(1-\beta) \frac{nF}{RT} \eta\right) \right\}, \tag{5.7}$$

where β is a symmetry coefficient (usually close to 0.5), I_0 is the exchange current density at the equilibrium potential and n is the number of charges that are exchanged during the reaction. At overpotentials, the anodic and cathodic reactions oppose each other. At any given potential the sum I of anodic I_a and cathodic I_c current densities are equal to $I = I_a + I_c = 0$ and at the equilibrium potential $I_0 = I_a = -I_c$. The value of the exchange current is proportional to the corrosion rate hence, the Butler-Volmer equation is used to estimate the corrosion rate of metals during electrochemical corrosion tests.

When the potential differs significantly from equilibrium, one reaction becomes dominant while the rate of the other one becomes negligible. Based on eq. 5.7, the anodic I_a and cathodic I_c current densities are equal to:

$$I_a = I_0 \left\{ \exp\left(\alpha_a \frac{nF}{RT} \eta\right) \right\}, \tag{5.8}$$

$$I_c = I_0 \left\{ \exp\left(\alpha_c \frac{nF}{RT} \eta\right) \right\}, \tag{5.9}$$

where α_a and α_c are the anodic and cathodic charge transfer coefficients respectively. For simple electrode reactions without the participation of adsorbed intermediates:

$$\alpha_a \alpha_c = n, \tag{5.10}$$

where n is the number of charges that are exchanged during the reaction. The so-called anodic b_a and cathodic b_c Tafel coefficients are given by:

$$b_a = \frac{dE}{d\log_{10}|I_a|} = \frac{2.303RT}{\alpha_a F}, \tag{5.11}$$

$$b_c = \frac{dE}{d\log_{10}|I_c|} = -\frac{2.303RT}{\alpha_c F}. \tag{5.12}$$

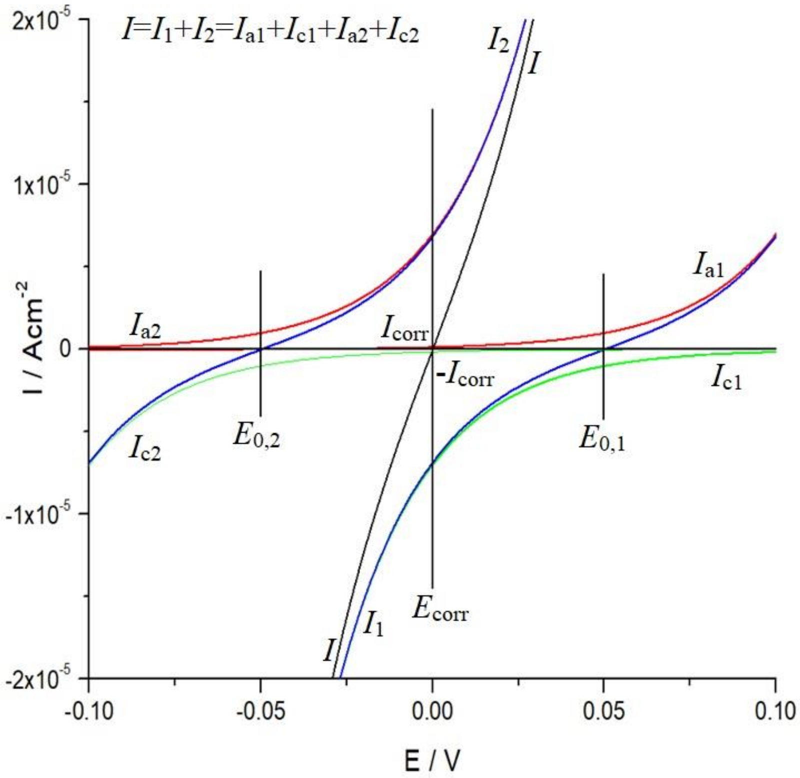

Figure 5.1 Dependence of the current density on the potential simulated for a corroding electrode. Index a - anode reaction, index c - cathode reaction, $E_{01,}$ and E_{02} are the equilibrium potentials for reactions 1 and 2 respectively.

On any given potential two reactions occur at the same time, hence $I=I_{a1}+I_{c1}+I_{a2}+I_{c2}$, where ‘1’ and ‘2’ denote the partial cathodic and anodic reactions of the corrosion process, respectively, as seen in Fig. 5.1 The density of the anodic current is balanced by the cathodic one at corrosion potential E_{corr}, which lies between the equilibrium potential for anodic and cathodic processes. The Stern-Geary approximation of corrosion current I_{corr} may be used, if the equilibrium potential of the cathodic and anodic reactions are shifted enough from the E_{corr} and the exchange current densities of both processes have got similar value [6]:

$$I_{corr} = \frac{b_a|b_c|}{2.303R_p(b_a+|b_c|)}, \tag{5.13}$$

where, R_p is the polarization resistance, which is defined as:

$$R_p = \left(\frac{\Delta E}{\Delta i}\right)_{\Delta E \to 0}. \tag{5.14}$$

5.3 Corrosion rate evaluation methods

As it was mentioned earlier, the corrosion process is mainly an electrochemical phenomenon hence to evaluate its rate the electrochemical techniques are commonly used. Electrochemical test methods, such as the open circuit potential (OCP) test, electrochemical impedance spectroscopy (EIS), and linear sweep voltammetry (LSV) are commonly used to evaluate the corrosion behavior of magnesium and titanium. Parameters obtained during electrochemical tests, e.g., corrosion current density enable evaluate the corrosion behavior of metals.

Fig. 5.2 shows an illustration of electrochemical cells used in electrochemical corrosion tests. The test system is equipped with three electrodes: a tested sample - a working electrode (WE), a reference electrode (RE), and a counter electrode (CE). A saturated calomel electrode (SCE), or silver-silver chloride (Ag-AgC) electrodes are usually used for Re. Platinum or carbon electrodes are commonly used for the CE. The potential of the WE is measured against RE, while the current flowing between the WE and CE is measured by a potentiostat.

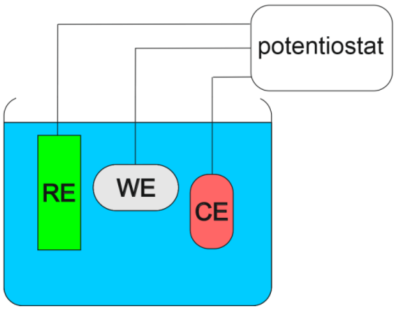

Figure 5.2 Electrochemical cell used in electrochemical corrosion tests.

5.3.1 Open circuit potential test

Registration of an electrochemical potential is one of the simplest measurements in electrochemistry. The potential of metal immersed in an aqueous solution depends on the reactivity of the metal and the oxidation capacity of the solution. It is necessary to make the potential measurements for a stable reference electrode so that any changes in the measured potential can be attributed to changes at the specimen/solution interface.

During the OCP measurement, the sample is immersed in the corrosive solution and the potential is registered against the stable RE in the function of time. The potential of the sample is measured without any intentional interference in electrochemical reactions that occur on the sample's surface. Due to this, every change in the value of registered potential is strictly related to changes in the tested material potential. The value of this potential varies during the measurements due to changes occurring on the sample's surface, e.g., oxidation and formation of a passive layer. After some period of immersion, the value of the potential stabilizes. OCP measurements reveal a tendency of a material to oxidation in a solution. It is generally assumed that the more positive registered potential, the more 'noble' and corrosion-resistant the tested metal is.

5.3.2 Linear sweep voltammetry

LSV technique allows creating a graphical representation - Stern or Evans diagrams, of the registered current density in the function of applied potential. The method consists of polarizing the tested sample with a potential changing linearly, with a constant rate in time, while recording the current flowing through the circuit. LSV enables studies of metal electrode behavior at both anodic – more positive than E_{corr} and cathodic potentials - with potential lower than E_{corr}.

The values of Tafel coefficients can be obtained by plotting the Evans diagram which is a graphical representation of overpotential η in the function of log(I). Their value equals the slope of the rectilinear sections of the plot obtained in the Evans diagram as shown in Fig 5.3. It has to be noted that polarization curves do not have to be symmetrical, and their shapes are determined by the Tafel coefficient and the exchange current. Tafel slope extrapolation method enables obtaining E_{corr} and I_{corr}. The current density I increases with an increase in overpotential following the equation derived from Butler-Volmer equation 5.7:

$$\eta = a + b\log(I), \tag{5.15}$$

where a and b are constants. Both Tafel coefficients: cathodic $b_c = \frac{RT}{\alpha_c F}$ and anodic $b_a = \frac{RT}{\alpha_a F}$ are equal to the tangent of the angle of inclination of branches extrapolation as shown in Fig. 5.3.

The polarization resistance R_{p} corresponds to corrosion resistance and can be obtained by a linear polarization resistance method. In a narrow region around E_{corr} ± 10 mV, as shown in Fig. 5.4 current depends linearly on the potential according to the Stern-Geary formula:

$$I_{corr} = \frac{b_a b_c}{2.303 R_p (b_a + b_c)} \left(\frac{\eta}{I}\right)^{-1} = \frac{K}{R_p}, \tag{5.16}$$

where b_a and b_c are Tafel coefficients, K is the so-called conversion factor, and η/I is the slope of the polarization curve near the E_{corr}, which corresponds to the polarization resistance.

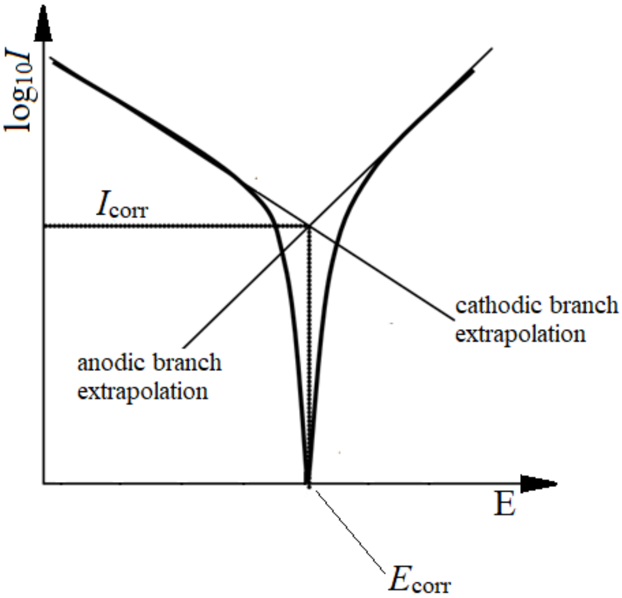

Figure 5.3 Schematic illustration of the Tafel extrapolation method.

Value of Rp and both b_a and b_c coefficients can be determined experimentally, although this is not always possible in the case of b coefficients. In the case of comparative measurements, it is usually sufficient to determine R_p only, as it is inversely proportional to the corrosion current.

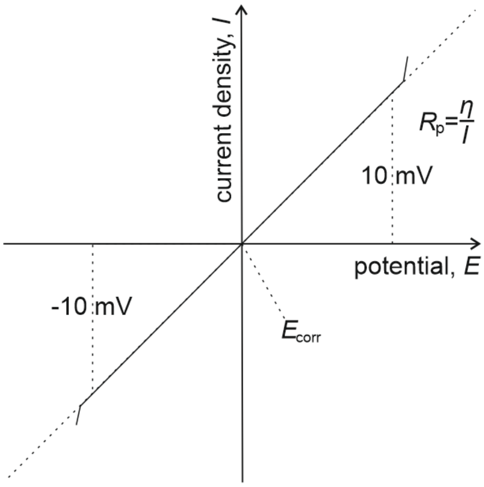

Figure 5.4 Scheme of linear polarization test, R_p - polarization resistance, E_{corr} - corrosion potential, η - overpotential, and i - current density.

5.3.3 Electrochemical impedance spectroscopy

During EIS measurements the sample (WE) is stimulated by an alternating current signal with a small amplitude, i.e., usually 10 mV, and known frequency. Measurements are performed in a wide range of frequencies (usually from 10^5 to 10^{-2} Hz), at which the current response of the measuring system is registered. The time required to measure the intensity for a given frequency is equal to one period of the AC signal, i.e., time measurement for 1 Hz – 1 s, and 1 mHz - 1000 s. Values of the system's impedance can be calculated by relating the value of the signal to the current response. Impedance data is usually presented in form of Bode plots, which illustrate the logarithm of the modulus of the impedance ($\log(|Z|)$) and phase angle ($-\Theta$) in the function of the logarithm of frequency *f*. The type of the processes and their number are reflected in the shape of Bode plots.

Equivalent electric circuits (EEC) are commonly used in the analysis of EIS data. Impedance models are constructed according to the electrochemical phenomena. The EEC consists of resistance elements, R, and constant phase elements (CPE), which include capacitance C and inductance elements L. CPEs are non-intuitive circuit elements, which are a representation of different physical phenomena. For example, capacitance elements may represent surface roughness, presence of impurities, and crystal lattice defects such as, e.g., dislocations and grain boundaries, while inductance may be related to the phenomena of adsorbing species on the electrode surface. The impedance of the constant phase Z_{CPE} element can be calculated from:

$$Z_{CPE} = q^{-1}(i\omega)^{-n}, \tag{5.17}$$

where q is a factor of proportionality, n is the CPE exponent that characterizes the phase shift, and ω is the angular frequency of the signal. For integral values of n ($n = 1, 0, -1$), the CPE represents C, R, and L, respectively. For $n = 0.5$, it gives the Warburg impedance, which represents the resistance related to diffusion in an electrochemical process [7].

References

1. B. Cwalina, Biodeterioration of concrete, brick and other mineral-based building materials, in T. Liengen, D. Féron, R. Basséguy, I.B. Beech (eds.): Understanding Biocorrosion, Woodhead Publishing, 2014, 281.
2. M.I. Hussain, S. Nawaz, M.M Sajid, et al. Corrosion resistance of nanostructured metals and alloys, in S. Rajendran, T. ANH Nguyen, S. Kakooei, M. Yeganeh, Y. Li (eds.): Corrosion Protection at the Nanoscale, Elsevier, 2020, 63.
3. R.W. Revie, H.H. Uhlig, Corrosion and Corrosion Control, An Introduction to Corrosion Science and Engineering, fourth ed., Wiley-Interscience, 2008.

4. L. Veleva, Soils and Corrosion, in R. Baboian (ed.): Corrosion Tests and Standards: Application and Interpretation, 2nd Edition, ASTM International, OH, 2005, 387.
5. M. Pourbaix, Atlas of Electrochemical Equilibria in Aqueous Solutions. Pergamon Press, UK, London, 1966.
6. R. Guidelli, R.G. Compton, J.M. Feliu, et al. Pure Appl. Chem. 86 (2014) 259.
7. A.J. Bard, L.R. Faulkner, Electrochemical methods: fundamentals and applications, Wiley, New York, 1980.

Chapter 6: Subsurface layer in metals studied by positron annihilation spectroscopy – the methodology of the experiment with chemical removing of sample layers

The following Chapter shows the usefulness of PAS for tracing the microstructural changes introduced in the subsurface layer of metals during various mechanical treatments. The methodology of obtaining depth profiles of the annihilation parameters by sequential chemical etching of layers of the tested material is presented. The studies concern copper subjected to sandblasting with different parameters of this process, deformed by compression and cut by lathe machining. One can expect that different ways of sample deformation induce different distributions of crystal lattice defects and hence different depth profiles of positron annihilation parameters, in this case, the S-parameter. The choice of copper as sample material was dictated by its simple face centered cubic (fcc) structure and the well-known tendency to strengthening by cold-working connected to the creation of crystal lattice defects.

6.1 Sample preparation

Six samples in the form of disks of 8 mm in diameter and 5 mm thick were cut from the refined copper rod with the purity of 99.9% and polished with abrasive papers of various gradations. In the next step, all samples were annealed in a vacuum of 10^{-5} Torr at 600 °C for one hour and then slowly cooled with the furnace to room temperature. In this way, specimens with only residual defects were obtained. One of the samples was kept as a reference, while the rest were exposed to mechanical treatments.

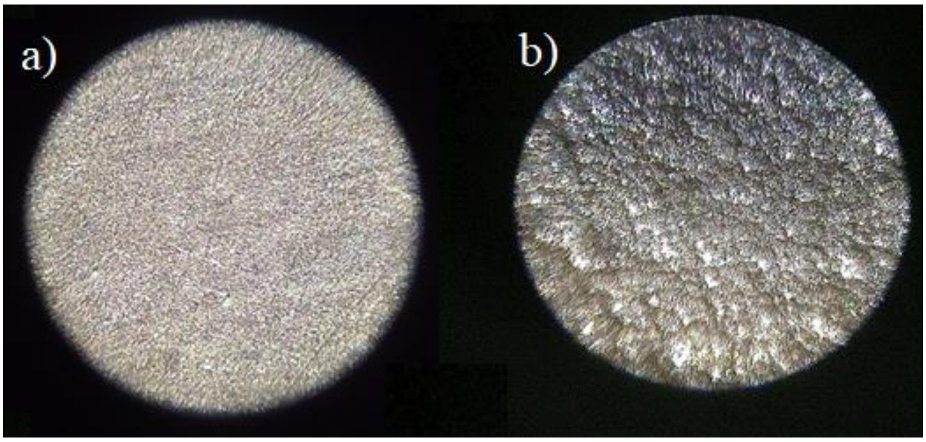

Figure 6.1 Optical microscope image of the reference sample (a) and the one sandblasted under 5 bar for 1 minute (b); magnification is equal to 180. A change in surface topology can be observed due to increased roughness caused by sandblasting.

Three disks of Cu were sandblasted. Sandblasting is the SP method, consisting of propelling abrasive media on the workpiece surface. The method is commonly used to expel rust, remove paint, and preparing surfaces for further treatments. Sandblasting is one of the oldest methods used for improving the osseointegration of metallic implants [1,2]. The high-speed shots cause plastic deformation close to the surface of the material treated. In this case, glass spheres of diameter 125 μm were blasted on the sample surface with a 90° impact angle and with a distance of 1 cm between a nozzle and the sample. Surfaces of two samples were blasted for 1 minute under different pressure of 1 or 5 bar, while the third specimen was blasted under 5 bar for 3 minutes. Renfert Vario Basic Jet blaster was used. Fig. 6.1 Cu specimens before and after sandblasting under 5 bar for 1 minute.

The fourth sample was only cut off from the rod using a lathe tool with a rotation speed of 1000 rev/min without cooling. The last of the copper specimens were pressed using a uniaxial hydraulic press with a pressure of 15 MPa and its thickness reduction was 72%.

6.2 Positron annihilation spectroscopy measurements details

An encapsulated isotope ^{22}Na with the activity of c.a. 15 μCi, sealed in a small capsule made of copper served as a positron source. Positrons were emitted through a 5 μm thick titanium window placed on the top of the capsule. The sample was placed on top of the capsule and placed in front of the HpGe detector. The studied sample covered the whole area of the titanium window. The annihilation photons originating from annihilation events in the sample are detected in the HpGe detector, while the lead shield located between the detector and the source absorbed most of the annihilation photons coming from the annihilation events in the capsule [3]. In this way, most of the registered annihilation quanta are attributed to annihilation events in the specimen. Any registered changes in annihilation parameters, i.e., S-parameter, during the measurement series were attributed to changes in the microstructures of the samples. It is worth noticing that the described above sample and source configuration is not typical for the PAS measurements depicted for example in Fig. 4.6, where the source is sandwiched between two identical samples which ensures that positrons emitted from the source in the full solid angle annihilate in the samples. However, the results presented further in this Chapter show that even when two identical samples cannot be obtained or when measurements are performed in situ, this experiment geometry still enables obtaining valuable data.

The DB of the annihilation line was registered at room temperature, by HPGe detector with energy resolution, FWHM = 1.20 keV at 511 keV. The measured spectra were analyzed using the SP-16K program [4]. This program allows to determining the S- and W- Parameters by fitting Gaussian function to the measured points with the automatic subtraction of the background. The energy range used for the calculations was constant within the entire measurement series.

6.2.1 The methodology of obtaining depth profiles of the annihilation parameters

Positrons emitted from the radioactive ^{22}Na isotope have a continuous energy spectrum; thus, they probe a certain depth inside the target material. The main contribution to the measured values of the annihilation parameters comes from a layer with a thickness comparable to $1/\alpha_+$. The linear absorption coefficient α_+ for positrons emitted from the ^{22}Na source implanted in Mg, Ti, Fe, and Cu are gathered in Table 4.1 in Chapter 4.2.2.

The penetration range of positrons from the ^{22}Na source is much larger than the range of additional defects that may be introduced during etching. Hence, It can be assumed that the chemical removal of the sample layers does not affect PAS measurements [5,6].

In the case of pure copper, the estimated average implantation depth is equal to 23 µm. The estimated implantation range is several times smaller than the layer affected by, e.g., sandblasting. Thus, if the deformed zone extends up to a few hundreds of micrometers, it is possible to obtain depth profiles of the positron lifetime and S- and W-parameters by sequential removal of layers of the sample. It was confirmed by Dryzek who performed the reconstruction of the actual positron lifetime profiles for irradiated silicon. In that case, the range of the defect distribution was comparable to the positron range, and the actual and measured values aligned pretty well [7].

To obtain the depth profiles of positron annihilation characteristics, thin layers of about 20 µm thick were removed from the Cu samples by sequential etching. All of the specimens were etched in the nitric acid solution. After each step, the thickness of the removed layer was measured using a digital micrometer caliper with ±1 µm accuracy and PAS measurements were carried out.

6.2.2 Results and discussion of positron annihilation spectroscopy measurements of deformed Cu

Fig. 6.2 shows the results of DB measurements for the reference sample and the sandblasted specimens. The values of the S-parameter are presented as a function of the depth. The hatched region represents values obtained for the reference sample.

As it can be seen, etching does not introduce additional defects, and the values of the S-parameter obtained for the bulk sample do not change during the measurement series. Close to the surface, the values of the S-parameter for the sandblasted specimens are higher than for the reference sample. This indicates the creation of the subsurface zone rich in crystal lattice defects during sandblasting. The obtained S-parameter dependencies are typical for this type of treatment and material. For all the sandblasted specimens, the S-parameter is decreasing to the values received for the bulk sample. The thickness of created deformed zones depends mainly on the time of sandblasting. For the sample that was sandblasted under the pressure of 5 bar for 3 min, the depth of the deformed zone is the largest and equal to ca. 240 µm. Blasting for 1 min under the pressure of 1 bar or 5 bar results in the creation of the deformed zones with similar extending to the depth of ca. 110 µm. This can be explained by the fact that despite a greater number of crystal lattice defects introduced during higher pressure of blasting, at the same time, the most deformed layer of the specimen is removed due to high erosion of the surface.

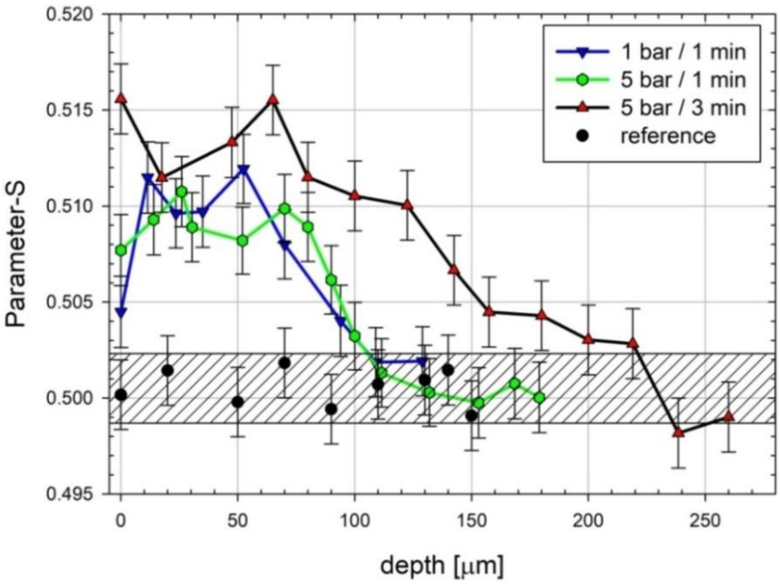

Figure 6.2 Values of the S-parameter as the function of the depth from the Cu surfaces exposed to sandblasting with 125 µm glass particles for different pressures and times. The hatched region represents the values obtained for the reference sample.

However, an unusual increase in the S-parameter near the surfaces of the specimens was observed. This is most visible for the sample that was sandblasted for 1 minute under 1 bar. The value of the S-parameter increases starting from the surface to a depth of ca. 50µm. Deeper, its values decrease almost linearly, indicating a decrease in the number of defects introduced during sandblasting. For the sample sandblasted under the pressure of 5 bar for 1 min, the maximum of the S-parameter is visible at the depth of about 30 µm. In the case of a sample blasted for 3 min, a decrease in the value of the S-parameter is visible to the depth of c.a. 20 µm, then the values of the parameter increases, reaching maximum at the depth of about 70 µm. This increase in the S-parameter values may be explained by the presence of the embedded abrasive media. A similar phenomenon has been observed by Horodek et al. in samples of pure copper that were blasted using aluminum oxide particles of the size of 250 µm [8]. Registered annihilation quanta may originate from both copper and the abrasive media which were shot into the specimen. The increase of the S-parameter values near the surface may be caused by the annihilation events in embedded glass particles. However, similar studies of beryllium bronze sandblasted using 110 µm particles of Al_2O_3 conducted by Kurdyumov et al. did not show abrasive particles deposition inside the samples [9].

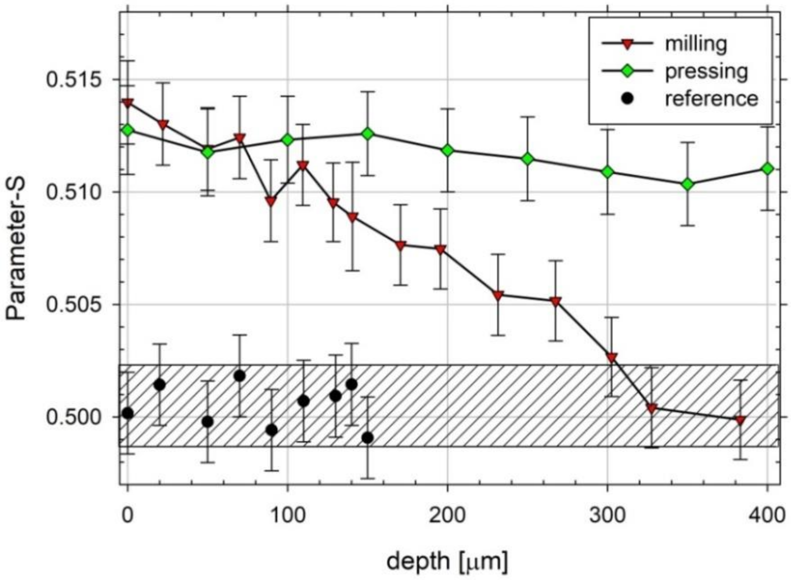

Figure 6.3 The dependence of the S-parameter in the function of the depth from the surface for the specimens subjected to cutting and 72% compression. The hatched region represents the values obtained for the reference sample.

Fig. 6.3 shows the values of the S-parameter as the function of depth for the Cu specimens pressed under 15 MPa and the second one cut by lathe machine. As it can be seen, the profile of the S-parameter for the pressed specimen differs from that obtained for cutting. For the pressed sample, values of the S-parameter are almost constant in the whole volume of the sample. It is because during uniaxial pressing, compressive stresses act on the whole volume of the sample, and the introduced microstructural changes, i.e., creation and movement of dislocations, are approximately the same across the entire volume of the specimen. It explains the constant value of the S-parameter during the measurement series. For the cut sample, the S-parameter decreases as the depth from the surface increases, finally reaching values for the bulk sample, at about 300 µm. During cutting, mainly shear stresses appear close to the treated surface, which induces dislocation movement and creation dislocations. The number of introduced crystal lattice defects decreases gradually with the depth from the treated surface. It is reflected in a decrease of the S-parameter values.

6.3 Summary

The performed experiment showed that the procedure of sequential etching combined with PAS measurements can be successfully used for obtaining depth profiles of annihilation characteristics, i.e., positron lifetimes, and S- or W- parameters. As far as the chemical etching introduces defects, they are created in a very thin surface layer which does not influence the S-parameter obtained in conventional PAS measurements using a radioactive β^+ source. Only a small amount of positron annihilates in this layer. It is confirmed by the results for the reference sample and the sample deformed by compression.

The measurement methodology used enabled obtaining the depth profiles of the S-parameter in deformed Cu specimens. The observed differences in the S-parameter profiles are caused by the different outcomes of the cold-working methods applied. For the sandblasted samples and the cut one, the well-defined subsurface zones are visible in the S-parameter dependencies on the depth. For the pressed sample the elevated, almost constant value of the S-parameter is registered in the whole measurement range. The difference is that in the case of the pressed sample, defects were introduced into the entire volume of the specimen, while in the case of sandblasted and cut samples they were introduced just below the treated surfaces. It should be noted, that for the sandblasting the size of the created subsurface zone depends mostly on the sandblasting time, while the differences between sandblasting pressure are negligible. It seems that the presence of the embedded particles of the blasting medium also influences the obtained S-parameter profile which exhibits a maximum of its value at some depth between 50 and 70 μm.

PAS allowed determining the thickness of the created deformed zones rich in crystal lattice defects. For the sample that was sandblasted under the pressure of 5 bar for 3 min, the depth of the deformed zone is the largest and equal to ca. 240 μm. Blasting for 1 min under the pressure of 1 bar or 5 bar results in the creation of the deformed layers similarly extending to the depth of ca. 110 μm. For the sample cut by lathe machining the range of the deformed zone exceeds 300 μm.

References

1. W. He, X. Yin, L. Xie, et al. J. Mater. Sci.: Mater. Med. 30 (2019) 73.
2. L.M. Czumbel, B. Kerémi, N. Gede, et al. PLoS ONE 14 (2019) e0216428.
3. P. Horodek, J. Dryzek, Acta Phys. Pol. B Proc. Suppl. 9 (2016) 231.
4. J. Dryzek SP-1 program https://ifj.edu.pl/private/jdryzek/page_r18.html, (accesed on 16.06.2021)
5. E. Dryzek, J. Mater. Sci. 38 (2003) 3755.
6. J. Dryzek, E. Dryzek, T. Suzuki, R. Yu, Tribol. Let. 20 (2005) 91.
7. J. Dryzek, Acta Phys. Pol. A 137 (2020) 196.
8. P. Horodek, K. Siemek, J. DryzekJ. M. Wróbel, Materials 10 (2017) 1343.
9. S. Kurdyumov, K. Siemek, P. Horodek, J. Phys.: Conf. Ser. 929 (2017) 012029.

Chapter 7: Studies of Mg specimens subjected to surface mechanical attrition treatment

The following Chapter presents the results of interdisciplinary studies of Mg samples subjected to SMAT, which was used to generate a gradient microstructure in them. PALS and VEP beam measurements, microhardness tests, EBSD, XRD, and electrochemical tests were used. The details of the apparatus used and methodology of measurements not included in the Chapters devoted to PAS and corrosion tests are presented.

7.1 Sample preparation

A specimen 100 mm × 100 mm × 7.6 mm in dimensions was cut from a plate of commercial-grade magnesium (99.5% purity). To obtain a material with only residual crystal lattice defects the specimen was annealed at 400 °C in a vacuum ($\sim 10^{-3}$ Pa) for half an hour and then slowly cooled inside the furnace to room temperature before the SMAT.

SMAT was performed in the stainless-steel chamber at room temperature in the air using 2 mm diameter stainless steel balls and a vibration frequency of 20 kHz. Fig. 7.1 shows the Mg sample in the SMAT chamber. To examine changes of the microstructure induced in the initial stage of SMAT, the two opposite sides of the magnesium were treated separately for 60 s and 120 s, with vibration amplitudes 13 ± 2 μm and 27 ± 2 μm, respectively. For simplicity, the opposite sides of specimens from now on are referred to as 60 s and 120 s. Fig. 7.2 shows both surfaces of the magnesium specimen subjected to SMAT.

Figure 7.1 Mg specimen after the SMAT.

After SMAT, the plate was cut into smaller pieces 10 mm × 10 mm in size. Pieces of the plate, not subjected to the SMAT process, were kept as a reference. Additional samples prepared from annealed magnesium were deformed at room temperature using a uniaxial hydraulic press.

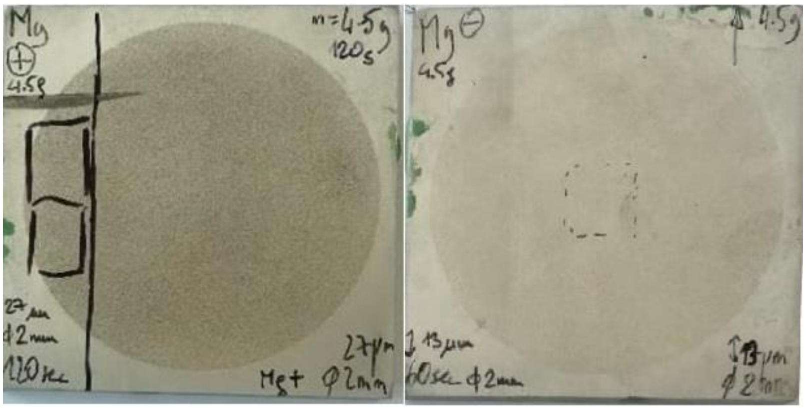

Figure 7.2 Surfaces of the magnesium specimen subjected to SMAT; on the left side 120 s, on the right side 60 s. Around the SMATed area, non-treated material can be seen.

7.2 Methods

7.2.1 Surface characterization

Surfaces of SMATed magnesium samples were characterized using an optical profiler WYKO NT9300. To evaluate the SMAT effect on the surface of the Mg specimens, the arithmetic average height parameter R_a was calculated. It is the most universally and commonly used roughness parameter in quality control. The parameter is easy to measure and it describes the height variations y on the examined surface. It is defined as the arithmetic mean of the absolute ordinate $y(x)$ within the sampling length l:

$$R_\mathrm{a} = \frac{1}{l}\int_0^l |y(x)|\,dx. \tag{7.1}$$

7.2.2 Optical microscopy and electron backscatter diffraction

To observe the microstructure, the samples were cross-sectioned, mounted in cold mounting resin, grounded with a series of SiC papers down to a grid 2400, and then further polished using aluminum oxides with grain size down to 0.05 μm and the 0.04 μm silica oxide, and, finally, argon ion beam cleaned using an IM4000Plus instrument.

To find the crystal orientation, as well as, microstructural maps of the tested material electron backscatter diffraction (EBSD) technique was used [1]. Nova NanoSEM 450 Scanning Electron Microscopy (SEM) was used.

An optical microscope Axio Imager M1m was used for observation of the microstructure of the cross-sectioned samples.

To reveal the possible presence of iron on the surfaces of the samples, the SEM-EDS (Energy Dispersive Spectroscopy) analysis using S-3500N microscope with the analyzer NORAN 986B-1SPS was performed before and after SMAT.

7.2.3 X-ray diffraction measurements

X-ray diffraction is a non-destructive method that enables the study of the crystallographic structure of crystalline materials. The shape of the obtained diffractograms is related to the crystal structure of an examined material. The analysis of the diffractograms allows obtaining information on lattice parameters such as distances between the crystallographic planes, which makes it possible to study strains and stresses in the tested sample.

The width of the registered diffraction peaks is correlated with the size of the areas of the tested material in which the coherent scattering of X-rays occurs. The size of such scattering centers can be linked with the size of crystallites that form the grains of the material however crystallites may be smaller. The width of diffraction peaks is also influenced by various distortions in the crystal structure. The basis of determining the size of crystallites using XRD is to define the apparatus broadening of the diffraction lines. To do this, a diffraction measurement should be performed for a sample with a known, large size of crystallites and the correct crystal structure. The measured width of the diffraction peaks for such a reference material should depend only on instrumental factors.

The Scherrer equation can be used to determine the size of the crystallites [2]:

$$l = \frac{K\lambda}{B\cos\theta}, \tag{7.2}$$

where *l* is the size of the coherent diffraction domains, which can be related to the notion of crystallite (i.e., crystal volumes relatively free from defects), *B* is the line broadening FWHM, after subtracting the instrumental line broadening, *K* is the so-called dimensionless Scherrer constant, and λ is the wavelength of the incident wave. The constant *K* ranges from 0.84 to 1.38. With the assumption that the material studied has only cubic crystals of equal dimensions $K = 0.94$ [3]. The crystallite is defined as a very low dislocation density volume bounded by an area with significantly increased dislocation density and much smaller than the grain, especially for the plastically deformed materials [4,5]. Crystallites are usually smaller than the dislocation cells or the subgrains observed by transmission electron microscopy.

The Scherrer equation does not take into account lattice strains. The line broadening resulting from lattice strains can be described in the following way:

$$B_z = 4\eta \tan\theta, \tag{7.3}$$

where η is linked to the root-mean-square lattice strain. In general, peak broadening is related to both the size of the crystallites and their deformation. These effects can be described using the well-known Williamson-Hall (W-H) method, which can be also used to determine average crystallite size [6]:

$$B\cos\theta = \frac{k\lambda}{l} + \eta\sin\theta, \tag{7.4}$$

where B is FWHM of the peak corrected for the instrumental broadening.

It is not possible to measure stresses directly using XRD methods. However, by series of diffraction measurements and the calculations based on them, it is possible to determine the deformation of the crystal lattice in the material studied. Knowing the material constants, it is possible to calculate the stresses causing the deformation of the crystal lattice. The well-known Bragg's law describes the relationship between the position of the diffraction peak (the angle between the incident ray and the scattering plane) and the distance between crystal lattice plains (lattice spacing d_{hkl}) in the crystal:

$$n\lambda = 2d_{\mathrm{hkl}} sin\theta, \tag{7.5}$$

where n is an integer, and λ is the wavelength of the incident wave. In the deformed material, the stress-induced change in d_{hkl} distance shifts the position of the diffraction peaks. Measurements of this shift make it possible to evaluate the deformation of the material by determining the distance between the planes. Deformation ε (perpendicular to the surface of the sample) can be determined by comparing the d_{hkl} distances in the deformed sample d_d with the distance measured for the reference, undeformed material d_0:

$$\varepsilon = \frac{d_d - d_0}{d_0}. \tag{7.6}$$

The measurements can be made at different angles ψ to the incident X-ray beam and different directions to the surface φ, as shown in Fig. 7.3:

$$\varepsilon = \frac{d_{\varphi\psi} - d_0}{d_0}. \tag{7.7}$$

The stress distribution is described by principal stresses σ_1 and σ_2 that exist in the plane of the surface, as shown in Fig. 7.3. No stress is assumed perpendicular to the surface, σ_3. Nevertheless, a strain component perpendicular to the surface ε_3 exists as a result of Poisson's ratio contractions caused by the two principal stresses.

The stresses σ in each direction can be calculated based on at least two measurements of the interplanar distances made for crystallographic planes that are parallel to the surface and containing the direction in which the stress is measured:

$$\sigma_\varphi = \frac{E}{(1+v)\sin^2\psi}\left(\frac{d_\psi - d_0}{d_0}\right), \tag{7.8}$$

where E is Young modulus and v is the Poisson's ratio of the material.

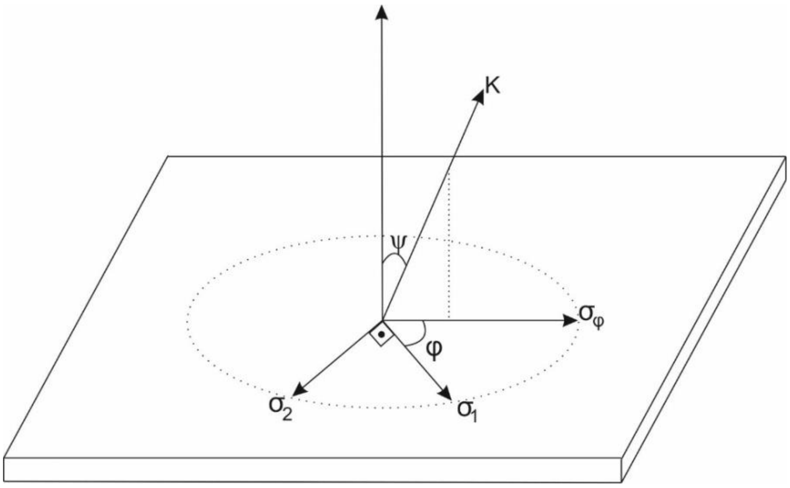

Figure 7.3 Orientation of the scattering vector K is defined by the φ and ψ angles.

The most common method of stress determination is the $\sin^2\psi$ method [7,8]. The method is based on the measurement of a single diffraction line. In the method, a series of diffraction measurements are performed for multiple ψ tilts, and the lattice spacing is calculated. A relationship between the *d*-spacing and $\sin^2\psi$ is plotted. The stress is calculated from the slope of the best fit. The stress is equal to the slope of the obtained linear relationship:

$$\sigma_\varphi = \frac{E}{(1+v)} m, \tag{7.9}$$

where m is the slope of the obtained line. There are two variants of the $d_{hkl}\sin^2\psi$ method consisting of inclining the sample to the incident beam of radiation in the diffraction plane (chi-stress) or the plane perpendicular to the diffraction plane(omega-stress).

To examine stresses in the near-surface region of the SMATed specimens the Multi-Reflection Grazing-Incidence X-ray Diffraction (MGIXD) method was used [9,10]. The method enables non-destructive stress measurements at depths of several micrometers for the metals. The MGIXD method is a useful tool for determining the in-depth stress gradients near the surface which are known to significantly influence the corrosion resistance of materials [11]. The stresses near the surface of the specimen can be measured using the standard X-ray $\sin^2\psi$ method. However, the penetration depth of X-ray radiation changes significantly during measurement, which is undesirable in an investigation of materials with a gradient structure. In the MGIXD method, the X-ray penetration depth is defined by the absorption of radiation coefficient of the material studied and does not change significantly during the experiment. In the method, the measurements are carried out for many hkl reflections using fixed both wavelength and incidence angle α of X-ray radiation. The used geometry of the experiment is characterized by a small and constant incident angle, in ω acquisition mode, and by different orientations of the scattering vector: $\psi_{hkl}=\theta_{hkl} - \alpha$, where $2\theta_{hkl}$ are the diffraction angles corresponding to reflections for which diffraction peaks are measured.

The incidence angle of the X-ray beam is constant during the measurement series, thus its penetration depth depends mainly on the path length of the incident beam. Hence, the penetration depth of X-ray radiation is almost constant in a large range of angle ψ. The penetration depth *h* can be calculated from the formula [12]:

$$h \simeq \frac{\sin\alpha}{\zeta}, \tag{7.10}$$

where ζ is the linear attenuation coefficient for X-ray radiation for a given material. The values of α can be changed and hence it is possible to study stresses at different depths inside the material studied.

The value of stress, at a certain depth, is calculated for a constant penetration depth by measuring interplanar spacings for different hkl reflections corresponding to different ψ_{hkl} angles. The interpretation of the results requires the use of so-called equivalent lattice parameters, which are expressed by the macro stresses and strain-free lattice constants. A detailed explanation of the method used is given in the works of Marciszko and Baczmański [9,10].

The X-ray diffraction was carried out using a PANalytical Empyrean diffractometer with Cu Kα radiation and a parallel beam geometry (Göbel mirror in the incident beam optics and parallel plate collimator in the diffracted beam optics) over the 2θ range of 20–120°, step 0.02°, at room temperature. The geometry used minimizes the possibility of error connected with the positioning of the sample, which may have an impact on the determined values of stress.

To perform stress measurements, diffraction patterns were collected using the MGIXD method with 3 different incident angles: 5°, 10°, and 15°. In the calculations, all registered peaks from the XRD patterns were used.

Additionally, the single-angle technique for XRD residual stress measurement was used. The measurement allows obtaining information from a deeper layer and a larger volume than the MGIXD method. Residual stress was calculated using Stress Plus code, v. 2.1 by PANalytical B.V. Figure 7.4 shows the penetration depth dependence of the Cu Kα radiation in magnesium vs $\sin^2\psi$ for this measurement.

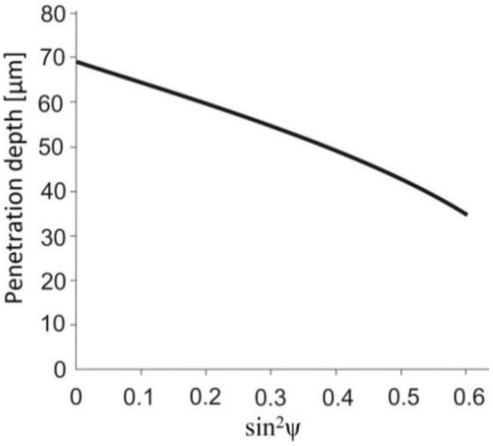

Figure 7.4 Penetration depth of X-ray radiation in the function of $\sin^2\psi$ for the single-angle measurement.

7.2.4 Microhardness tests

The hardness of a material can be defined as its resistance to a variety of shape changes under the influence of compressive forces acting on a small area. The strengthening mechanisms that influence the hardness of metals are an increase in dislocation density during mechanical treatments, reduction of the average grain size of the material, and the presence of alloying elements.

The mechanical properties of a solid determine its resistance to various mechanical factors. To determine these properties, hardness and microhardness tests are often used. Hardness measurement allows to easily determining the influence of various technological processes on the properties of a given material. The hardness of the material depends on, e.g., the nature of its chemical bonds, its structure, and microstructure. The size and shape of the specimen that is subjected to the hardness test also influence the selection of a specific test. Therefore, there are hardness tests suitable for various shapes and types of materials tested, i.e., dynamic, indentation, and scratch hardness [13-15].

The Knoop method was chosen in this study. It belongs to indentation hardness tests in which hardness is determined by the relationship between the force with which the indenter presses on the sample and the amount of permanent deformation caused by the indenter [14]. The Knoop method is usually used for hardness evaluation of thin films, where the use of small indentations is necessary. The test consists of a static indentation of the diamond made indenter in the shape of a pyramid with a rhombus base in the polished surface of the tested material. As the result of the indentation, the imprint of the intender is created on the specimen surface, which size is being determined by an optical microscope. The Knoop testing method allows measurements to be carried out very close to the edge of the sample, which played a key role in selecting this method, rather than the more popular Vickers method. The shape of the indenter allows for making imprints close to each other, which allows making in-depth microhardness profiles on the cross-sections of the samples. The measurement is almost non-invasive and causes only very slight damage to the sample surface. The shallow depth of the imprint and favorable stress distribution around the indenter prevents the formation of cracks around the imprints.

The Knoop test consists of indenting the indenter under a constant load F expressed in kgf and determining the length l of the longer diagonal of the imprint expressed in mm, as shown in Fig. 7.5. The Knoop hardness is calculated and determined as follows [14]:

$$HK = \frac{F}{C_{\mathrm{p}} l^2}, \tag{7.11}$$

where C_{p} is a constant related to the shape of the intender used.

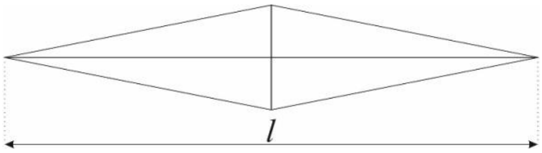

Figure 7.5 Knoop hardness indenter imprint.

Hardness tests that are performed with low loads (F <10 N) can be referred as to microhardness tests. Measurement of microhardness is most often used for samples that, due to their size, require the use of small loads during tests. For example, it is used when applying a high load to the indenter could pierce the sample.

The microhardness measurements were performed using a 2500 Instron ITW device with a Knoop indenter with a maximum load of 0.01 kg (HK0.01) at room temperature. Tests were performed after EBSD and optical microscopy evaluation of the microstructure of the cross-sectioned specimens. During measurements, the indenter longer diagonal was parallel to the trace of the SMATed surface.

7.2.5 Positron annihilation lifetime spectroscopy

A fast-fast spectrometer with BaF_2 scintillators was used for PALS measurements. The time resolution of the spectrometer was about 280 ps (FWHM).

Sodium isotope ^{22}Na enveloped into a 7 μm thick Kapton foil was used as a positron source. The source was 'sandwiched' between two identical samples and positioned in front of the scintillator detectors of the spectrometer.

All the obtained spectra containing more than 10^6 counts were analyzed using the LT code, taking into account the source contribution and background subtraction [16].

7.2.6 Variable energy positron beam and Doppler broadening spectroscopy

VEP beam was used to study microstructure changes of the near-surface region of the magnesium subjected to SMAT. VEP beam localized at the facility at the Joint Institute for Nuclear Research (JINR) in Dubna, was used [17]. The positrons were formed into a mono-energetic beam with an intensity of about 10^5 e^+/s and a diameter of 5 mm. The energy of implanted positrons ranged from 0.2 to 26 keV. The DB spectrometer with HPGe detector of resolution 1.1 keV was used.

7.2.7 Corrosion tests

Corrosion tests were performed in an all glass-and-PTFE (Polytetrafluoroethylene) cell with a platinum foil as a CE and the SCE as a RE. All potentials are reported versus that electrode. The WE with an exposed area of 0.25 cm^2 was placed at the bottom of the cell, in a horizontal position, with the active surface up to facilitate the liberation of the hydrogen formed in the Mg corrosion process. Fig. 7.6 shows photography of the used cell. Tests were performed in a 0.15 mol dm^{-3} NaCl saturated with $Mg(OH)_2$. Magnesium hydroxide is formed during the magnesium corrosion process due to the reaction: $Mg + 2H_2O = Mg(OH)_2 + H_2$. The pre-saturation of the test solution with $Mg(OH)_2$ stabilizes not only the composition of the solution but also pH, which is very important because the corrosion rate of magnesium strongly depends on pH. Note that the solubility of magnesium hydroxide in water is very low ($Ksp = 5.61 \times 10^{-12}$). The composition of solution used is close to the solutions in which magnesium objects corrode in practical applications, e.g., in the human body (implants) and the land transportation, e.g., sodium chloride is spilled on the road surfaces in winter.

Before the measurements, the solution was bubbled with argon to remove dissolved oxygen. The measurements were carried out at room temperature 21 ± 1 °C. Before the immersion in the electrolyte, specimens were cleansed with acetone. The measurements started with 2-h registration of the OCP. Then the LSV was performed to trace the polarization curve, starting from the potential of −0.2 V versus OCP in the anodic direction with the potential sweep rate of 1 $\mathrm{mVs^{-1}}$. Polarization was continued up to the attainment of the current density of ~10 $\mathrm{mA\ cm^{-2}}$. In some cases, LSV was preceded by the registration of the EIS spectrum in the frequency range of 10 kHz - 10 mHz and the amplitude of the sinusoidal voltage signal of 10 mV. Gamry G300 Potentiostat/Galvanostat/ZRA or Autolab PGSTAT 302N were used in the experiments.

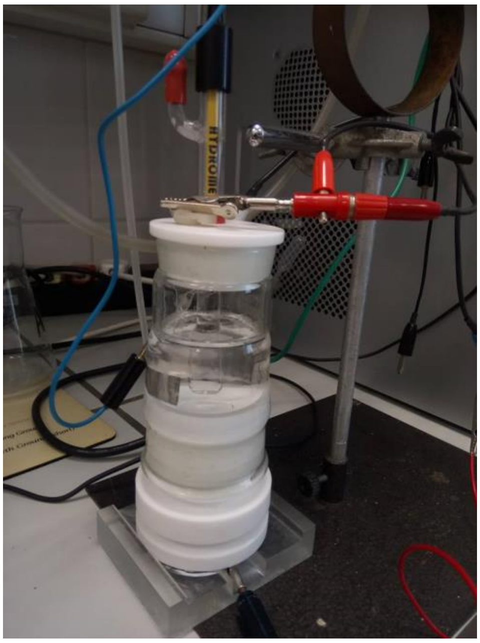

Figure 7.6 Photography of the glass-and-PTFE cell with a platinum foil as the CE and the SCE as the RE.

7.3 Results and discussion

7.3.1 Surface

Fig. 7.7 shows the morphology of Mg specimens prior to and after 60 s and 120 s of SMAT. On both SMATed surfaces, there are visible numerous craters that are a result of impacts of steel balls used in the treatment. The roughness parameter R_a was calculated from all the areas of the specimens visible in Fig 7.7 The value of R_a for the reference sample is about 1 μm. Processing with the SMAT increased the roughness parameter to 3.37 μm and 4.63 μm for 60 s and 120 s of SMAT duration, respectively.

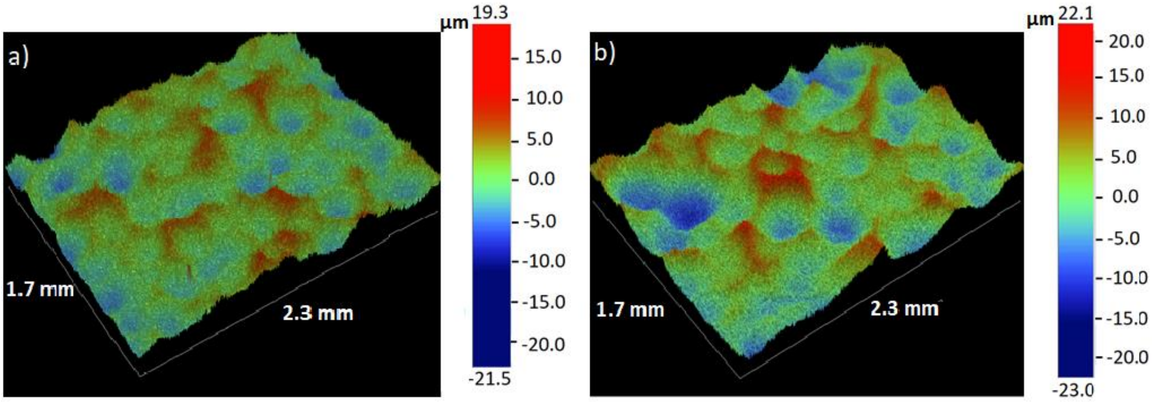

Figure 7.7 Optical profiler images of Mg samples surface SMATed for (a) 60 s and (b) 120 s.

It is a known fact that the increase in the surface roughness depends on the ball type and size, the treatment time, and the vibration amplitude [18,19]. For example, increasing the amplitude of vibration resulted in higher roughness of stainless steel [20]. The obtained roughness values of SMATed specimens are similar to those obtained by Laleh and Kargar for AZ91D alloy that was SMATed for 30 min with stainless steel balls with a similar diameter [21]. However, Li et al. reported higher values for pure Mg and Mg-1Ca alloy that were SMATed for times ranging from 40 to 90 min with 2 mm zirconia balls [22]. Nonetheless, Kargar et al. reported that the surface roughness dependence on the SMAT duration is not necessarily monotonic. These authors observed an initial increase in the surface roughness of copper after 10 min of SMAT and a slight decrease after 300 min [23].

The iron content in Mg is one of the most important parameters for its corrosion behavior. Figs. 7.8 and 7.9 show the EDS spectra for the reference sample and the sample SMATed for 120 s respectively. The data was collected from an area of about 250 x 250 μm^2. The performed SEM-EDS analysis did not show the presence of iron on the surfaces of the samples.

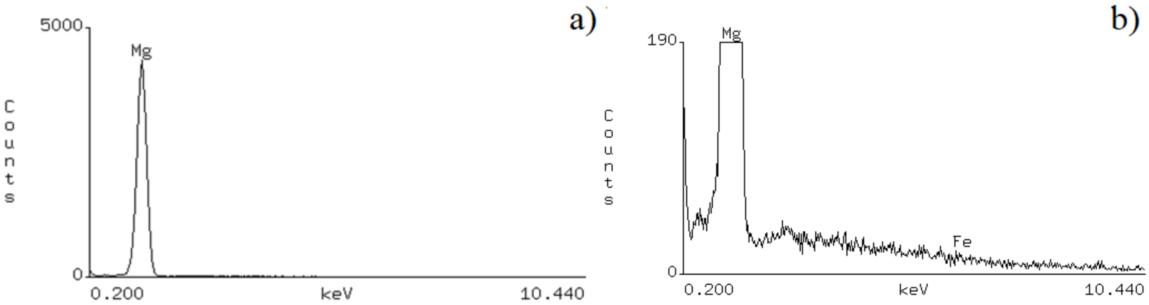

Figure 7.8 The SEM-EDS spectrum for the a) reference sample, b) region of interest.

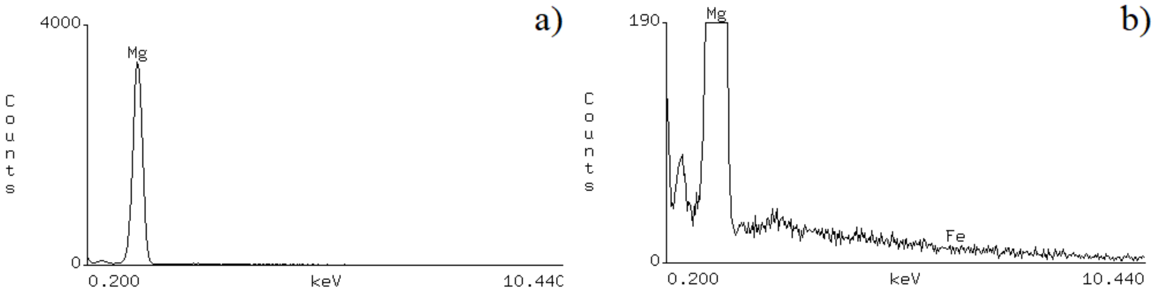

Figure 7.9 The EDS spectrum for the a) sample SMATed for 120s, b) region of interest.

7.3.2 Microstructure

The microstructure of the SMATed Mg was observed using optical microscopy with polarized light and the EBSD technique. Typical images of microstructure of cross-sectioned Mg SMATed for 60 s and 120 s obtained by use of EBSD technique and optical microscopy show Figures 7.10 and 7.11 respectively. The darker areas of the image are more deformed areas of the Mg microstructure. Near the surface of the sample SMATed for 60 s (bottom edge of Fig. 7.10) the refined grains are visible up to a depth of about 150-200 μm. Below, to the depth of about 400 μm the deformed area containing twins is visible. Deeper, the large grains are visible. Large grains are characteristic of the reference materials and their presence indicates the beginning of the bulk area of the specimen. The total depth of changes introduced by the SMAT can be estimated at 800 μm. This range corresponds well to the thickness of the hardened layer determined by microhardness measurements (see Chapter 7.3.3).

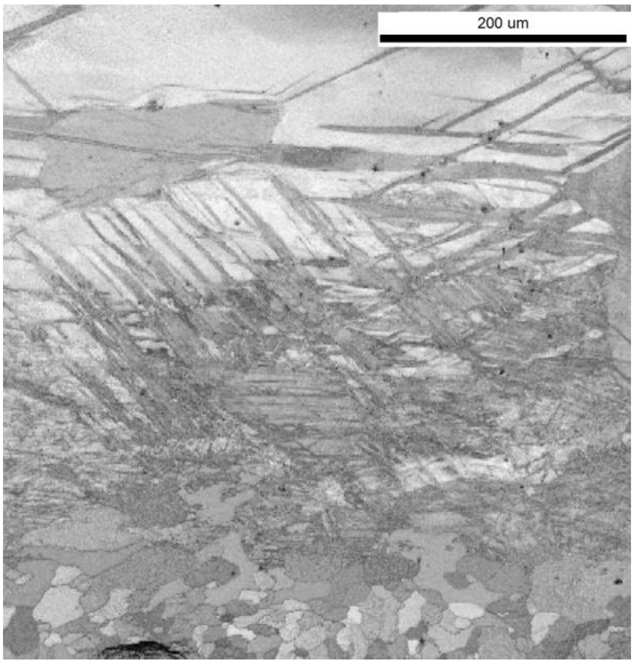

Figure 7.10 Image quality microstructure reconstructed from EBSD of the cross-sectioned specimen of Mg SMATed for 60 s.

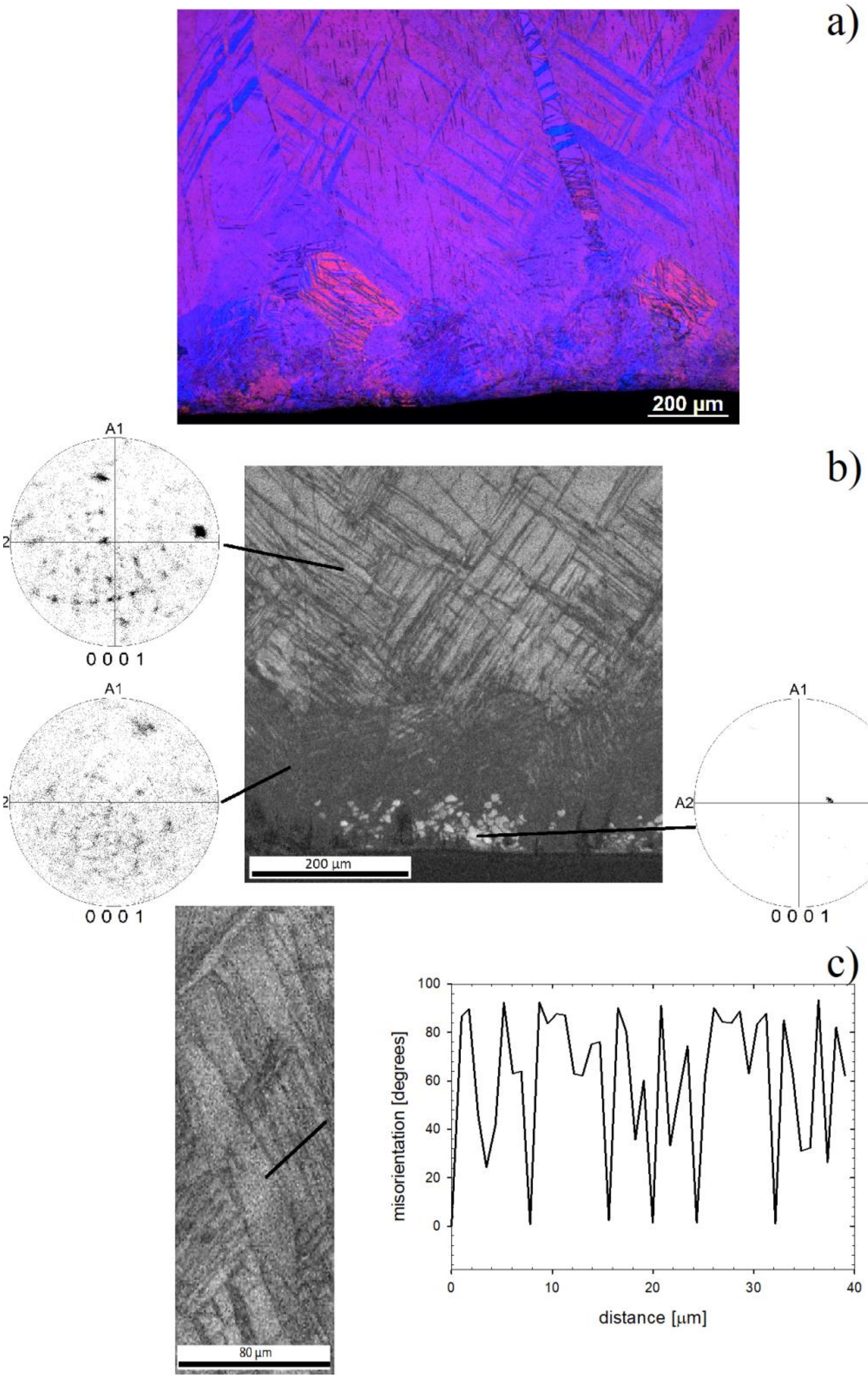

Figure 7.11 a) Optical microscopy image of a typical microstructure on the cross-section of the sample SMATed for 120 s; (b) the Image Quality Microstructure reconstructed from EBSD measurements and corresponding local crystallographic orientations shown in 0001 pole figures, and (c) magnification of a selected subsurface area with corresponding misorientations along the marked black line. SMATed surface is located at the bottom of images (adapted from [32]).

For the sample SMATed for 120 s, a much more significant decrease in the grain size in comparison to the one SMATed for 60 s is observed near the surface region. Deeper, there is also visible the gradual decrease in the number of characteristic twins belonging to different twinning systems when a distance from the surface increases (located at the bottom edge of Fig. 7.11 b). In the topmost layer, near the surface, up to the depth of about 80 μm, very small twin-free grains are visible. The presence of even smaller grains is not excluded, but a more resolved technique for their observation, e.g., a transmission electron microscope (TEM) may be needed. The estimated size of grains that are visible near the SMATed surface is less than 10 μm. The deformation twins are present from the very surface and their density is very high up to a depth of about 200 μm. A similar microstructure was created in the specimen SMATed for 60 s, however, the fine twin free grains are not visible. The estimated density of twins and the depth of the SMAT affected layer are larger in the case of sample SMATed for 120 s than the one treated for 60 s. These differences may arise from higher vibration amplitude and the SMAT time. An increase in both SMAT duration and the vibration amplitude leads to an increase in the energy imparted into the treated surface. The normal speed of shots depends on the vibration amplitude, i.e., an increase in the amplitude leads to a higher impact velocity [24]. Doubling the vibration amplitude leads to doubling the velocity of shots and hence their kinetic energy rises approximately fourfold. The total depth of 120 s SMAT induced changes extends to about 800-900 μm, which is in good agreement with the thickness of the hardened layer (see Chapter 7.3.3). It is also confirmed by the images obtained by optical microscopy (see Fig. 7.11). The visible SMAT affected layer extends also to the depth of about 800-900 μm. Due to the lower resolving power of optical microscopy than the EBSD method, direct observation of the refined, near-surface region is not possible. A gradual increase in the size of grains is observed with the depth from the SMATed surface. At a depth of about 400 μm, grains containing twins are visible. At greater depths, the structure characteristic for bulk is visible. The twins seen in this area most likely come from the sample preparation process.

A similar type of microstructure was reported for some SMATed hcp metals [25-28]. At a high strain rate at room temperature, mechanical twinning is the main deformation mode of hcp metals, such as magnesium and titanium, especially when the strain is not too high [28]. The grain refinement, as well as, strain hardening may be a result of twinning. Characteristic for twins misorientation of the crystal lattice are visible for Mg SMATed for 120 s in Fig. 7.11 [29]. The presence of twin-free grains near the SMATed surface may be attributed to recrystallization. Recrystallization nuclei and very fine recrystallized grains usually do not contain recrystallization twins, or the density of such twins is relatively low. The recrystallization of highly deformed, nano-grained materials can start at low temperatures. The formation of such twin-free grains can be related to a very low recrystallization temperature of pure magnesium. Ichikawa, reports that recrystallization of magnesium can start already at 75–175 °C [30], while thermomechanical simulations conducted by Rouquette et al. show that the temperature can reach locally 200 °C during shot impact [31]. Hence it is understandable that SMAT induced heat effects can result in the local recrystallization of highly deformed grains, which results in the formation of small grains, especially visible for specimen SMATed for 120 s (Fig. 7.11). Those grains are present only near the surface and only for the specimen SMATed for 120 s. It indicates that the thermal effect of SMAT is weaker than the strengthening one and that 60 s treatment with the lower vibration amplitude is not sufficient to induce both of them strongly. This explanation is confirmed by the results of the microhardness measurements (see Chapter 7.3.3).

Table 7.1 Calculated values of lattice crystallite size for magnesium samples.

sample	**crystallite Size [nm]**
Reference	205 ± 63
SMAT 60 s	38 ± 3
SMAT 120 s	37 ± 3
thickness reduction 10%	48 ± 6
thickness reduction 40%	35 ± 5

The XRD method was used to determine the effect of SMAT on the internal microstructure of the topmost layer of the samples. To calculate the average crystallite size, the W-H method was used. The values of the crystallite sizes are gathered in Tab. 7.1. SMAT significantly reduces the size of the crystallites in comparison to the reference sample. However, there is no significant difference between samples SMATed for 60 s and 120 s. Doubling the vibration amplitude and time of treatment does not influence the obtained crystallite size. A similar size of crystallites was calculated for the Mg deformed in the uniaxial press to 40% thickness reduction. For 10% thickness reduction, a slightly larger size of crystallites was obtained. A similar crystallite size in pure SMATed Mg was reported by Li et al. [22]. Obtained values of lattice strains are comparable to the error of the W-H method applied. It is equal to 0.01(1)% for the reference sample, the sample SMATed for 60 s, and the compressed sample with 10% thickness reduction. For the sample treated for 120 s and the pressed one with 40% thickness reduction, the lattice strain is slightly higher (i.e., at least 0.02(1)%).

The $\omega \sin^2\psi$ method was used to determine the effect of SMAT on residual stresses in magnesium samples. Figure 7.12 shows the dependencies of lattice spacing in the function of $\sin^2\psi$. Solid lines represent the best fit to the experimental points. The stress values are calculated from the slope of the fit. The values of residual stresses introduced during SMAT are equal to -6.1 ± 1.2 MPa and -8.2 ± 2.6 for the samples treated for 60 s and 120 s respectively. It has to be mentioned that the penetration depth of the X-ray beam varied during the measurement series due to multiple ψ tilts, while φ remained constant, equal to 180°. The penetration depth of the X-ray beam varied between c.a. 70 μm and 35 μm (see Fig 7.4). Hence the information about the residual stress values obtained by the $\sin^2\psi$ method comes from this depth range.

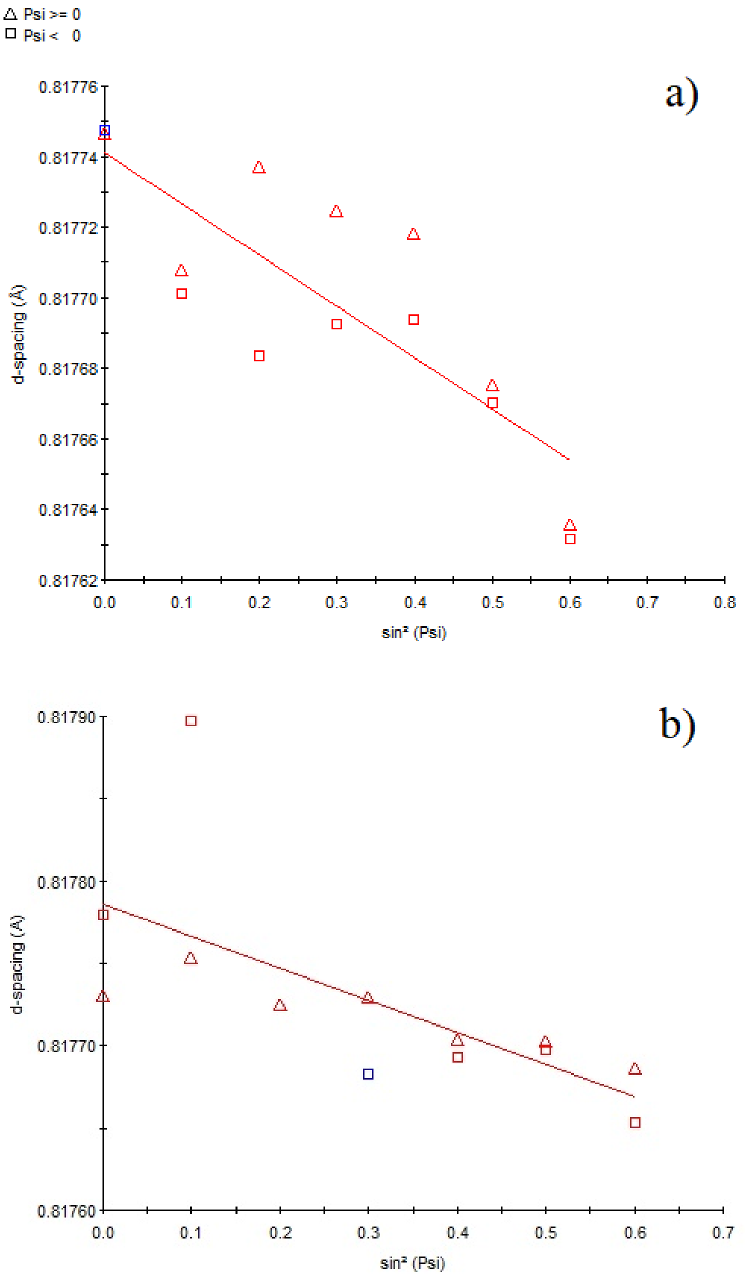

Figure 7.12 Dependencies of lattice spacing in the function of $\sin^2\psi$ for a) sample SMATed for 60 s and b) SMATed for 120 s (Stress Plus program, v. 2.1 by PANalytical B.V).

To measure residual stresses just below the SMATed surfaces the MGIXD method was used. Application of MGIXD method made it possible to determine residual stresses for 3 different penetration depths: 12 µm (for $\alpha = 5°$), 21 µm (for $\alpha = 10°$), and 29 µm (for $\alpha = 15°$), where α is the X-rays angle of incidence. The calculated values of residual stresses are gathered in Tab. 7.2. No significant effect of SMAT (regardless of the process duration and the vibration amplitude) on residual stress was found. The calculated values of residual stresses are small. The values of stresses determined for $\alpha = 5°$ are within the error range of the method. It can be assumed that they are negligible in the probed depth up to 12 µm. Between the depth of 21 and 29 µm calculated values of stresses remain low. The $\omega\sin^2\psi$ method measurements show that at the depth between 35 µm and 70 µm values of stresses introduced during SMAT are equal to -6.1 ± 1.2 MPa and -8.2 ± 2.6 MPa for the samples treated for 60 s and 120 s respectively.

Table 7.2 Values of residual stresses σ_1 and σ_2 calculated from MGXID data.

sample	**α[°]**	**σ_1[Mpa]**	**σ_2[Mpa]**
SMAT 60 s	5	-2.8 ± 2.7	0.2 ± 2.7
	10	-2.1 ± 2.2	0.1 ± 2.2
	15	-5.1 ± 1.9	-1.9 ± 1.9
SMAT 120 s	5	2.4 ± 2.1	0.4 ± 2.1
	10	4.7 ± 2.5	3.5 ± 2.5
	15	-2.7 ± 2.2	-3.6 ± 2.2

Low residual stresses in SMATed Mg correspond to very low lattice strain values obtained by the W-H method. A similar low lattice strain value, below 0.06% was obtained by Li et al. for SMATed with 2 mm zirconia balls Mg [22]. Those authors also observed lattice strain increase up to 60 min of SMAT, but extending the time of process for another 30 minutes leads to a significant decrease of the lattice strain. Low lattice strain, about 0.1% was also reported by Liu et al. for the GW63K Mg alloy SMATed for 3 min [33]. Similar results of low compressive residual stresses were also reported by Fabijanic et al. for SMATed magnesium. However, they used different treatment parameters in comparison to the present study, such as longer treatment time – 60 min, greater ball diameter, i.e., 11 mm, 8 mm, and 10 mm, for alumina, steel, and zirconia balls, respectively, and much lower vibration frequency – 50 Hz. The process resulted in the introduction of residual stresses of 7.1 ±2.8 MPa, 6.5±2.6 MPa, and 12.4 ± 4.6 MPa for treating with steel, alumina, and zirconia balls, respectively [34]. It can be seen that ball material has a considerable influence on residual stresses, i.e., the use of zirconia balls resulted in the introduction of significantly higher residual stresses than the steel balls used in the present work. There are reports of higher residual stresses introduction during SMAT or similar SP methods in magnesium alloys, e.g., in severely shot-peened AZ31 the maximum value of residual stress is about 50 ± 10 MPa at the depth of 100 μm under the treated surface [35].

The absence of residual stresses near the surfaces of the SMATed Mg specimens corresponds well with the microstructure observation made by the use of the EBSD method. As it can be seen, the visible layer that contains recrystallized grains (Fig. 7.11) extend to a depth greater than the penetration depth of X-ray radiation used in the MGIXD method. The recrystallization phenomenon is preceded by stress relief during recovery which explains the obtained results [36,37]. The obtained values of residual stress in SMATed magnesium, due to its low melting point, can be attributed to their ease of recrystallization. For the other hcp metals, with much higher melting points such as Ti and Zr, much higher compressive residual stresses values, reaching several hundred MPa, were reported [38-41].

7.3.3 Microhardness profile

Fig. 7.13 presents the microhardness values changes with the increasing depth from the surfaces of the specimens. The measurements were carried out on the cross-sectioned samples starting from the very near of the SMATed surfaces. The microhardness measured at a depth of about 40 μm for the sample SMATed for 120 s is 1.8 times higher than the value for the reference sample. For the specimen treated for 60 s, a slightly lower increase in microhardness value was observed, i.e., 1.55 at the same depth from the surface. Both obtained microhardness profiles are similar to each other. The microhardness values gradually decrease with the distance from the SMATed surface to the depth of about 800-900 μm where they reach values for the reference sample. Both dependencies of microhardness on the depth can be described with by exponential decay functions: $HK_{60}(z) = 0.98 + 0.7\exp(-z/268)$ and $HK_{120}(z) = 0.94 + 0.9\exp(-z/322)$ for specimens SMATed for 60 s and 120 s respectively. The depth at which the microhardness value drops to 1/e of their initial values can be referred to as the decay length. Values of the decay length are equal to 268 μm and 322 μm for 60 s and 120 s treatment time, respectively. The difference between those values is small and is comparable with their uncertainties. Hence, it can be stated that there are no differences in the total thickness of the deformed layers created during 60 s and 120 s treatment duration.

The obtained values of microhardness near the surfaces of the SMATed Mg specimens show that doubling both the amplitude and the SMAT duration results in the creation of a harder layer. It is explained by the fact that, during 120 s of SMAT due to a higher amplitude, and thus speed of shots, more energy was imparted to the surface of the specimen than in the case of 60 s process duration [42]. Literature reports suggest that extending SMAT duration has a small influence on the resulted hardness of the material treated. This was reported, e.g., for Mg, Mg-1Ca, and AZ31 alloys [22,43]. Effect of SMAT duration on hardness profile is more visible for shorter treatment times, e.g., for AZ31B alloy two- or three-fold extension of time resulted in an approximate increase in hardness from 70% to 120%, which is comparable to the present results [44].

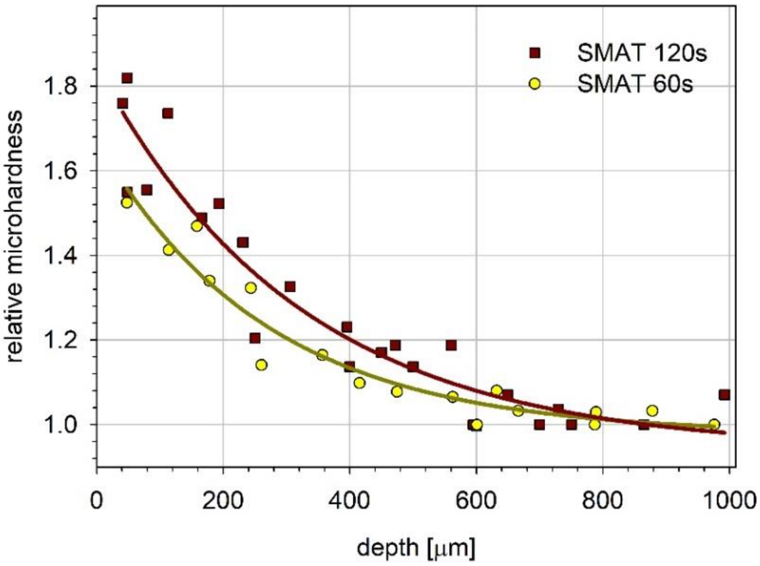

Figure 7.13 The relative microhardness of magnesium samples SMATed for 120 s and 60 s versus depth. The solid lines represent the best fit of the exponential decay function to the experimental points: $HK_{60}(z) = 0.98 + 0.7\exp(-z/268)$ and $HK_{120}(z) = 0.94 + 0.9\exp(-z/322)$ for 60 s and 120 s-SMATed samples, respectively; z is the depth beneath the surface (adapted from [32]).

The number of papers relating to the hardness profiles for SMATed pure magnesium is very limited, while information on magnesium alloys is more frequent. Li et al. reported an increase in hardening of the near-surface region of SMATed pure Mg reaching 120% of the reference value, with the creation of a hardened layer to the depth of 1.75 mm. For Mg-1Ca treated in the same way, the creation of a 1-mm thick hardened layer with a maximum of 180% increase in hardness after SMAT was reported [22]. Moreover, the shape of the microhardness profile is very similar to the profiles obtained in the present research. SMAT of Mg-6Gd-3Y-0.5Zr for 3 min resulted in the creation of a 1.2 mm thick hardened layer [45].

7.3.4 Positron lifetime measurements

Only one positron lifetime was resolved in the measured positron lifetime spectra. The possible explanation of this fact is the presence of a variety of crystal lattice defects with positrons lifetimes that values only slightly differ from each other. The finite time resolution of the spectrometer used did not allow them to be distinguished. The obtained lifetime values can be treated as the mean positron lifetime $\overline{\tau}$.

The implantation range of positrons is much shorter than the total thickness of SMAT affected layers determined in the microhardness test and observed on the EBSD images. Therefore, it is possible to use a method based on the chemical etching of subsequent sample layers to obtain the annihilation characteristics, i.e., mean positron lifetime depth-profiles as was described in Chapter 6. Thin layers of samples were removed by sequential etching in Nital and PALS measurements were carried out. The contribution to the measured value of the positron lifetimes comes from a layer of thickness comparable to $1/\mu$. The linear absorption coefficient μ for positrons emitted from the ^{22}Na source implanted in magnesium is equal to ca. 76 cm^{-1} (Table 4.1). Therefore, the mean implantation depth of positrons is about 130 μm, while the SMAT affected layer is almost 1 mm thick.

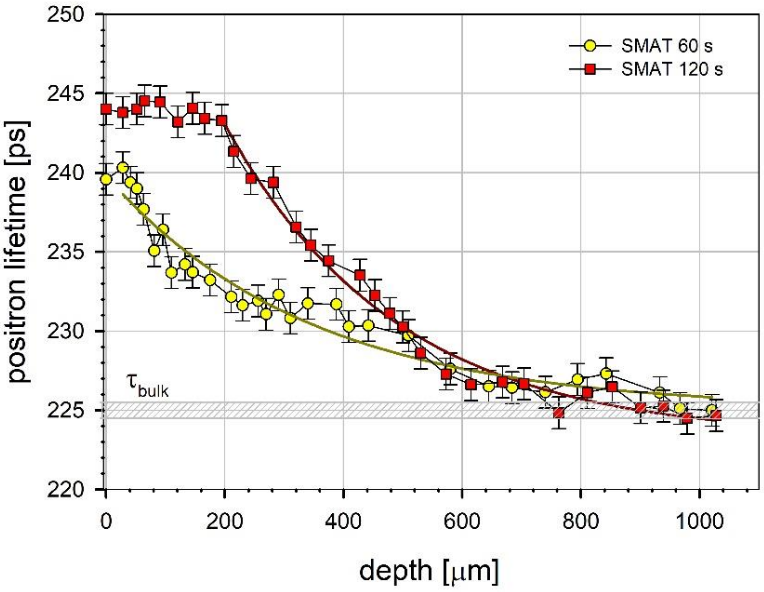

Figure 7.14. The mean positron lifetime profiles. The solid lines represent the best fit of the exponential decay function to the experimental points (adapted from [32]).

Figure 7.14 presents the mean positron lifetime dependencies on the depth from the SMATed surfaces of the magnesium samples. The value of the positron lifetime measured for the reference sample τ_{bulk} is equal to 225 ± 1 ps. The obtained value for the bulk sample is in good agreement with the values obtained by Hautojärvi and Rio [46,47]. The values of the mean positron lifetimes measured on the surfaces of the SMATed specimens are equal to 240 ± 1 ps and 244 ± 1 ps for 60 s and 120 s treatment durations, respectively. They are almost constant up to the depth of about 200 μm in the case of the sample SMATed for 120 s. Deeper, the mean positron lifetime gradually decreases between 195 μm and 600 μm. Then its decrease is much slower up to the depth of 900 μm where it reaches the value obtained for the reference sample. For the specimen SMATed for 60 s, a decrease in the measured $\bar{\tau}$ is already visible just below the treated surface. The value of the mean positron lifetime decreases with the depth and reaches τ_{bulk} for the depth slightly larger than 900 μm.

The obtained depth dependencies of the mean positron lifetime and microhardness are similar. For the sample SMATed for 120 s, both lifetime and microhardness (see Fig. 7.13) values are higher than for the one treated for 60 s. Both quantities take their highest values near the surfaces for both SMATed samples, and then they decrease with the depth from the surfaces to the values obtained for the reference sample. The total range of changes of microhardness and positron lifetime is similar. However, it should be noted that because positrons emitted from ^{22}Na have a continuous spectrum not all of them annihilate at the same depth. Therefore, the mean positron lifetime is averaged over some volume of the sample, which results in the reduction of the scattering of the measurement points. The solid lines in Fig. 7.14 represent the best fit of the exponential decay function to the experimental points: $\bar{\tau}_{60}(\text{in ps}) = 225 + 13.6\exp[-(z-28)/342.8]$ for the specimen SMATed for 60 s and $\bar{\tau}_{120} = 223 + 20.2\exp[-(z-195)/285.7]$ for the one SMATed for 120 s, where z is the depth from the treated surface in μm.

High values of the mean positron lifetimes measured on surfaces of both SMATed samples indicate the creation of a layer rich in crystal lattice defects. The value of the mean positron lifetime measured on the surface of the sample SMATed for 60 s is shorter than for the 120 s one. It indicates a lower crystal lattice defect concentration under the surface treated for 60 s. The obtained depth dependencies of the microhardness and positron lifetime, as well as, EBSD maps reflect well the defect depth distribution below the treated surfaces. The visible plateau of the positron lifetime under the surface of specimen SMATed for 120 s coincides with the high values of microhardness and the highly deformed layer that contains a high density of twins observed on the EBSD map (Fig. 7.11). Additionally, the fine grains that are visible on the EBSD images may contain defects that are also responsible for positron trapping. According to Sun et al., the strain rate in SMAT is much higher, in comparison to other severe plastic deformation processes, such as HPT or ECAP, which leads to obtaining smaller refined grains [48,49]. As it was shown by Okhubo et al., the strain rate can also influence the generated crystal lattice defects [50]. The reduction of the number of twins with the increasing depth from the surfaces is accompanied by the decrease in the values of $\overline{\tau}$ for both 60 s and 120 s treatment times. In the case of the sample SMATed for 60 s, the defect concentration starts to decrease much closer to the surface.

Values of the mean positron lifetime similar to those obtained in the present study for SMATed Mg were reported by Dryzek for magnesium subjected to dry sliding against stainless steel [51,52]. It can be explained by the fact that both SMAT and sliding friction result in the creation of the subsurface region rich in defects. A plateau similar to this observed for the magnesium sample SMATed for 120 s was found for other metals and alloys subjected to much longer sliding distances [53]. It was attributed to the accumulation of deformation for repeating passages of a sample over a hard counterface in the pin-on-disc sliding experiment.

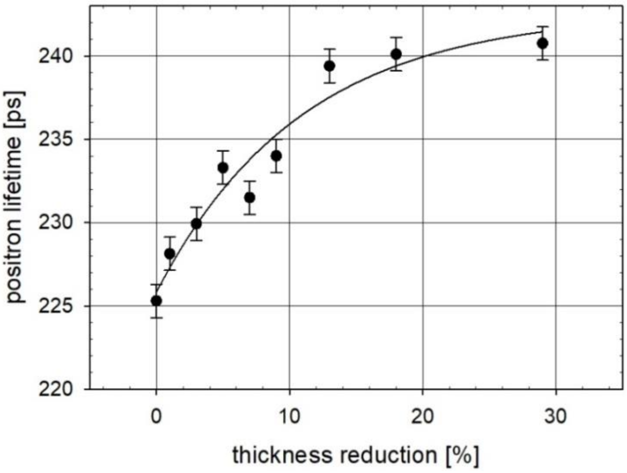

Figure 7.15 Mean positron lifetime values as a function of thickness reduction for the Mg specimen deformed using the uniaxial-hydraulic press. The solid line is a guide eye.

For comparison purposes, one of the well-annealed Mg specimens was deformed with the use of a hydraulic press. Fig. 7.15 shows the mean positron lifetime values for the sample deformed by compression using the uniaxial-hydraulic press. After each thickness reduction with the hydraulic press, the positron lifetime was measured. The thickness reduction of the Mg specimen is accompanied by a quick rise in the value of the positron lifetime. This indicates a sharp increase in the number of crystal lattice defects that are a result of the sample compressing. This type of dependency is typical for deformed metals. For higher deformation, the concentration of crystal lattice defects is high enough to trap almost all positrons, and thus saturation of the measured lifetime takes place. A high degree of deformation in magnesium results in the activation of multiple slip systems, the interaction of moving dislocation, and the creation of jogs on their lines. However, trapping of positron by twin boundaries has to be taken into account as well, as it was reported by Serra and de Diego for deformed titanium [54]. Dislocations that are associated with twin boundaries can act as positron traps characterized by lower lifetimes than those of pure lattice dislocations. It is explained by the fact that vacancies and dislocations minimize their open volume when they are localized in twin boundaries. Hence, dislocations and their jogs, and accompanying vacancies may be responsible for trapping positrons in severely deformed magnesium. Therefore, due to the limited resolving power of the lifetime spectrometer used and the fact that potentially a few different types of defects could have been introduced during plastic deformation of magnesium, it is necessary to analyze the obtained positron lifetime spectra in terms of the mean positron lifetime especially in the case of the SMATed samples. For magnesium deformed by compression, there was reported a successful attempt of resolving two positron lifetime components. Del Rio et al. ascribed the lifetime component of 253 ps to the annihilation of positrons trapped in jogs and 244 ps to positrons trapped in dislocations without jogs [47]. The mean positron lifetime much shorter than 253 ps was explained by a contribution of positrons annihilating in undisturbed crystal lattice regions. For comparison, the values of the positron lifetime in Mg monovacancies reported by Häutojarvi et al. and Folegati et al. are equal to 253 ps and 245 ps, respectively [46,55].

A similar phenomenon of positron lifetime saturation is visible for the sample SMATed for 120 s. However, in this case, the lifetime plateau is observed for the slightly longer mean positron lifetime, i.e., 244 ps. The obtained values of the positron lifetime for magnesium specimens subjected to SMAT can be compared with those obtained by Čížek et al. for ultrafine-grained bulk magnesium obtained by HPT, in which two lifetime components were resolved in the spectra [56]. The longer one equal to 257 ps was attributed to the vacancies associated with dislocations. The shorter one with an intensity of 39% was equal to 188 ps, which is significantly lower than the value for bulk Mg. Such a short positron lifetime was attributed to annihilation in recrystallized regions which were created as a result of dynamic recrystallization. The mean positron lifetime calculated by Cizek was equal to 230 ps, which still is much shorter than the value obtained at the SMATed surface even for only 60 s SMAT duration in the present study. This may also confirm that in the case of SMATed Mg a much higher density of defects was created.

7.3.5 Variable energy beam measurements

To study a near-surface region of the sample, the VEP beam was used. The technique enables locating positrons at a small depth below the surface of the sample. Positrons that are diffusing back to the surface can be trapped in surface states or near-surface defects or they can form positronium atoms. In general, the value of the S- parameter measured for a given positron incident energy is a weighted average of its values for positron annihilation from different states: free positrons, positrons trapped in defects inside the material, and positrons annihilating from surface-related states. Transport of thermalized positrons in solids is described by a diffusion theory in which the positron diffusion length L_+ is a crucial parameter depending on the properties of the material such as, e.g., the density of the crystal lattice defects that are present. Hence, the positron diffusion length value can be used to characterize the internal structure of materials studied and it can be even used to determine the dislocation density inside the material [57].

The dependencies of the S-parameter values as a function of the positron incident energy measured for the samples SMATed for 60 s, and 120 s, as well as, the reference one, and the same samples after etching in Nital are shown in Fig. 7.16. Additionally, for comparison purposes, the results for the sample compressed to 23 % thickness reduction, and then etched in Nital are also shown. The top horizontal axis denotes the mean implantation depth of the annihilating positrons calculated using the formula: $\bar{z}[nm] = 1.4E^{1.757}$, where E is the positron incident energy in keV [58]. The low values of the S-parameter obtained for low positron energies indicate the formation of oxide layers on surfaces of samples [59-62].

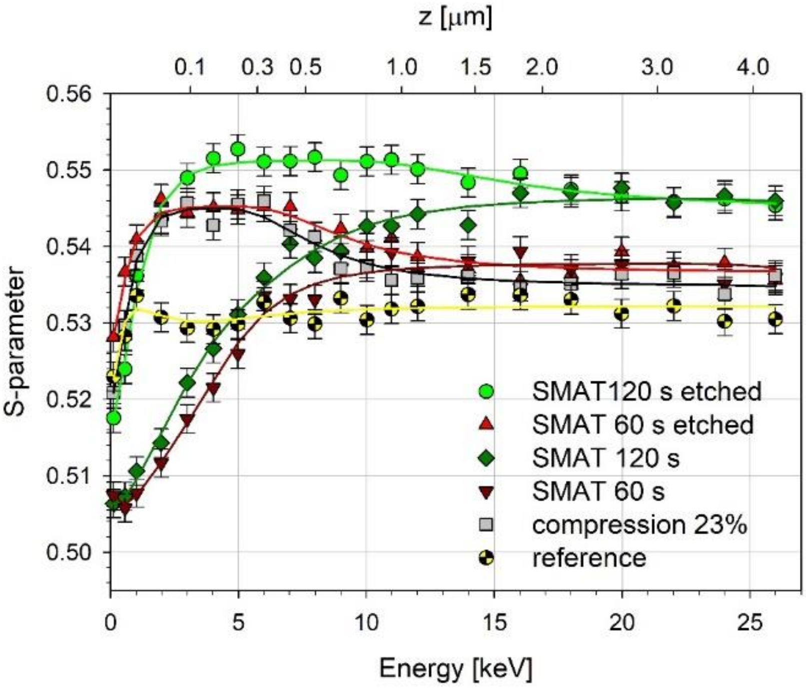

Figure 7.16 The *S*-parameter as a function of incident positron energy (mean implantation depth) (adapted from [32]).

In the case of SMATed specimens without etching, the values of the S-parameter increase with the increase of the implantation depth, and then, at certain depths they saturate. The depths at which the S-parameter saturates, as well as, saturation value differ for both SMATed samples. For the specimen SMATed for 60 s, the S-parameter saturates at about 7 keV, while, for the 120 s SMATed sample, it saturates at higher energy, even close to 12 keV. It can be stated that, in this range of incident energies, and thus in a certain implantation range, positrons penetrate mainly the oxide layer that was created on the surfaces of the Mg specimens. For higher positron energies, the metal matrix is penetrated. The higher saturated value of the S-parameter for the 120 s SMATed sample than that for the 60 s SMATed sample is in good agreement with the higher value of the mean positron lifetime measured using the conventional PALS method discussed in Chapter 7.3.4. The higher values of the S-parameter indicate a higher concentration of positron trapping defects induced by SMAT in the metal matrix.

To confirm this explanation of the shape of S-parameter profiles, the oxide layer was removed from specimens by etching in Nital, and the VEP measurements were repeated. It should be noted that due to the high reactivity of magnesium towards oxygen, oxide layers were spontaneously formed at the surfaces of the samples after etching. The additional measurement was performed for the sample compressed to the thickness reduction of 23%. The shape of the S-parameter profiles obtained for the etched samples are similar to each other but differ significantly from those obtained for non-etched samples. The values of the S-parameter on the surfaces are higher than before etching. The S-parameter increases for the positron energy up to 5 keV for the 120 s SMATed sample and up to 2 keV for the 60 s SMATed and the compressed samples. A broad maximum of S-parameter values, after which the S-parameter decreases to the saturated level obtained for the non-etched samples is visible in Fig 7.16. Therefore, the saturated values of the S-parameter correspond to the annihilation of positrons in the metal matrix of the samples. The increase in the S-parameter to higher values than for the metal matrix indicates the presence of open volume defects induced by etching. Similar dependencies were observed for aluminum [59,64]. The broader maximum and the higher values of the S-parameter for the sample SMATed 120 s compared with the sample SMATed for 60 s indicate a higher concentration of defects. Therefore, it can be stated that sample SMATed for 120 s has got a higher reactivity towards oxygen than the one treated for 60 s.

For a given positron energy E (i.e., penetration depth), the measured S-parameter can be expressed as:

$$\mathrm{S} = F_S S_S + F_{ox} S_{ox} + F_{id} S_{id} + F_m S_m \tag{7.12}$$

where F_s, F_{ox}, F_{id}, and F_m are the fractions of positrons annihilated at the surface, in an oxide film, at defects (including the oxide film/matrix interface and pores, etc.), and the metal matrix, and S_s, S_{ox}, S_{id}, and S_m are the corresponding values of the S-parameter in these regions. The obtained dependencies of S(E) were fitted using the VEPFIT code. The program solves the diffusion equation taking into account the positron implantation profile. The results of fitting are solid lines in Fig. 7.16 [65]. The fitting was conducted with the assumption that the positron diffusion length in the metal matrix of the samples is much shorter than diffusion length in the annealed defect-free magnesium, which is close to 200 nm [66]. It can be stated that the shorter diffusion length of positrons in the metal matrix of the SMATed specimens is caused by the presence of crystal lattice defects, which is confirmed by the PALS measurements presented in Chapter 7.3.4. For example in Mg films prepared by radio frequency magnetron sputtering at room temperature reported by Hruška et al., the positron diffusion length was about 35–45 nm [67]. The shortening of the positron diffusion length in the case of those films was caused by defects, such as misfit dislocations necessary for the accommodation of the lattice mismatch between the film and the substrate and open volume point defects (vacancies and vacancy clusters) located at grain boundaries. It can be assumed that due to the severe plastic deformation during SMAT, crystal lattice defects were introduced in the metal matrix. Hence SMATed samples have similar or lower values of positron diffusion length than those reported by Hruška. This assumption makes it possible to obtain the positron diffusion length in the oxide layer for the SMATed samples. The calculated values of the positron diffusion length and thickness of oxide layers are gathered in Table 7.3. For both SMATed samples before etching, the positron diffusion length has got a higher value, about 74 nm. The obtained value is comparable to those reported by Yang et al. for the layer of the corrosion products for AM60B magnesium alloy immersed in NaCl solution for longer immersion times and higher thickness of the layer [68]. The calculated thickness of the oxide layers for the SMATed and the reference samples correlate with their corrosion resistance estimated by electrochemical tests discussed in Chapter 7.3.6. The increase in the oxide layer thickness with the increase of SMAT time suggests that the process increases the susceptibility of Mg to oxidation.

Information about the type of defects that are present in the studied samples can be obtained from the W_r- versus S-parameter plot, as shown in Fig. 7.17 [69,70]. A straight-line segment in such a plot indicates that only two positron states contribute to annihilation. The end-point of this segment corresponds to phases or defects having particular S- and W_r-parameters. Points in Fig. 7.16 for which an increase of the S-parameter starts at the surface lie along a straight line in Fig. 7.17. For higher values of the positron incident energy, the points deviate from this straight line. Similar behavior has been observed for AM60B magnesium alloy after short immersion in NaCl solution [71]. It was explained by the presence of an oxide layer and then a corrosion product layer, whose thickness increased with the increase of the immersion time. The states from which positrons annihilate in the metal matrix of the samples SMATed for 60 s and 120 s, and the compressed sample may differ because of different kind and amplitude of deformation and possibly different kinds and densities of defects. Nevertheless, the points for which the S-parameter values saturate in Fig. 7.16 are gathered in three locations in Fig. 7.17. The first cluster of points is depicted as bulk for the sample SMATed for 120 s, the second one as bulk for the specimen SMATed for

60 s, and the third one as bulk for the compressed sample. There is almost no difference in $W_r(S)$ dependency for the sample SMATed for 60 s and the compressed one. It can be seen that the points for those three samples lie along the same straight line as the points for the annealed Mg. This can be explained by the fact that there are similar types of defects that are present in the metal matrixes of all Mg specimens, and only their concentration changes.

Table 7.3 Results of fitting of the S(E) curves. L_{+layer} is the positron diffusion length in the surface layer of the samples, which is different from the magnesium matrix, and *d* is the thickness of this surface.

sample	**L_{+layer} [nm]**	**d [nm]**
SMAT 60 s	74 ± 4	148 ± 9
SMAT 120 s	74 ± 2	370 ± 32
reference	21 ± 10	80 ± 43
SMAT 60 s & etched	6 ±2	320 ± 2
SMAT 120 s & etched	12 ± 1	708 ± 78
Compressed & Etched	6 ± 1	266 ± 18

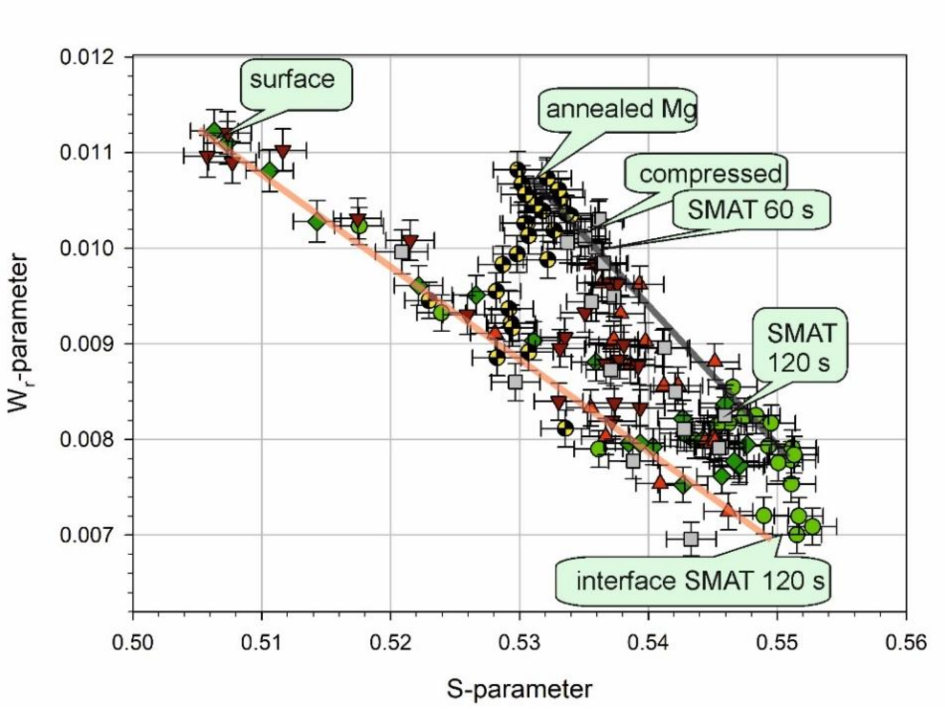

Figure 7.17 W_r-parameter as a function of S-parameter. The symbols are the same as in Figure 7.16 (adapted from [32]).

7.3.6 Corrosion resistance

The corrosion rate of magnesium is relatively high and changes significantly with time [72,73]. This makes evaluating its corrosion rate a rather difficult task because the properties of the sample change during the time of measurement. To evaluate the corrosion resistance of SMATed magnesium the parameters were calculated from the LSV measurements: corrosion potential, E_{corr} (the potential at which the plot $j = f(E)$ crosses the abscissa), polarization resistance (derivative dE/dj at E_{corr}), and the corrosion current density, j_{corr}. Corrosion current density was calculated by the extrapolation of the linear segment on the cathodic branch of the $j = f(E)$ curve traced in the semi-logarithmic coordinates to E_{corr}. It has to be mentioned that, the product of j_{corr} and R_{p} should be constant for a given material and electrode reaction mechanism but it was roughly fulfilled in the magnesium measurements (Table 7.4). EIS was performed at OCP, and the EEC used for fitting the impedance data is shown in Fig. 7.18. An example of the fit is shown in Fig 7.19. For the EEC showed in Figure 7.18, the polarization resistance, i.e., the parameter characterizing the susceptibility of a material to corrosion, is calculated from the formula:

$$\frac{1}{R_{\mathrm{p}}} = \frac{1}{R_{\mathrm{T}}} + \frac{1}{R_{\mathrm{L}}} \tag{7.13}$$

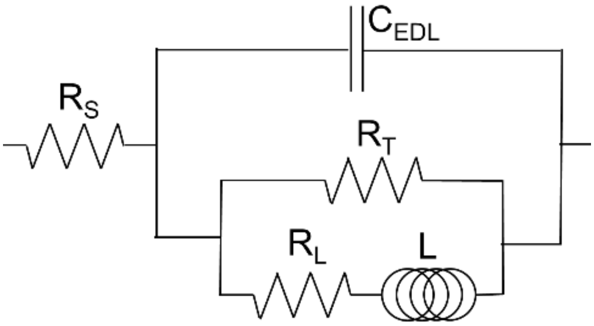

Figure 7.18 EEC applied in the interpretation of the data from electrochemical impedance spectroscopy measurements. R_S = resistance of the solution, C_{EDL} = capacitance of the electrical double layer, R_T = charge-transfer resistance, L = inductance of the electrode process, R_L = resistance connected with the inductance of the electrode process.

Fig. 7.19 shows an example of the fit of the EEC model to the EIS data. Fig. 7.20 and Table 7.4 show the results of the most representative series of measurements. The total number of three series of measurements was performed during which commonly observed variations in obtained results occurred. A variation in corrosion measurements with nominally identical materials was reported, e.g., by op't Hoog [74]. However, the basic characteristics of the material behavior, namely: $E_{\mathrm{corr}}^{0} < E_{\mathrm{corr}}^{60} < E_{\mathrm{corr}}^{120}$, $j_{\mathrm{corr}}^{0} > j_{\mathrm{corr}}^{60} > j_{\mathrm{corr}}^{120}$, and $R_{\mathrm{p}_{\mathrm{corr}}}^{0} < R_{\mathrm{p}_{\mathrm{corr}}}^{60} < R_{\mathrm{p}_{\mathrm{corr}}}^{120}$ were always preserved during series.

The SMAT process strongly influenced the behavior of magnesium specimens in polarization experiments. The cathodic branch of the polarization curve practically did not change after the SMAT process, while the differences in the anodic branch were very significant, as can be seen in Fig. 7.20. The magnitude of the corrosion current decreased for the longer SMAT duration, and the shape of the curve changed, and E_{corr} was shifted in the anodic direction. Approximately at -1.4 V bulges are visible on the curves registered for the SMATed samples. The anodic branches of all three curves show kinks reminiscent of breakdown potential, the more numerous the longer the SMAT process was. After the attainment of the potential of ~1.0 V, the curves coincide with each other. This indicates that the anodic process is no longer controlled by the surface properties of the sample, and at this point, probably transport becomes the controlling factor.

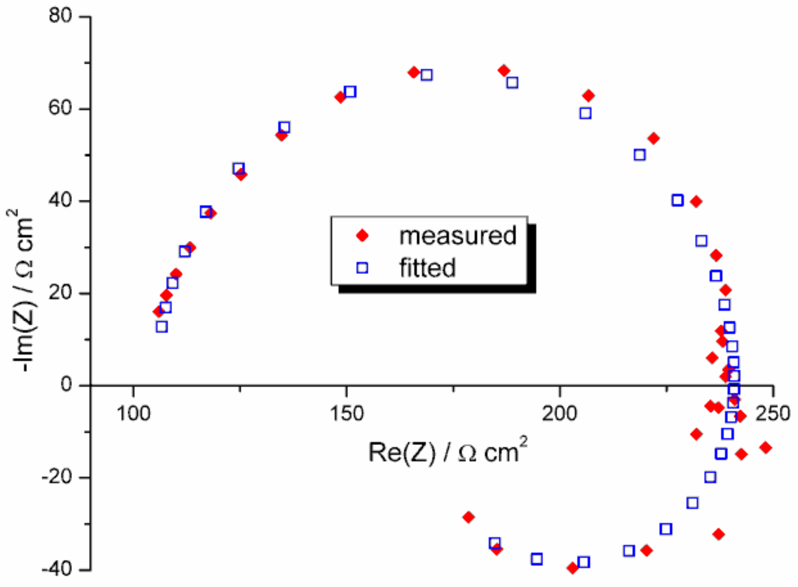

Figure 7.19 An example of the fit of the EEC showed in Fig. 7.18 to the impedance data. Mg not subjected to any treatment (reference sample) in 0.15 mol dm^{-3} NaCl solution saturated with $Mg(OH)_2$ (adapted from [32]).

All these observations lead to the conclusion that SMAT does not decrease but rather increases the susceptibility of magnesium to anodic oxidation. This, in turn, leads to the enhanced formation of hydroxide coverage at the surface, which consequence is a decrease in the corrosion current. This explanation is supported by the EIS measurements. For all magnesium specimens, OCP was lower than E_{corr} measured by LSV, and R_{p} measured at OCP by EIS was much lower than the respective R_{p} measured at E_{corr} in LSV experiments (Table 7.4). What is more, R_{p} measured at OCP changed with the SMAT duration in the opposite direction (${R_p}_{\mathrm{EIS}}^{0} > {R_p}_{\mathrm{EIS}}^{60} > {R_p}_{\mathrm{EIS}}^{120}$)

in comparison to R_p measured at E_{corr}, although the differences between R_p values measured by EIS at OCP were rather small.

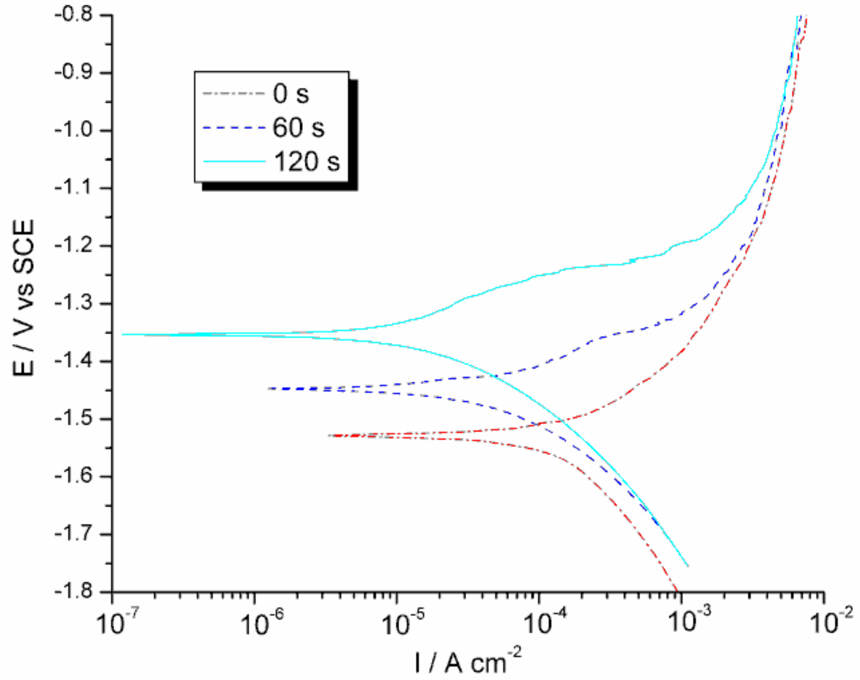

Figure 7.20 Linear sweep voltammetry on the Mg sample not subjected to any treatment (reference sample), the samples SMATed for 60 s and 120 s in 0.15 mol dm^{-3} NaCl solution saturated with $Mg(OH)_2$ at the potential sweep rate of 1 mV s^{-1} (adapted from [32]).

SMAT influences the behavior of magnesium during corrosion tests. The SMATed magnesium is more reactive in comparison to the reference sample. This in turn promotes the creation of the oxidation layer at its surface, which leads to apparent better corrosion resistance. This is supported by the results of the VEP measurements. The positron beam measurements showed that SMATed magnesium is more susceptible to aerial oxidation. However, it should be noted that a stagnant NaCl solution saturated with $Mg(OH)_2$ was used in the corrosion tests. This solution facilitates the precipitation of magnesium hydroxide at the surface of immersed magnesium. The hypothesis of increased reactivity of SMATed magnesium is also supported by the explanation of the influence of SPD methods on the corrosion resistance of metals given in the paper of Ralston et al. [75]. Those authors stated that the most important factor that influences the corrosion behavior of metal is the density of grain boundaries at the surface, which influences the activity of the metal in the process of anodic oxidation. However results obtained by PAS, XRD and EBSD images suggest that not only grain/subgrain boundaries at the surface but also other crystal defects, like dislocations, and vacancies play a significant role in the corrosion behavior of magnesium. For both samples SMATed for 60 s and 120 s, the XRD analysis gave almost the same size of crystallites and only a small difference in the lattice strain. The lattice strain can be related to all lattice defect density, which is reflected in PAS results. A much greater number of dislocations was introduced to the sample SMATed for 120 s than the one treated for 60 s. At the same time, the differences in the behavior of Mg specimens during electrochemical tests were observed.

It is well known that contamination with attrition media material, especially with Fe, during SMAT can affect the behavior of treated material during electrochemical tests. For example, Jiang et al. reported an increased corrosion rate of zirconium due to contamination with Fe and Cr during SMAT [76]. Another example is an increase in the corrosion rate of pure Mg after SMAT which was attributed to contamination with nanoscale embedded Fe wear debris originating from steel balls, as well as the steel chamber used to perform SMAT [34]. The SEM-EDS analysis does not reveal the presence of iron on the surfaces of the sample SMATed for 120 s and the reference one. Hence, the corrosion measurements were not affected by the eventual Fe contamination that may originate from the attrition media used or the SMAT chamber.

Table 7.4 Results of the electrochemical experiments carried out on Mg samples subjected to SMAT duration 0, 60, and 120 s in 0.15 mol dm^{-3} NaCl solution saturated with $Mg(OH)_2$: open circuit potential (OCP) after 2 h, corrosion potential (E_{corr}), the difference between OCP and E_{corr}, polarization resistance at the corrosion potential (R_p), corrosion current density (I_{corr}) obtained by the extrapolation of the cathodic branch of polarization curve in the semi-logarithmic coordinates to E_{corr}, product of I_{corr} and R_p, and polarization resistance measured by electrochemical impedance spectroscopy at OCP.

time [s]	OCP [V]	E_{corr} [V]	E_{corr}–OCP [V]	$R_{p,LSV}$ [Ωcm^2]	j_{corr} [Acm^{-2}]	$R_p \times$jcorr [V]	$R_{p,}$EIS [Ωcm^2]
0	–1.601	–1.528	0.073	173	1.32×10^{-04}	0.0228	59
60	–1.586	–1.448	0.138	636	5.00×10^{-05}	0.0318	46
120	–1.576	–1.354	0.222	1612	2.03×10^{-05}	0.0327	34

Summary

There have been investigated the surface and the deformed layer created by SMAT in pure magnesium with different parameters of the process. Magnesium was treated for 60 s and 120 s, with vibration amplitudes 13 ± 2 µm and 27 ± 2 µm, respectively. Attrition treatment led to an increase in surface roughness of Mg specimens.

Processing with the SMAT increased the roughness parameter R_a from about 1 μm for the reference sample to 3.37 μm and 4.63 μm for 60 s and 120 s of SMAT duration, respectively. The performed SEM-EDS analysis did not show the presence of iron contamination on the surfaces of the specimens.

Polarized light microscopy, EBSD, and XRD techniques revealed a gradient microstructure within the deformed surface layer of the SMATed magnesium. The visible SMAT affected layer extends to the depth of about 800-900 μm for both SMAT duration times. A significant decrease in the grain size close to the surface for the sample SMATed for 120 s and the gradually decreasing density of characteristic twins belonging to different twinning systems with increasing distance from the treated surface for both samples were observed. This result corresponds well with the thickness of the SMAT affected layers determined by microhardness tests and PAS.

The absence of residual stresses near the surfaces of the SMATed Mg specimens corresponds well with the microstructure observation made by the use of the EBSD method. The obtained values of residual stress in SMATed magnesium, due to its low melting point, were attributed to their ease of recrystallization. SMAT induced heat effects resulted in the local recrystallization of highly deformed grains leading to the formation of small grains. Those grains were only visible for specimen SMATed for 120 s and were present only near the surface. It indicated that the thermal effect of SMAT is weaker than the strengthening one and that 60 s treatment with the lower vibration amplitude is not sufficient to induce both of them strongly. This explanation was confirmed by the results of the microhardness measurements. The obtained values of microhardness near the surfaces of the SMATed Mg specimens show that doubling both the amplitude and the SMAT duration results in the creation of a harder layer.

PAS measurements revealed the presence of the plastically deformed region rich in crystal lattice defects near the SMATed surfaces. It was indicated by the high values of the mean positron lifetime equal to 240 ± 1 ps for the samples SMATed for 60 s with the vibration amplitude of 13 ± 2 μm and 244 ± 1 ps for the sample SMATed for 120 s with the vibration amplitude of 27 ± 2 μm. These positron lifetimes are much longer than the value for the reference sample which is about 225 ps. Extension of positron lifetimes points out the trapping of positrons in vacancies associated with dislocations and dislocation jogs. A plateau of the high mean positron lifetime values near the surface was visible for the sample SMATed for 120 s. The longer processing time and the higher energy imparted to the sample surface during longer SMAT caused the appearance of the plateau. The plateau of the high mean positron lifetime values extended to the depth which coincides with the thickness of the highly deformed layer, i.e., about 200 μm. Such plateau was not observed for the shorter SMAT duration with the lower vibration amplitude. The obtained depth profiles of the mean positron lifetime reflect the defect concentration profiles. The decrease of the mean positron lifetime with the depth corresponds with the decreasing density of twins.

The SMAT process strongly influenced the behavior of the magnesium samples during electrochemical corrosion tests. The structure changes induced by SMAT increased the susceptibility of magnesium to anodic oxidation, leading to the enhanced formation of hydroxide coverage at the surface and, as a consequence, leading to apparent better corrosion resistance. This is confirmed by the VEP measurements which indicate a thicker oxide layer formation on the surface of the sample SMATed for 120 s. Taking into account PAS results, this demonstrates that not only grain/subgrain boundaries at the surface but also other crystal defects, like dislocations, and vacancies, may also play a significant role in corrosion behavior.

References

1. M. de Assumpção Pereira-da-Silva, F.A. Ferri, Scanning Electron Microscopy, in A.L. Da Róz, M. Ferreira, F. de Lima Leite, O.N. Oliveira (eds.): Micro and Nano Technologies, Nanocharacterization Techniques, William Andrew Publishing, 2017,1.
2. P. Scherrer, Nachr. Goettinger Gesell., Zsigmondy's Kolloidchemie, 3rd Ed. 1918.
3. B. E. Warren, X-ray diffraction, Dover Publ. Inc., USA, New York, 1969
4. F.J. Humphreys, M. Hatherly, Recrystallization and related annealing phenomena. 2nd ed. Pergamon, UK, Oxford, 2004.
5. T. Ungar, G. Tichy, J. Gubicza, et al. Powder Diffr. 20 (2005) 366.
6. G.K. Williamson, W.H. Hall, Acta Metall. 1 (1953) 22.
7. I.C. Noyan, J.B. Cohen, Residual Streess-Measurement by Diffraction and Interpretation, Springer-Verlag, Germany, Berlin, 1987
8. U. Welzel, J. Ligot, P. Lamparter, et al. J. Appl. Crystallogr. 38 (2005) 1.
9. M. Marciszko, A. Baczmański, K Wierzbanowski, et al. Appl. Surf. Sci. 266 (2013) 256.
10. M. Marciszko, A. Baczmanski, C. Braham ,et al. J. Appl. Cryst. 2016, 49 (2016) 85.
11. N. Zazi, A. Bouabdallah, O. Aaboubi, et al. J. Solid. State Electrochem. 14 (2010) 1705.
12. M. Marciszko-Wiąckowska, A. Oponowicz, A. Baczmański, et al. J. Appl. Cryst. 52 (2019) 1409.
13. D. Leeb, NDT International 12 (1979) 274.
14. F. Knoop, C.G. Peters, W.B. Emerson, J. Res. Natl. Bur. Stand. (U. S.) 23 (1939) 39.
15. F. Wredenberg, P.L. Larsson, Wear. 266 (2009) 76.
16. J. Kansy, Nucl. Instrum. Methods Phys. Res. A 374 (1996) 235.
17. A. Sidorin, I. Meshkov, E. Akhmanova, et al. Mater. Sci. Forum, 733 (2013) 291.
18. T. Balusamy, S. Kumar, T.S.N. Sankara Narayanan, Corros. Sci. 52 (2010) 3826.
19. T. Grosdidier, M. Novelli, Mater. Trans. 60 (2019) 1344.
20. M. Novelli, P. BocherP. T. Grosdidier, Mater. Charact. 139 (2018) 197.
21. M. Laleh, F. Kargar, J. Alloy Compd. 509 (2011) 91509156.

22. N. Li, Y.D. Li, Y.X. Li, et al. Mater. Sci. Eng. C 35 (2014) 314.
23. F. Kargar, M. Laleh, T. Shahrabi, et al. Mater. Sci. 37 (2014) 1087
24. J. BadreddineJ. M. Micoulaut, E. Rouhaud, et al. Granul. Matter 2 15 (2013) 367.
25. H. Chen, J. Yang, H. Zhou, et al. Met. Mater. Trans. A 48 (2017) 3961.
26. H.Q. Sun, Y.N. Shi, M.-X. Zhang, et al. Surf. Coat. Tech. 202 (2008) 3947.
27. Y.H. Wei, B.S. Liu, L.-F. Hou, et al. J. Alloy Compd. 452 (2008) 336.
28. K.Y. Zhu, A. Vassel, F. Brisset, et al. Acta Mater. 52 (2004) 4101.
29. C.H. Caceres, P.L. Blake, Philos. Mag. 88 (2009) 991.
30. R. Ichikawa, J. Jpn. I. Met. 20 (1956) 93.
31. S. Rouquette, E. Rouhaud, M. François, et al. J. Mater. Process. Technol. 209 (2009) 3879.
32. K. Skowron, E. Dryzek, M. Wróbel, et al. Materials 13 (2020) 4002.
33. Y. Liu, B. Jin, D.-J. Li, et al. Surf. Coat. Technol. 261 (2015) 219.
34. D. Fabijanic, A. Taylor, K.D. Ralson, et al. Corrosion 69 (2013) 527
35. S. Bagherifard, D.J. Hickey, S. Fintová, et al Acta Biomater. 66 (2018) 93.
36. R. Wawszczak, A. Baczmański, M. Marciszko, et al. Mater. Charact. 112 (2016) 238.
37. F.J. Humphreys, M. Hatherly, Recrystallization and Related Annealing Phenomena, Elsevier Science Ltd., UK, Oxford, 1995.
38. S.B. Fard, M. Guagliano, Frat. Ed Integrità Strutt. 7 2009, 3.
39. D. Gallitelli, D. Retraint, E. Rouhaud, Adv Mat Res. 2014, 996 (2014) 964.
40. V. Optasanu, AT. Kanjer, T. Montesin, Influence of shot-peening on the high temperature oxidation of Zr and Ti plates, High Temperature Corrosion, in T.S. Sudersham, M.A.J. Somers (eds): Twenty Ninth International Conference on Surface Modification Technologies, Kongens Lyngby, Denmark 10-12 June 2015, Curran Associates, Inc.: Morehouse, USA, 2016, 29-37.
41. L. Raceanu, V. Optasanu, T. Montesin, et al. Oxid. Met., 79 (2013) 135.
42. T. Grosdidier, M. Novelli, Mater. Trans. 60 (2019) 1344.
43. J. Peng, Z. Zhang, P. Guo, et al. Mater. Charact., 148 (2019) 26.
44. H. Chen, J. Yang, H. Zhou, et al. Met. Mater. Trans. A 48 (2017) 396.
45. Y. Liu, B. Jin, D.-J. Li, et al. Surf. Coat. Technol. 261 (2015) 219.
46. P. Hautojärvi, J. Johansson, A. Vehanen, et al. Appl. Phys. A 27 (1982) 49.
47. J. Río, C. Gómez, M. Ruano, Philos. Mag. 92 (2012) 535.
48. H.Q. Sun, Y.-N. Shi, M.-X. Zhang, et al. Acta Mater. 55 (2007) 975.
49. X. Meng, M. Duan, L. Luo. et al. Mater. Sci. Eng. A 707 (2017) 636.
50. H. Okhubo, Z. Tang, Y. NagaiY. et al. Mater. Sci. Eng. A 350 (2003) 95.
51. J. Dryzek, E. Dryzek, T. Suzuki, et al. Tribol. Let. 20 (2005) 9.
52. J. Dryzek, Appl. Phys. A 114 (2014) 465.
53. J. Dryzek, Tribol. Int. 131 (2019) 268.
54. A. Serra, N. de Diego, Phys. Status Solidi A 110 (1988) 409.
55. P. Folegati, A. Dupasquier, R. Ferragut, et al. Phys. Status Solidi C 4 (2007) 3493.
56. J. Čížek, I. Procházka,; B. Smola, et al. Mater. Sci. Forum 584-586 (2008) 591.
57. R. Krause-Rehberg, V. Bondarenko, E. Thiele, R. Klemm, N. Schell, Nucl. Instrum. Methods Phys. Res. B 240 (2005) 719.
58. J. Dryzek, P. Horodek, Nucl. Instrum. Methods Phys. Res. B 266 (2008) 4000.
59. K.R. Hebert, T. Gessmann, K.G. Lynn, et al. J. Electrochem. Soc. 151 (2004) 22.
60. Y.C. Wu, T. Zhai, P.G. Coleman, Metall. Mater. Trans. A 43 (2011) 2823.
61. W. Yang, Z.J. Zhu, J.J. Wang, et al. Corros. Sci. 106 (2016) 271.
62. J. Dryzek, H. Schut, E. Dryzek, Phys. Status Solidi C 4 (2007) 3522.
63. K.R. Hebert, T. Gessmann, K.G. Lynn, et al. J. Electrochem. Soc. 151 (2004) 22.

64. Y.C. Wu, T. Zhai, P.G. Coleman, Metall. Mater. Trans. A 43 (2011) 2823.
65. A. Van Veen, H. Schut, M. Clement, et al. Appl. Surf. Sci. 85 (1995) 216.
66. S.W.H. Eijt, R. Kind, S. Singh, et al. J. Appl. Phys. 105 (2009) 043514.
67. P. Hruška, J. Čížek, W. Anwand, et al J. Phys.: Conf. Ser.505 (2014) 012024.
68. W. Yang, Z.J. Zhu, J.J. Wang, et al. Corros. Sci. 106 (2016) 271.
69. M.J. Puska, R.M. Nieminen, Rev. Mod. Phys. 66 (1994) 841.
70. M. Clement, J.M.M. de Nijs, P. Balk, et al. J. Appl.Phys. 79 (1996) 9029.
71. W. Yang, Z.J. Zhu, J.J. Wang, et al. Corros. Sci.106 (2016) 271.
72. Z. Qiao, Z. Shi, N. Hort, et al. Corros. Sci. 61 (2012) 185.
73. Z. Shi, F. Cao, G. Song, et al. Corros. Sci. 88 2014 434.
74. C. op’t Hoog, N. Birbilis, Y. Estrin, Adv. Eng. Mater. 10 (2008) 579.
75. K.D. Ralston, N. Birbilis, C.H.J. Davies, Scr. Mater. 63 (2010) 1201.
76. P. Jiang, Q. Wei, Y.S. Hong, et al. Surf. Coat. Technol. 202 (2007) 583.

Chapter 8: Studies of laser shock peened 316L stainless steel

The following Chapter presents the results of studies of AISI 316L stainless steel subjected to LSP. The technique was used to generate a gradient microstructure inside steel specimens. PALS, VEP beam measurements, and XRD techniques were used to study changes in the microstructure of the treated steel.

8.1 Sample preparation

The polished samples of AISI 316L stainless steel were annealed for 1 hour at 1000 °C in the flow of nitrogen. The LSP was carried out on the sample surface (covered with 50 μm thick layer of black paint) in the point grid (0.64 × 0.64 mm^2) using the Q-switched Nd:YAG laser system operating with the following parameters: wavelength: 1064 nm, frequency: 10 Hz, pulse length: 10 ns, energy: 0.55 J, spot diameter: 2.7 mm. A schematic illustration of the LSP procedure is shown in Fig. 8.1.

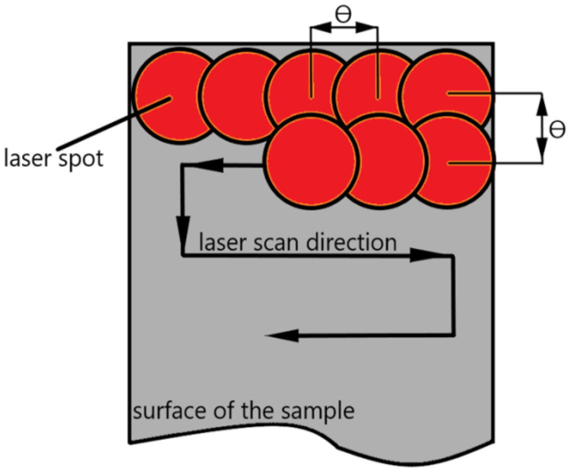

Figure 8.1 Schematic illustration of LSP procedure; θ = 0.64 mm.

8.2 Methods

8.2.1 X-ray Diffraction measurements

The XRD patterns were registered using X'Pert PRO Materials Research Diffractometer by PANalytical. The Cu Kα radiation was used at the Bragg-Brentano geometry over the 2θ range of 20-120°, step 0.02°, at room temperature. The HighScore Plus v.305 software by PANalytical B.V was used for the XRD pattern analysis.

8.2.2 Positron annihilation spectroscopy

To obtain the depth profiles of positron annihilation characteristics, the LSP treated samples were sequentially etched in glyceregia etchant and PALS measurements were carried out. The procedure was similar to that described in Chapter 6.

The PALS measurements were performed with the ^{22}Na isotope using the fast-fast spectrometer based on BaF_2 scintillators with a time resolution of 260 ps. The analysis of the obtained spectra with more than 10^6 counts was made with the LT program.

To investigate the 1 μm thick layer close to the LSP treated surface the VEP beam was used. The positrons were formed into a mono-energetic beam with an intensity of about 10^5 e^+/s and a diameter of 5 mm. The energy of implanted positrons ranged from 0.01 to 32 keV. DB spectra were measured at room temperature using HPGe detector with 1.1 keV energy resolution at 511 keV.

8.3 Results and discussion

The XRD method was used to determine the effect of LSP on the internal microstructure of the topmost layer of the samples. Fig. 8.2 shows X-ray patterns of 316L samples. For both reference and LSP specimens, there are visible clear peaks from austenite (γ) in the XRD patterns. Additional small peaks of deformation-induced martensite (α’) are visible for the LSP sample. To calculate the average crystallite size, the W-H method was used. LSP significantly reduces the size of the crystallites from 2735 ± 194 nm for the reference sample to 24 ± 13 nm for the LSP sample.

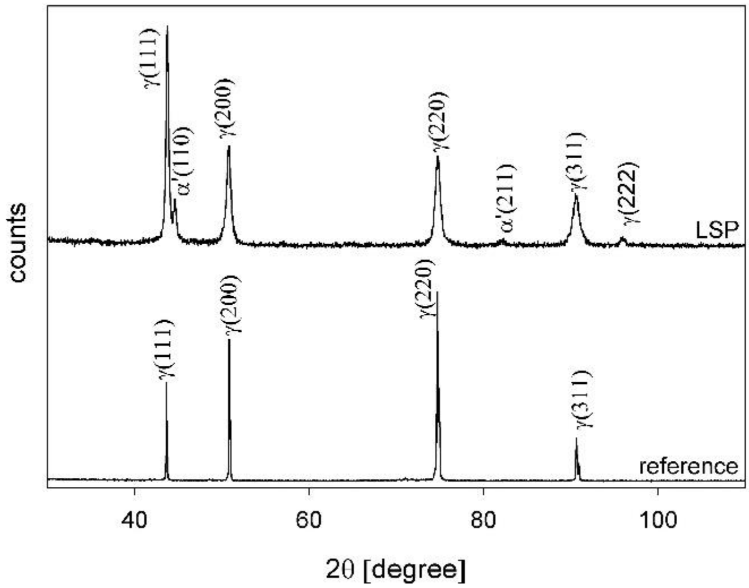

Figure 8.2 X-ray patterns of 316L samples [1].

A formation of similar in size crystallites in LSP-treated steel samples was reported by Zhou et al [1]. They found that a layer of isometric crystallites with sizes ranging from 50–300 nm were formed on the surface of stainless steel. There are a relatively large number of papers reporting the grain refinement and martensite transformation, mainly in 304 stainless steels during severe plastic deformation [3-5]. According to Lu et al., the high strain rate plastic deformation resulting from LSP leads to the generation of dislocation lines and their tangles, dislocation walls, and mechanical twinning in the original coarse-grained structure of steel [6]. Due to dynamic recrystallization that occurs in the top-most layer of steel during the LSP process, the dislocation structure is transformed into subgrain boundaries which finally build nanoscale grains. Chen et al. ascribed the process of nanocrystallization of stainless steels during SPD to dislocation motions and martensite transformations [7].

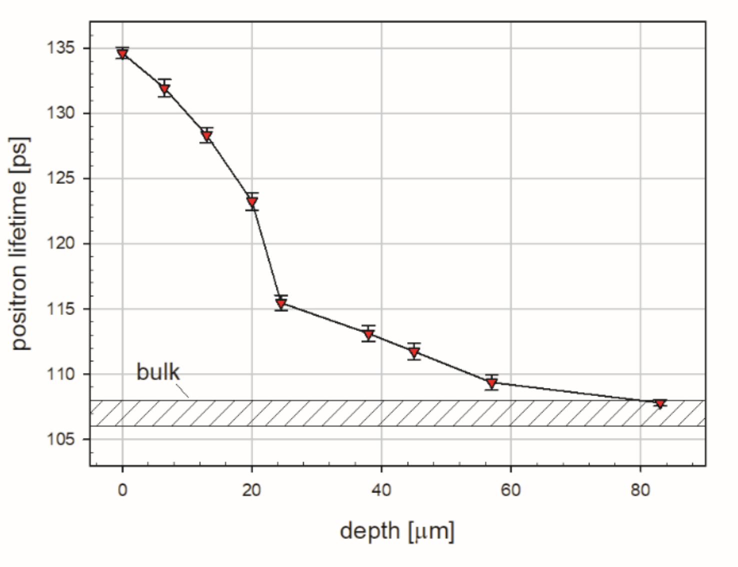

Figure 8.3 Mean positron lifetime profile. The solid line is a guide for an eye [1].

Fig. 8.3 presents the mean positron lifetime dependencies on the depth from the LSP surface of the steel sample. The value of the positron lifetime measured for the well-annealed reference sample is equal to $\tau_{bulk} = 107 \pm 1$ ps. The obtained value for the bulk sample is in good agreement with values for defect-free pure Fe [8]. The value of the mean positron lifetime measured on the surface of the LSP specimen is equal to 135 ± 1 ps. The mean positron lifetime decreases steeply to the depth of about 25 μm starting just below the surface. Then the more gradual decrease in its values is visible to the depth of about 80 μm where it finally reaches the value for the well-annealed sample. Hence, the depth of 80 μm can be considered as the total depth of the LSP-induced changes. This is much shorter than the range observed, e.g., for cutting [9]. Two positron lifetimes were resolved in the measured positron lifetime spectra up to the depth of about 13 μm, as can be seen in Fig. 8.4. Both components are longer than the reference bulk lifetime value. The first lifetime τ_1 can be attributed to positron trapping by dislocations. The second lifetime (τ_2 = 240 ÷ 300 ps) indicates the presence of clusters that consist of two to five vacancies [10,11]. For the depth larger than 13 μm only one component in the spectra was resolved.

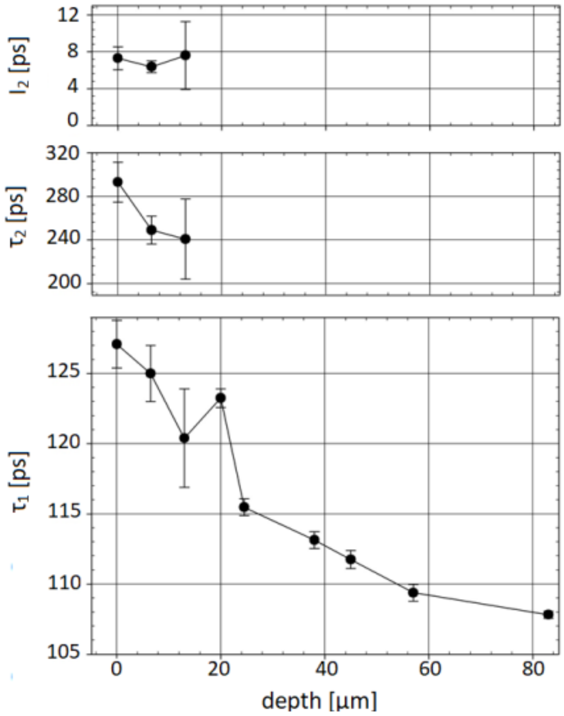

Figure 8.4 Positron lifetime components τ_1 and τ_2 and intensity I_2 of the longer component versus depth [1].

The values of the S- and W-parameter versus the energy of the incident positrons, obtained using VEP are presented in Fig. 8.5. The top horizontal axis denotes the mean implantation depth of the annihilating positrons calculated using the formula: $\bar{z}[nm] = 1.4E^{1.757}$, where E is the positron incident energy in keV. The S-parameter decreases with the increase in positrons energy and then saturates. The level of saturation is higher for the LSP sample which points out a higher concentration of defects in comparison to the reference sample. In the case of the reference sample, saturation is achieved at higher energies than for the LSP sample. Solid lines visible in Fig. 8.5 are the result of the VEPFIT code fitting of the model function. The obtained positron diffusion length equals $L_{+\mathrm{ref}}$ = 84 ± 2 nm for the reference sample and L_+ = 60 ± 1 nm for the LSP sample, which is in good agreement with the values presented in the literature [12]. The shortening of the positron diffusion length indicates the presence of crystal lattice defects. In general, the effective positron diffusion length can be described by the formula:

$$L_{+eff} = \sqrt{\frac{D_+}{\lambda_b + \kappa_i}}, \tag{8.1}$$

where D_+ is the positron diffusion coefficient, λ is the annihilation rate and κ is the trapping rate for open volume defects, $\kappa_i = n_i \nu_i$, where ν_I is the specific trapping rate of positrons for a certain defect i and n_i is the defect concentration. The presence of open volume defects causes shortening of the effective diffusion length. It is worth mentioning that, the positron diffusion coefficient can also influence L_{+eff} . For example, the presence of interstitials can reduce the D_+ value and hence L_{+eff}. Considering self-interstitials in metals, it should be noted that their equilibrium concentration is very low at room temperature and can be neglected. Therefore it can be expected that the observed shortening of the effective positron diffusion length is caused by the presence of open volume defects which is confirmed by the results of positron lifetime measurements.

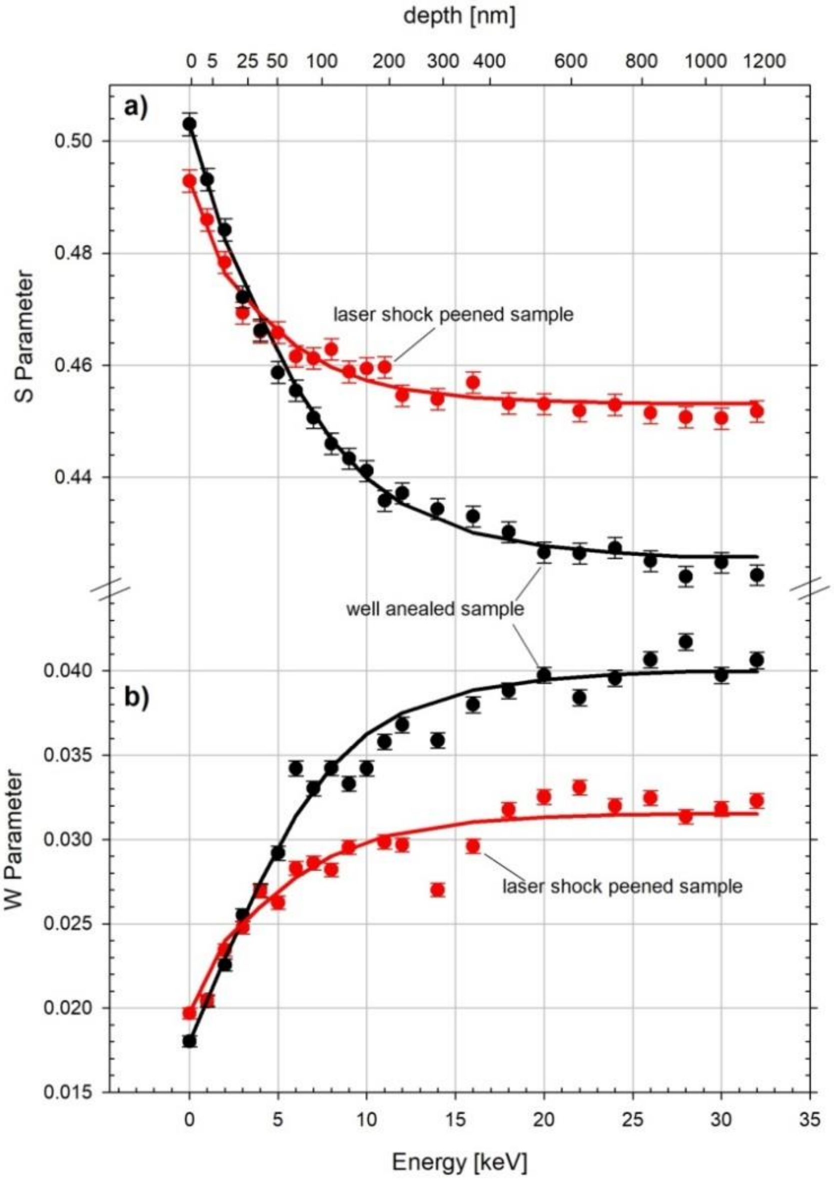

Figure 8.5 a) The S-parameter as a function of the incident positron energy (as well as its implantation range - upper horizontal axis), b) The W-parameter as a function of the incident positron energy. Solid lines represent the best fit using VEPFIT [1].

Assuming that all positrons are trapped mainly in dislocations and their density is constant in the probed volume, it is possible to relate positron diffusion length L_+ obtained from VEP measurements with dislocation density ρ_d using the formula [14]:

$$\rho_d = \frac{1}{\mu\tau_{\mathrm{bulk}}}\left(\left(\frac{L_{+\mathrm{ref}}}{L_+}\right)^2 - 1\right), \tag{8.2}$$

where μ is the specific trapping rate of positrons in dislocations, τ_{bulk} is positron lifetime in bulk material, $L_{+\mathrm{ref}}$ and L_+ are positron diffusion lengths in reference and LSP samples respectively. Assuming that, the value of μ is equal to 0.51×10^{-4} m^2/s [13] which is a value determined for iron, the approximated dislocation density for the LSP sample is of the order of 10^{14} m^{-2}.

Summary

PALS measurements make it possible to determine the depth of LSP-induced changes in AISI 316L steel, which extends to the depth of about 80 μm. Near the surface, at a depth less than 13 μm, clusters consisting of two to five vacancies are formed during the LSP process. The dislocation density near the LSP treated surface at a depth less than 1 μm estimated from the VEP results is of the order of 10^{14} m^{-2}.

The W-H method was used to determine the average crystallite size in reference and LSP specimens. LSP significantly reduces the size of the crystallites from 2735 ± 194 nm for the reference sample to 24 ± 13 nm for the LSP sample. XRD analysis reveals deformation-induced martensite in the LSP steel.

References

1. K. Skowron, E. Dryzek, M. Wróbel, et al. Acta Phys. Pol. B 51 (2020) 317.
2. L. Zhou, W. He, S. Luo, et al. J. Alloys Compd. 655 (2016) 66.
3. B.N. Mordyuk, Yu.V. Milman, M.O. Iefimov, G.I. Prokopenko, et al. Surf. Coat. Technol. 202 (2008) 4875.
4. C.X. Huang, G. Yang, Y.L. Gao, et al. J. Mater. Res. 22 (2007) 724.
5. H.W Zhang, Z.K Hei, G Liu, et al. Acta Materialia 51 (2003) 1871.
6. J.Z. Lu, K.Y. Luo, Y.K. Zhang, et al. Acta Materialia 58 (2010) 5354.
7. A.Y. Chen, H.H. Ruan, J. Wang, et al, Acta Materialia 59 (2011) 3697.
8. J.M. Campillo Robles, E. Ogando, F.J. Plazaola, J. Phys.: Condens. Matter 19 (2007) 176222.
9. P. Horodek, J. Dryzek, M. Wróbel, Tribol. Lett. 45 (2012) 341.
10. E. Kuramoto, T. Tsutsumi, K. Ueno, et al. Comput. Mater. Sci. 14 (1999) 28.
11. M. J. Puska, R. M. Nieminen, J. Phys. F: Metal Phys., 13 (1983), 333
12. Y. C. Wu, Y. C. Jean, Phys. Stat. Sol. C 4 (2010) 3506.
13. Y.K. Park, J.T. Waber, M. Meshii, et al. Phys. Rev. B 34 (1986) 823.
14. R. Krause-Rehberg, V. Bondarenko, E. Thiele, et al. Nucl. Instrum. Methods Phys. Res., Sect. B, 240 (2005) 719.

Chapter 9: Studies of Ti specimens subjected to surface mechanical attrition treatment

As it was mentioned in Chapter 1, in the last several decades, Ti-based materials have been used for a wide variety of applications in such areas as aerospace, automotive, power generation, biomedical devices, and biomedical implants. Nonetheless, the wear resistance of titanium is relatively low which limits the potential area of its application in load-bearing applications, e.g., in articulating components of total joint replacements. Mechanical and chemical properties of titanium-based materials can be improved with appropriate mechanical treatments based, e.g., on the SPD methods and among them SMAT.

This Chapter aims to characterize the microstructure of grade 2 titanium subjected to SMAT and to relate the obtained results to corrosion properties determined by electrochemical tests. PALS, XRD, EBSD, microhardness tests, and the surface profile characterization were applied to characterize the influence of SMAT on the microstructure of the Ti surface.

Noteworthy is the fact that PAS can shed light on the complicated mechanism of deformation induced by SMAT in the surface layer of titanium by providing information on crystal lattice defects created in this layer.

9.1 Sample preparation

The specimen 100 mm × 100 mm × 8.3 mm in dimensions was cut from a sheet of Ti grade 2. Before SMAT, the specimen was annealed at 400°C in a vacuum (~10^{-3} Pa) for half an hour, and then slowly cooled inside the furnace to room temperature.

SMAT was performed in the stainless steel chamber in the air at room temperature using 2 mm diameter stainless steel balls and a vibration frequency of 20 kHz. The two opposite sides of the Ti plate were treated separately for 60 s and 120 s, with vibration amplitudes 13 ± 2 μm and 27 ± 2 μm, respectively. After SMAT, the specimen was cut into smaller pieces 10 mm × 10 mm in size. For simplicity, the opposite sides of specimens from now on are referred to as 60 s and 120 s SMATed samples. Pieces of the plate, not subjected to the SMAT process, were kept as references.

9.2 Methods

The details of the apparatus used and the methodology of measurements including surface characterization with a profilometer, XRD, and microhardness tests are described in Chapter 7.

9.2.1 Positron annihilation lifetime spectroscopy

The digital positron lifetime spectrometer manufactured by TechnoAP with two photomultipliers: H3378-50 each one coupled with a single crystal of BaF_2 scintillators was used. The timing resolution (FWHM) was about 190 ps. A ^{22}NaCl-solution evaporated on a 7 μm thick Kapton foil with an activity of about 20 μCi served as the positron source. All the obtained spectra containing more than 10^6 counts were analyzed using the LT code, taking into account the source contribution and background subtraction [16].

9.2.2 Corrosion tests

Two series of measurements were performed. In the first one, the surfaces of SMATed and the reference samples were only cleansed with acetone, and then EIS measurements were performed. To facilitate the description of the results of corrosion resistance measurements in Chapter 9.3.5, these specimens are referred to as as-received ones. In the second series, Ti pieces after SMAT and the reference ones were grounded and polished to remove the presumably thick oxide layer that has grown on their surfaces. SiC papers of a grid 1000, 2000, 2400 were used. Then, the samples were further polished using paper of a grid 4000 and then cleansed with acetone. The thicknesses of abraded layers were determined by measuring the dimensions of the samples and their weight loss after the polishing process. Approximately 2 μm thick layers were abraded in each polished sample. The specimens from the second series are referred to as polished ones. Samples SMATed for 60 s and 120 s, as well as references, were measured in each of the series. At least three measurements were made for each sample.

Corrosion tests were performed in an all glass-and-PTFE (Polytetrafluoroethylene) cell in a 0.15 mol dm^{-3} NaCl solution. The composition of the solution used is close to the solutions in which Ti objects corrode in practical applications, e.g., in the human body (implants) and the land transportation, e.g., sodium chloride is spilled on the road surfaces in winter. A three-electrode corrosion testing set-up consisting of the SCE as the RE, the platinum foil as the CE, and the sample as the WE, was used. All potentials are reported versus RE. The WE with an exposed area of 0.25 cm^2 was placed at the bottom of the cell, in a horizontal position, with the active surface up to facilitate the eventual liberation of the hydrogen formed in the titanium passivation process. Before the measurements, the solution was bubbled with argon to remove dissolved oxygen. The measurements were carried out at room temperature 21 ± 1 °C. All titanium EIS measurements were preceded by a 24-hour immersion in the solution accompanied by simultaneous measurement of the OCP. EIS spectra in the frequency range of 225 μHz to 300 kHz and the amplitude of the sinusoidal voltage signal of 10 mV were registered at OCP with the density of 8 points per decade using Gamry G300 Potentiostat/Galvanostat/ZRA.

9.3 Results and discussion

9.3.1 Surface

Fig. 9.1 shows the morphology of titanium samples after 60 s, and 120 s of SMAT. SMAT resulted in the creation of numerous craters on the treated surfaces. There are clear differences between surfaces visible in Fig. 9.1 a) and b). In the case of Ti SMATed for 60 s, the surface is more or less homogeneous, with a large number of small, shallow craters created by steel shots. The surface SMATed for 120 s exhibits larger and deeper craters. The roughness parameter R_a was calculated from the areas of the specimens visible in Fig 9.1. The value of R_a for the reference sample is about 1 μm. Processing with the SMAT increased the roughness parameter to 1.65 μm and 3.07 μm for 60 s and 120 s of SMAT duration, respectively.

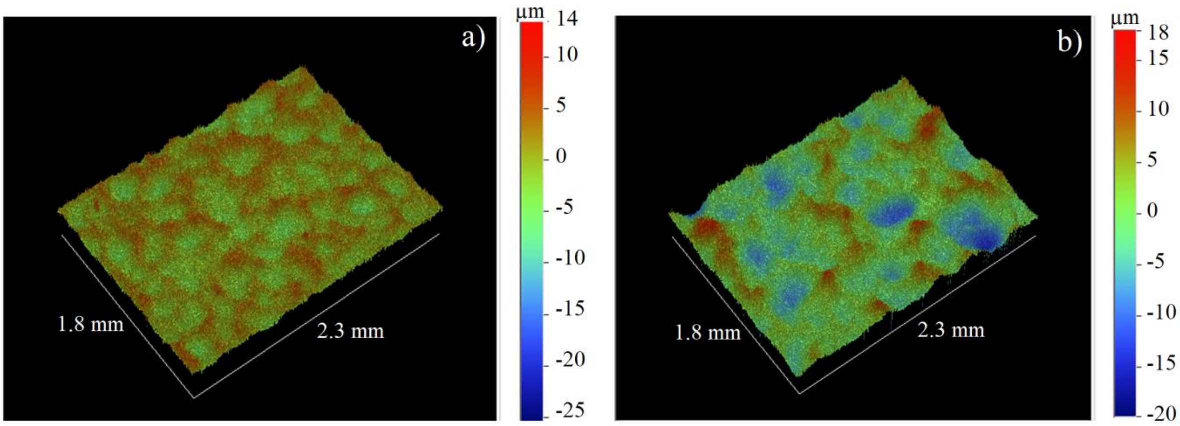

Figure 9.1 Optical profiler images of Ti specimens surface SMATed for (a) 60 s and (b) 120 s, and (c) the reference sample.

A similar value of the surface roughness to those for specimen SMATed for 120 s was obtained by Jamesh et al. in grade 2 titanium SMATed for 45 min with 8 mm alumina balls. These authors reported the change of titanium surface roughness from R_a 0.15 μm to 3.27 μm for untreated and SMATed specimens, respectively [2]. The surface of the specimen SMATed for 60 s is more homogeneous compared to the 120 s sample on which surface craters are larger and deeper. These differences in the surface finish are related to different vibration energy, i.e., higher for the sample SMATed for 120 s, rather than treatment time. The higher amplitude of the vibrating sonotrode translates to the higher kinetic energy of steel shots, which results in the creation of larger and deeper craters. This, in turn, leads to the increase of surface roughness. Similar dependencies of surface roughness on the processing parameters for pure Ti were reported by Zhu et al. [3,4]. They reported that for short SMAT durations, the increase of the peening duration increases the pit number and thus the roughness. However, further increasing of treatment time does not result in higher roughness. After the peening duration reaches a certain time, the surface roughness reaches its maximum value and the shots do not introduce plastic deformation and the surface roughness became stable. This is due to the fact that after some time of the peening, the material reaches its maximum hardness, and further processing does not introduce any new plastic deformation.

9.3.2 Microstructure

The microstructure of the SMATed titanium was observed using the EBSD technique. The image of the microstructure of cross-sectioned titanium samples is shown in Fig. 9.2. The SMATed surface is located on the bottom edge of the picture. However, it should be noted that the edge of the specimen was not visible, due to its undesirable rounding during preparation made before measurement. The EBSD scan was recorded starting at approximately 5 μm below the SMATed surface. The area rich in refined grains is visible up to the depth of about 50 μm. The inverse pole figures show that close to the surface, no significant preferred orientations of the grains were developed. Deeper, small clusters of grains were formed. These clusters are usually stretched along lines inclined concerning the treated surface and their grains have some preferred orientation to the matrix. However, determining this orientation relationship requires a more resolving research technique (TEM).

Table 9.1 Calculated values of crystallite size for Ti samples.

sample	**crystallite size [nm]**	**lattice strain [%]**
SMAT 60 s	52 ± 5	0.1(1)
SMAT 120 s	68 ± 21	0.28(4)

SMAT effect on the average crystalline size and the lattice strain was determined from XRD by the W-H method. The results are shown in Fig. 9.3 and Tab. 9.1. One can see that the lattice strains depend on the SMAT processing parameters, i.e., they are equal to 0.1(1)% and 0.28(4)% for the sample SMATed for 60 and 120 s, respectively. Although there is no significant effect on the size of crystallites. In comparison to previous results for magnesium treated in the same way, it seems that for titanium, the 60 s of SMAT induced much smaller changes in the microstrain or surface roughness than in the case of the sample SMATed for 120 s. It was reported that SMAT creates ultra-fine grains of 100-150 nm in size in cp titanium [5,6]. Similar in size crystallites, i.e., 40 nm were found by Bahl et al. in SMATed grade 2 titanium [7].

They performed SMAT using steel balls of 4.75 mm in diameter for 30 min. The crystallite sizes obtained in the present studies are also comparable with those obtained for severe shot-peened cp titanium, which size was reported to be 74 nm [8]. Similar values of lattice strain and average crystallite size induced by SMAT in pure titanium were reported by Wen et al. The average grain size calculated by them was about 43 nm, and the micro-strain was about 0.18% [9].

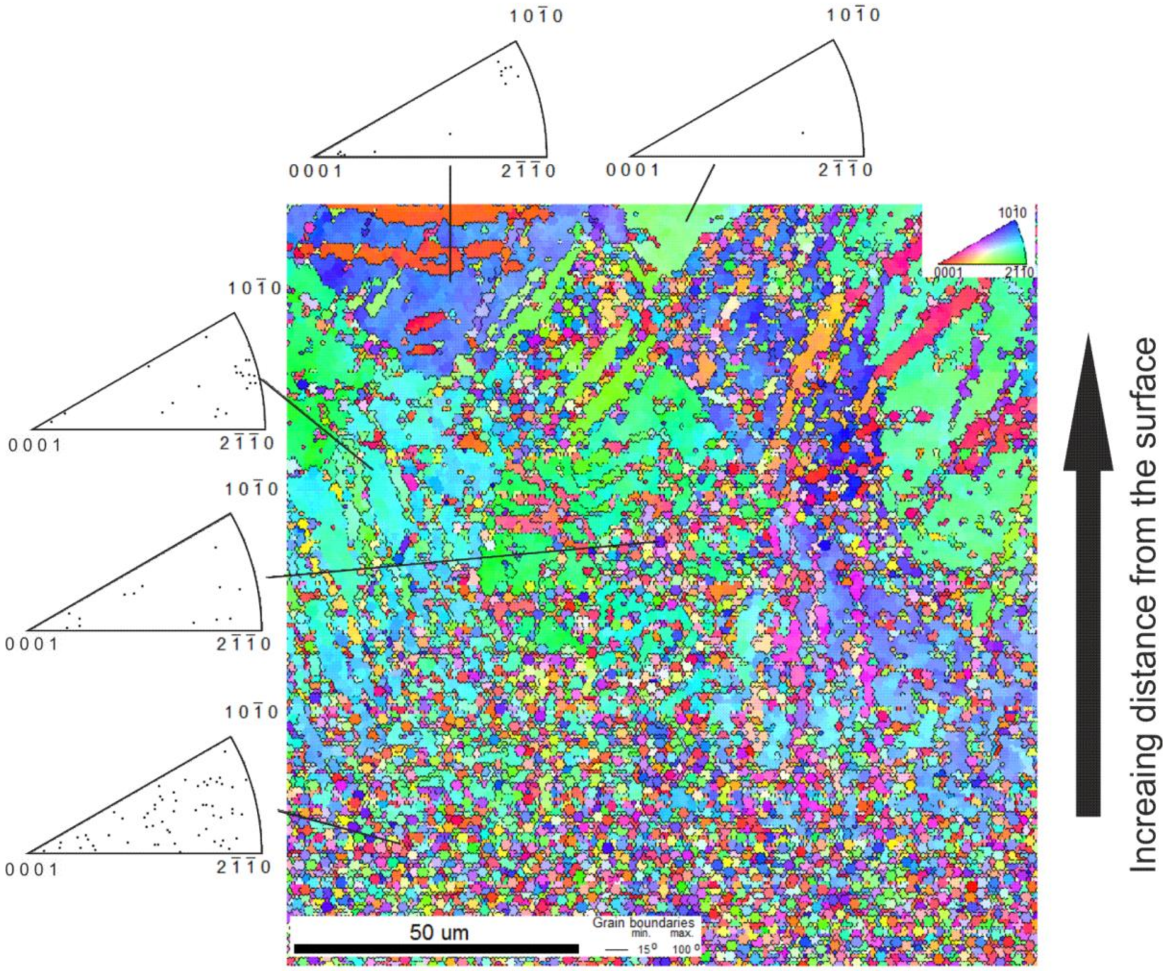

Figure 9.2 EBSD orientation mapping of the cross-section of the Ti SMATed for 120 s.

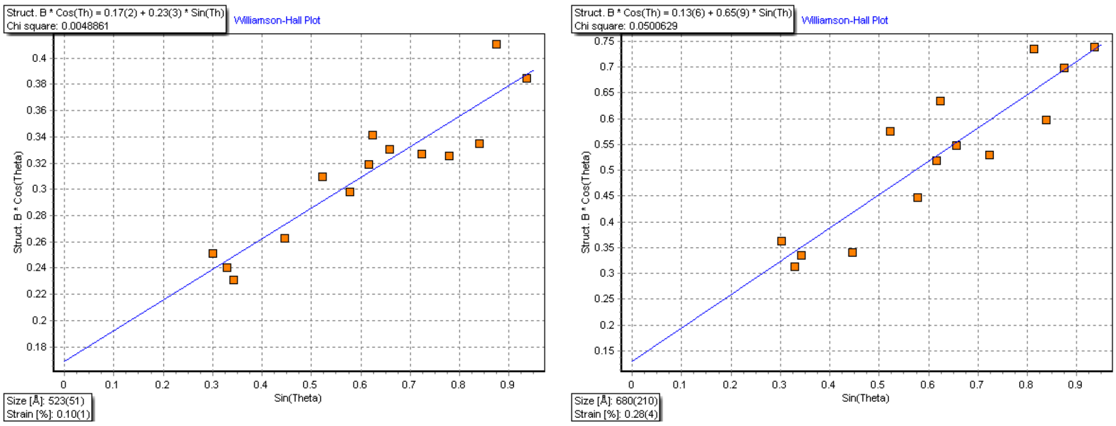

Figure 9.3 W-H analysis using PANalytical software.

9.3.3 Microhardness profile

Fig. 9.4 shows the microhardness values measured on the cross-sections of the SMATed titanium specimens. For the specimen treated for 120 s, microhardness values near the surface, i.e., at the depth of about 10 µm, is approximately 1.6 times higher than the value measured for the reference sample. The SMAT treatment did not significantly affect the hardness of the 60 s SMATed sample, i.e., approximately 1.08 increase in hardness at the depth of 10 mm was revealed. However, a clear decrease in hardness with a distance from the treated surface was visible for both samples. For the specimen SMATed for 120 s, the microhardness decreases almost linearly to the distance of about 120 µm. This corresponds to the decreasing density of small grains in Fig. 9.2. For this specimen decrease in microhardness is visible to the depth of about 200-250 mm, which may be considered as the total thickness of the SMAT hardened layer. In the case of the titanium SMATed for 60 s, a much more gradual decrease in microhardness values is visible however, due to the large spread of the measurement points, it is difficult to clearly define the total thickness of the hardened layer. The microhardness tests confirm the results of surface roughness and microstrain measurements indicating that plastic deformation of the surface layer of the sample SMATed for 60 s is much smaller than that SMATed for 120 s with higher sonotrode amplitude.

Summarizing, the lattice strain, and the microhardness dependency on depth show that SMAT resulted in the creation of the hardened, fine grain subsurface layer in titanium samples. Such grain refinement may result from dynamic recrystallization of the highly deformed material. For the sample SMATed with the higher vibration amplitude, the deformation and the resulting increase in hardness in the top-most layer of the specimen is much higher than in the sample treated shorter with a lower amplitude. It can be seen that doubling both the amplitude and the SMAT duration results in the creation of a much deeper and harder layer than in the sample treated shorter. These differences are due to the higher energy imparted into the sample surface during 120 s SMAT with higher sonotrode amplitude. A similar increase in microhardness to this observed for specimen SMATed for 120 s was reported by Zhu et al. for cp titanium [10]. They observed 1.5 times increase in microhardness values in comparison to the value measured for the reference sample. It is worth mentioning that, they processed titanium using USSP with fairly similar conditions to those applied in the present study, i.e., they treated titanium for 100 s with the sonotrode amplitude of about 32-40 μm, with 20 kHz frequency using 2 mm steel shots. These authors found that the thickness of the refined layer and its grain size are key parameters influencing the hardness of titanium. The calculated values of crystallite sizes for titanium samples that are shown in Table 9.1 can be related to the presence of small grains which are responsible for the hardening of SMATed titanium. A similar increase of hardness in comparison to the reference specimen was reported by Unal et al. for severe SP of cp titanium [8]. They reported an almost 1.6 times increase in hardness after the treatment and attributed it to the increase of dislocation density and grain refinement.

Generally, the surface hardness and the total depth of the hardened layer in pure titanium increase with the increase of both amplitude of the sonotrode and shots diameter. However, the surface hardness increases also with the increase of SMAT duration until reaching its maximum value after which hardness became stable. Such behavior of hardness was reported by, e.g., Zhu et al. [10].

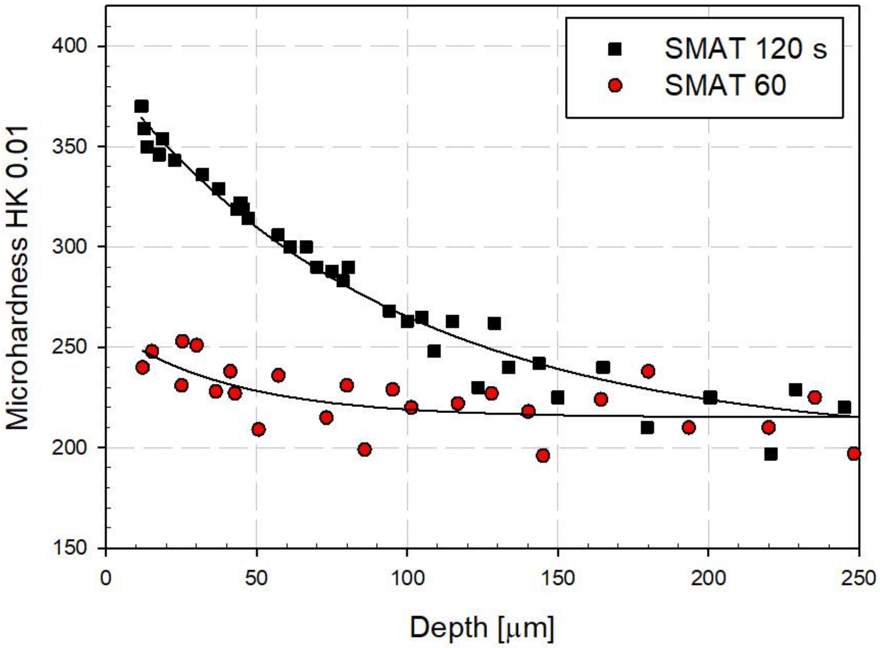

Figure 9.4. The microhardness measured on the cross-section of Ti samples SMATed for 120 and 60 s versus the distance from the surface. The solid lines are a guide for the eye.

9.3.4 Positron lifetime measurements

The implantation range of positrons emitted from ^{22}Na is much shorter than the total thickness of the SMAT affected layer whose thickness was determined in the microhardness test and observed on the EBSD map. Hence, it is possible to use a method based on the subsequent chemical etching of sample layers to obtain the annihilation characteristics, i.e., the mean positron lifetime depth profiles using a similar procedure as it was described in Chapter 6. Thin layers of samples were removed by sequential etching in Kroll's Etchant and PALS measurements were carried out. The contribution to the measured value of the positron lifetimes comes from a layer of thickness comparable to $1/\mu$. The linear absorption coefficient μ for positrons emitted from the ^{22}Na source implanted in Ti is about 222.4 cm^{-1} (Table 4.1). Therefore, the mean implantation depth of positrons is c.a. 56 μm, while the SMAT affected layer is much thicker.

Two positron lifetime components were resolved for both samples. Figure 9.4 presents the dependencies of the lifetime values of these components and the intensity of the longer component on the distance from the SMATed surface. Figure 9.5 shows the dependence of the mean positron lifetime defined as follows:

$$\bar{\tau} = I_1\tau_1 + I_2\tau_2 \tag{9.1}$$

where $I_1 + I_2 = 1$. At the surface, the mean positron lifetime takes similar values for both samples. In the case of the specimen SMATed for 60 s, the initial decrease of positron lifetime is slow up to the depth of 75 μm, then it is steeper up to 150 μm. At the depth of about 250 μm, the mean positron lifetime reaches the values for the annealed titanium which is equal to 144 ps. A similar value of the mean positron lifetime measured for bulk titanium, equal to 144.6 ps was reported by F Lukáč et al. [11]. The depth of 250 μm can be treated as the total range of defects induced by SMAT. The shape of the positron lifetime depth profile is slightly different for the sample SMATed for 120 s. After an initial decrease to the depth of about 25 μm, the mean positron lifetime increases slightly reaching a maximum at 180 μm. Then it decreases to the reference value at the depth of 400 μm, which can be considered as the total depth of SMAT induced changes. Shapes of the mean positron lifetime depth profiles shown in Fig. 9.5, in particular, in the region of its decrease, which for the sample SMATed for 120 s starts at about 200 μm, can be described by a sigmoidal function formula [17]:

$$\bar{\tau} = \tau_0 + \frac{a}{2}\left[1 + erf\left(-\frac{z - z_0}{\sqrt{2b}}\right)\right] \tag{9.2}$$

where z is the depth from the surface, and τ_0, z_0, a, and b are the adjustable parameters which values can be obtained in the fitting procedure. The z_0 parameter is the depth at which the curve reaches the transition center and a is the transition height. Tab. 9.2. gathers values of those parameters and the values of the total depth of the SMAT affected region, i.e., the depth where the reference value of the mean positron lifetime is reached (Fig. 9.5). The total depth and the z_0 parameter values increase with the SMAT time. It seems that a parameter does not depend on the SMAT time within the error range. The dashed lines in Fig. 9.5 show results of the best fit of Eq. 9.2 to the experimental points. The fitted function describes well the experimental points for the Ti SMATed for 60 s. However, in the case of sample SMATed for 120 s, there is a discrepancy in the region of a small maximum for the depth of 180 μm.

For the sample SMATed for 60 s, the shorter lifetime, τ_1, decreases rapidly from about 170 ps at the surface to the values slightly higher than the reference lifetime already at the depth of 30 μm. The longer lifetime, τ_2, takes the values close to 300 ps while its intensity, I_2, increases starting from the surface reaching a maximum of 35% at the depth of 30 μm. Then it decreases and disappears deeper than 200 μm. In the case of titanium SMATed for 120 s, to the depth of about 150 μm, τ_1 values remain close to 170 ps. Then, with increasing depth from the surface, τ_1 decreases to the values close to the reference lifetime. Near the surface, the longer lifetime, τ_2, is close to 300 ps, except exhibiting some higher values where its intensity is low, then its intensity increases reaching a maximum of 35% at about 220 μm. Then, I_2 decreases and disappears at the depth of 350 μm.

Table 9.2 The values of the adjusted parameters in Eq. (2) used for the description of the obtained depth dependencies of the mean positron lifetime depicted in Fig. 9.5.

sample	SMAT 60 s	SMAT 120 s
τ_0 [ps]	144.7 (0.7)	145.5(1.5)
a [ps]	49.3(1.4)	46.9(1.8)
z_0 [μm]	110.5(3.3)	269.1(5.0)
b [μm]	53.9(4.9)	39.8(6.9)
approximate total depth [μm]	250	400

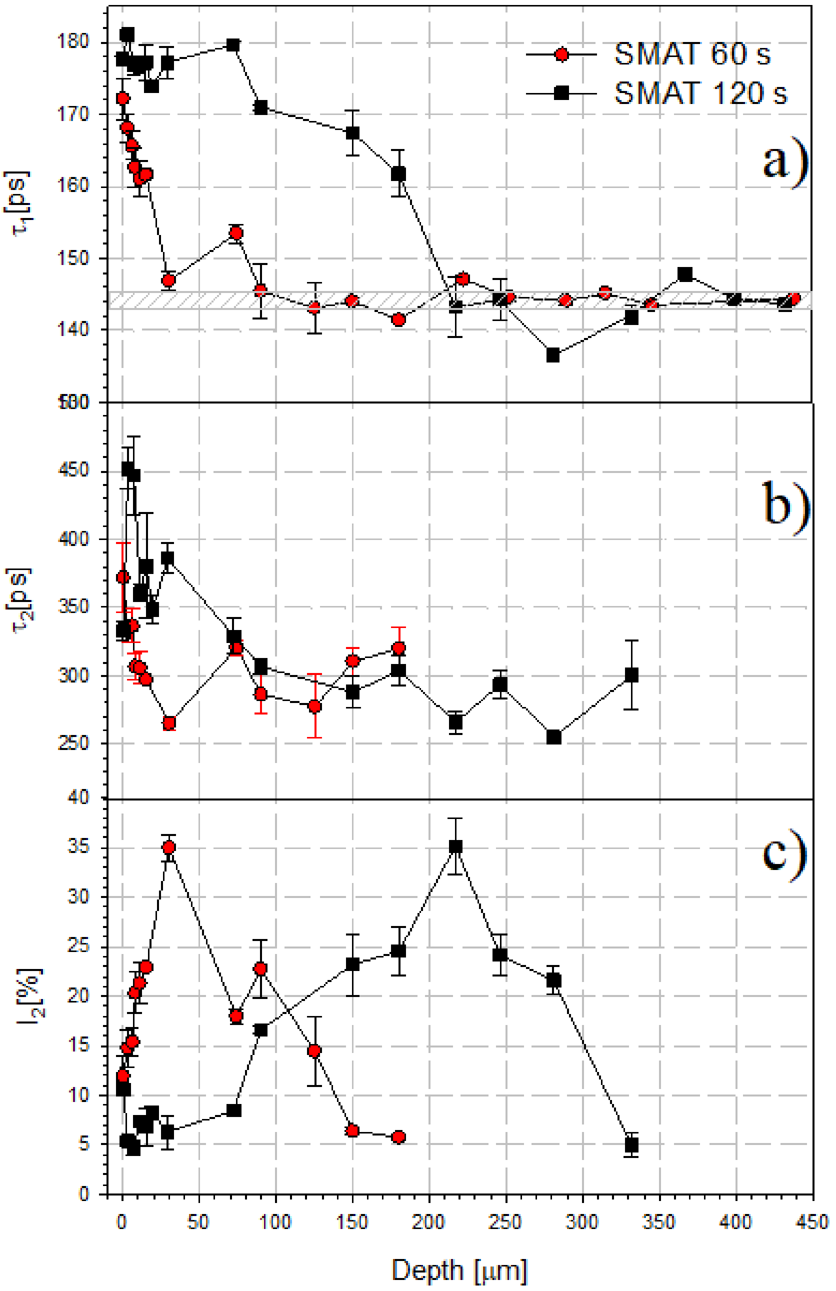

Fig. 9.4 The depth profiles of the positron lifetime components, a) τ_1, b) τ_2, and c) intensity I_2, of the longer component ($I_1 = 1 - I_2$, I_1, and I_2 are expressed in percentage in the Figures) obtained from the deconvolution of the positron lifetime spectra measured for the Ti samples SMAted for 60 and 120 s.

The first positron lifetime component, i.e., $\tau_1 \approx 170$ ps can be attributed to the annihilation of positrons trapped at dislocations [11]. The longer component, $\tau_2 \approx 300$ ps, is longer than the positron lifetime in vacancies, i. e., 222 ps reported by Kaupilla et al. [12]. The presence of such a long component indicates the trapping of positrons at vacancy clusters containing about 3 or 4 vacancies according to the theoretical calculations performed by Čížek et al, [13]. Similar values of the positron lifetime components were obtained by Lukáč et al. for pure titanium prepared by HPT [11]. The longer lifetime component equal to 280 ps, with an intensity of about 10 % was shorter than this reported in this dissertation. The shorter positron lifetime trapped in vacancy clusters was explained by those authors as caused by the lower purity of the titanium sample deformed by ECAP (Ti Grade 4). In their case, the vacancy clusters are likely coupled with interstitial oxygen atoms which reduce their open volume.

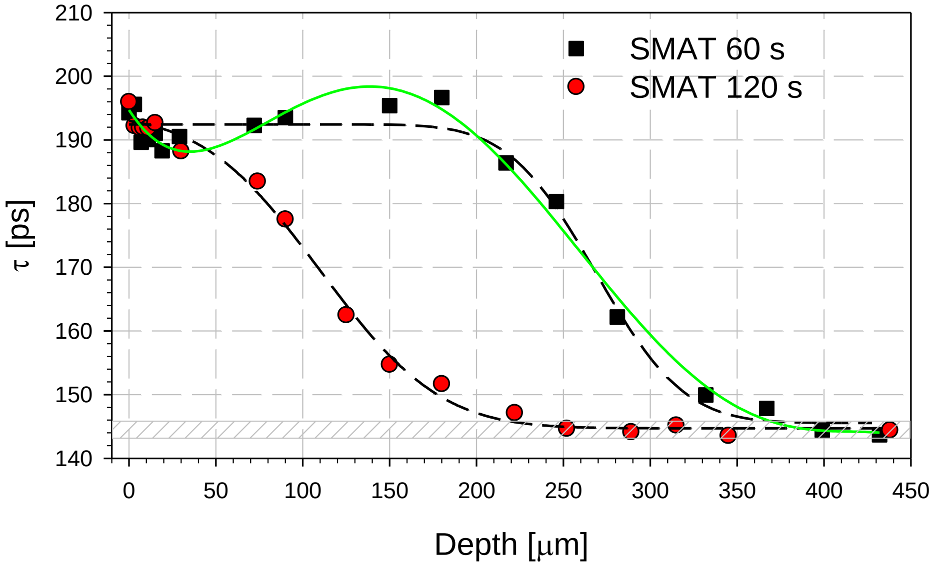

Fig. 9.5 Depth profiles of the mean positron lifetime for Ti samples SMAted for 60 s and 120 s. The dashed lines were obtained by fitting Eq. (2) to the experimental points. The solid line is a guide for the eye.

It seems that saturated trapping of positrons in dislocations and vacancy cluster occurs to the depth at which τ_1 takes the values close to 170 ps. However, the contribution of these two positron traps changes with the increasing depth from SMATed surfaces. A layer with a higher concentration of vacancy clusters is visible for both specimens and is indicated by the maximum of I_2 which occurs at the depth for which τ_1 decreases to the reference lifetime indicating a significantly reduced dislocation density. In the case of specimen SMATed for 120 s, the vacancy cluster layer is shifted deeper in comparison to specimen SMATed for 60 s. For the sample SMATed for 60 s, the layer of the higher values of τ_1 close to the surface corresponds to the layer of slightly increased microhardness. This is understandable taking into account the fact, that mainly dislocations are responsible for material hardening in this case. The influence of the vacancy clusters on microhardness is negligible. A similar situation takes place for the sample SMATed fo 120 s. The distance from the surface for which τ_1 approaches the bulk lifetime for titanium corresponds to the distance at which the microhardness decreases to the reference value.

During SMAT, the gradient microstructure forms due to a gradient variation of the strain and strain rate from the treated top surface [14]. It has been demonstrated that strain rates as high as 10^4 – 10^5 s^{-1} are developed during SMAT [14,15]. In comparison, for other SPD methods, such as HPT or ECAP strain rates are small or medium despite large strain. Hence, a good example to compare the PALS measurements results is shock-loaded titanium for which the strain rate is extremely large [16]. In the case of shock-loaded titanium, also two components were derived from the PALS spectra. The intensity of the component originating from positron annihilation in vacancy clusters is comparable with the maximum intensity obtained in the present studies, which is higher than those reported for ECAP or HPT. Nevertheless, the maximum of the intensity of the longer lifetime component is visible at some distance from the SMATed surface where the strain and strain rate are much lower than at the surface.

The obtained mean positron lifetime values for SMATed Ti are similar to those obtained by Dryzek for pure titanium subjected to dry sliding against stainless steel [17]. He reported a high value of the mean positron lifetime above 190 ps extending to some depth in the sample and a presence of a second layer where the positron lifetime decreases to the bulk values. The high intensity, i.e., 30-45% of the second component was still present at the depth at which the shorter lifetime approached the bulk values. Generally, for both SMAT and sliding friction, a gradient structure of defects is induced in the subsurface region. As it was mentioned in Chapter 7, in magnesium the sliding friction is accompanied by a large amount of plastic deformation localized within a small volume of material close to the surface, hence the common features of the defects structure of the surface layer may arise.

9.3.5 Corrosion resistance

Fig. 9.6 shows the OCP measurements for as-received and polished samples. It can be seen that the value of this potential varies during the time of measurement due to changes occurring on the surfaces of the samples, i.e., oxidation and formation of a passive layer. After a short period of immersion, the value of the potential stabilizes for all specimens.

A clear difference in the values around which potentials measured for polished and as-received samples stabilize is visible in Fig. 9.6 For the polished samples, the plateau of the potential is shifted towards negative values in comparison to the as-received ones. The surfaces of the polished samples were stripped of the oxide layer that grew during exposure to air. The surfaces of the polished samples are more reactive and titanium is oxidizing at a faster rate on their surfaces than on surfaces of as-received ones, which is reflected in the lower OCP values.

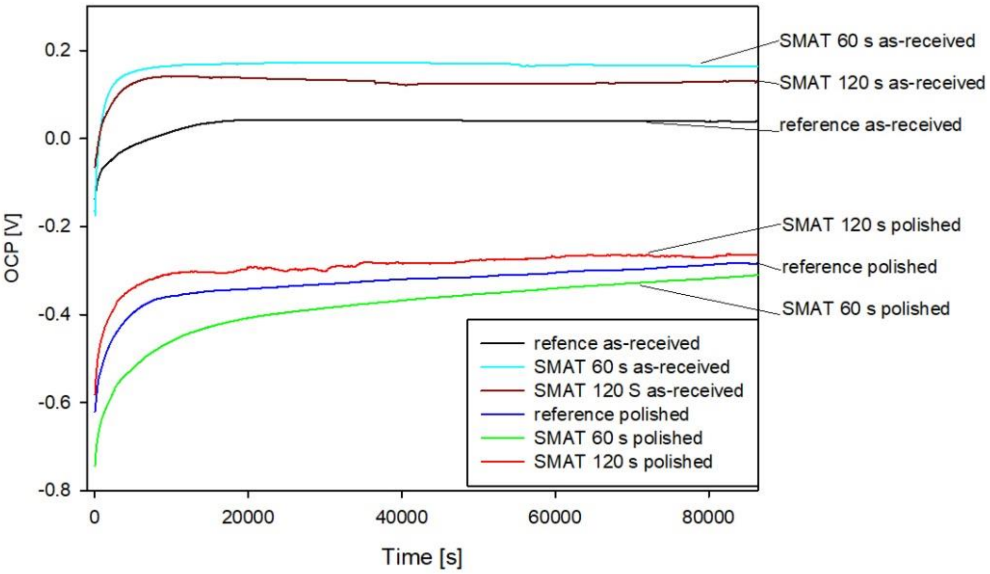

Figure 9.6 Evolution of the OCP in time.

Nyquist plots are relatively featureless. The Bode plots contain more information about the electrochemical characteristics of the system. The Bode plots of the spectra from the most representative series of measurements for the as-received samples and the polished ones are shown in Fig. 9.7 and Fig. 9.8, respectively. Three such measurements were made for each sample.

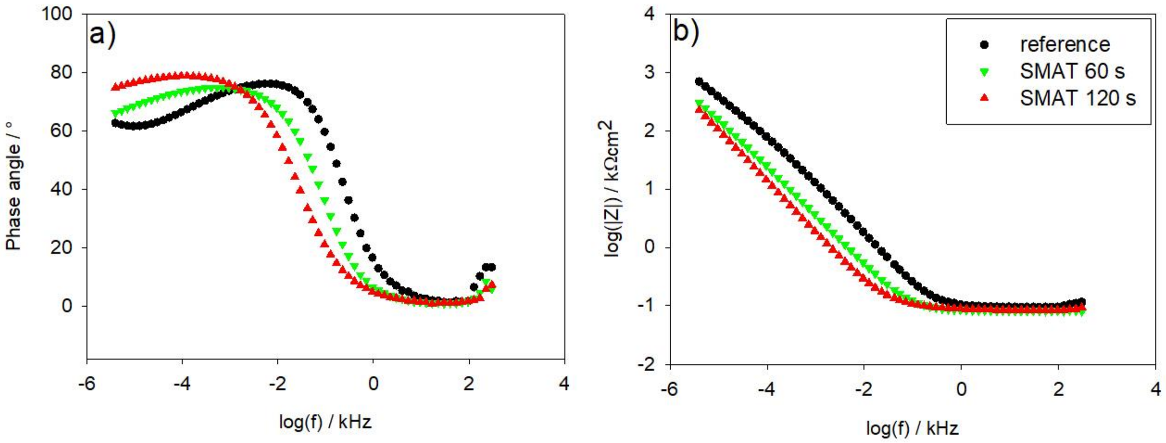

Figure 9.7 Impedance spectra of the as-received SMATed and reference samples: a) phase angle, and b) logarithm of modulus of impedance log(|Z|) versus the logarithm of frequency log(f).

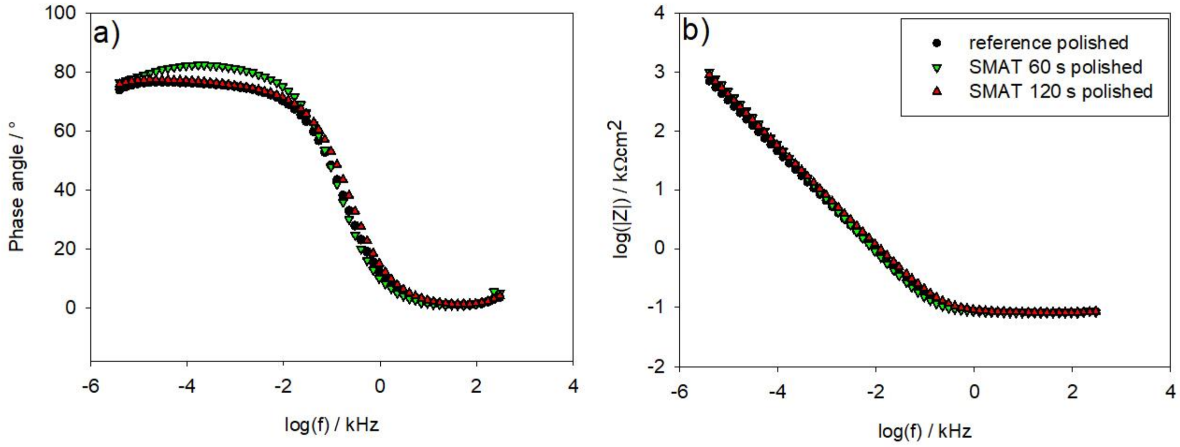

Figure 9.8 Impedance spectra for the polished SMATed and reference samples: a) phase angle, and b) logarithm of the modulus of impedance log(|Z|) versus the logarithm of frequency log(f).

As it can be seen in Fig. 9.7 b) and 9.9, at low frequencies, the logarithm of modulus of impedance Z suggests that the corrosion resistance of the material is the highest for the reference sample and the lowest for the sample SMATed for 120 s. However, according to the definition of the polarization resistance as the limit value of resistance at a frequency approaching zero, the interpolation of these curves to lower frequencies gives the highest polarization resistance for the sample SMATed for 120 s and then SMATed for 60 seconds, as can be seen in Fig. 9.10.

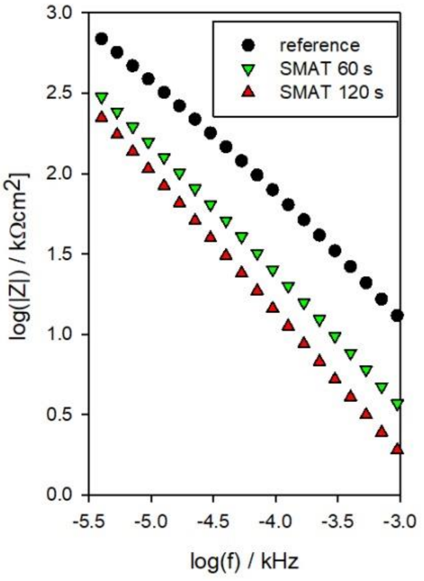

Figure 9.9 Logarithm of modulus of impedance *Z* versus the logarithm of frequency f in the range of low frequencies for polished SMATed and the reference samples.

For the polished samples, log(|Z|) values in the range of low frequencies are higher for the SMATed specimens than for the reference sample, as can be seen in Fig 9.8 b). As can be seen in Fig. 9.8 a), the phase angles in the range of low frequencies are almost constant for the polished samples. A shift in the phase angle values in the range of low frequencies indicates a decreased capacitive influence in the electrochemical behavior of the sample [18]. It is more visible for the as-received samples. All polished samples exhibit much higher values of log(|Z|) in the range of low frequencies which indicate their nobler electrochemical response, in comparison to as-received ones. It can be seen from the impedance data presented in Fig. 9.7 and Fig. 9.8 that the systems show capacitive behavior over a relatively wide-frequency region. It is typical for passive systems. The plot of the log(|Z|) versus log(f) is practically a straight line for all samples in the intermediate range of frequencies. It indicates that the oxide layer is being continuously sealed. In the high-frequency region log(|Z|) values are almost frequency independent and the phase angle approaches nearly 0°. This indicates a response of solution resistance.

There is a little difference in the shapes of the profiles of log(|Z|) and phase angle for all samples in all frequency ranges, except for the reference sample, as seen in Fig 9.7. Comparing the data for as-received samples and the polished ones, it can be seen that the experimental points in Fig. 9.8b are arranged along one curve.

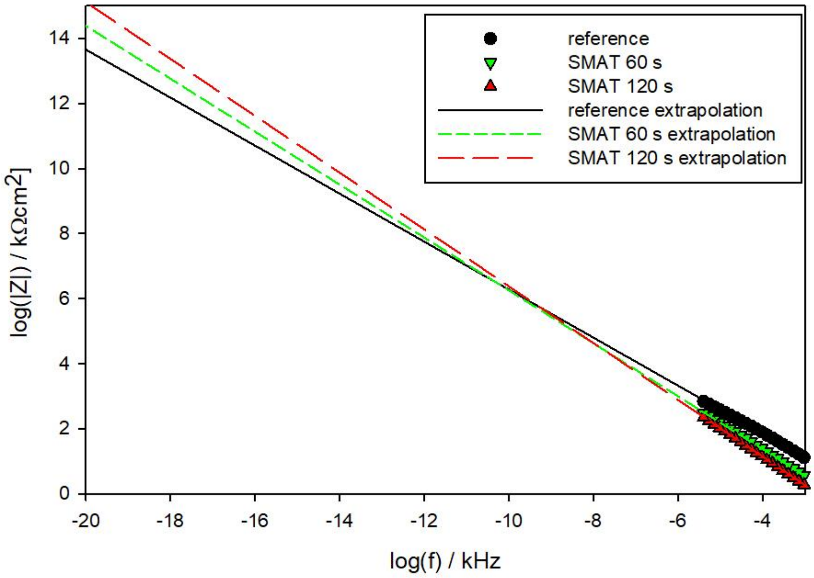

Figure 9.10 Logarithm of modulus of impedance Z versus the logarithm of frequency f in the range of low frequencies for the as-received SMATed and the reference sample.

The EEC used for fitting the impedance data is shown in Fig. 9.11 The EEC consists of resistance elements, *R* and CPEs *Q*. This EEC is commonly used to simulate data for Ti in a saline solution [19]. According to the model used, the passive film on the titanium surface composes of two layers: an outer porous layer and an inner barrier layer underneath it. In the present model R_s, R_T and R_c represent solution resistance, the porous barrier resistance, and the inner barrier layer resistance, respectively. CPEs Q_1 and Q_2 correspond to the capacitance of the barrier layer and the capacitance of the double layer, respectively. The impedance Z_{CPE} of CPE can be expressed by [20]:

$$Z_{\text{CPE}} = \frac{1}{2\pi f_0 C_0}\left(\frac{f_0}{if}\right)^{\alpha}, \tag{9.3}$$

where i is the imaginary unit, f_0 is the frequency of reference (assumed 1000 Hz), f is the frequency, C_0 is the capacitance at the frequency of reference, and α is a coefficient which is close to 1 for an ideal capacitor and it usually ranges between 0.7 and 1.0 in the case of a non-ideal capacitance. For the EEC showed in Fig. 9.11, the polarization resistance R_p, i.e., the parameter characterizing the susceptibility of the material to corrosion, can be calculated from the formula:

$$R_p = R_T + R_C. \tag{9.4}$$

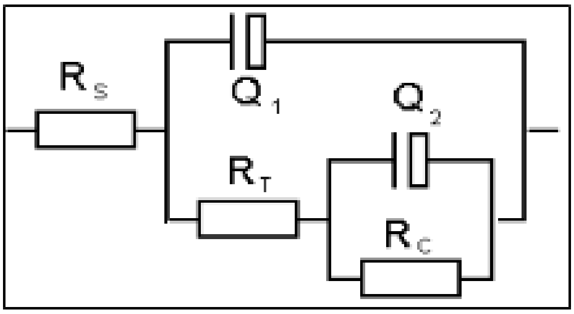

Figure 9.11 EEC applied in the interpretation of the data from electrochemical impedance spectroscopy measurements.

The Minuit program based on a complex nonlinear regression least-square fitting procedure was used to fitting the EEC model used to the measured data [21]. The quality of the fit can be seen in Figs. 9.12 and 9.13, which show the example of the fits to measured data for the as-received SMAT 120 s sample using the EEC depicted in Fig. 9.11. Values calculated by the fitting program are marked by the crosses while experimental data is represented by the empty circles. The quality of the fit is also determined by the standard deviation s:

$$s = \sqrt{\frac{\sum_{k=1}^{n}\left(\frac{\left|z_{i,\text{measured}} - z_{k,\text{fitted}}\right|}{\left|z_{k,\text{measured}}\right|}\right)}{k-1}}, \tag{9.5}$$

where Z_i is the impedance at the frequency number k and n is the number of frequencies in the impedance spectrum.

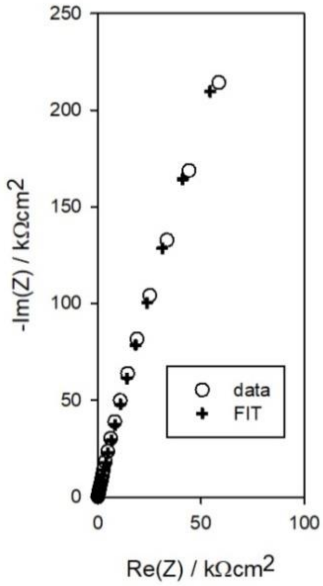

Figure 9.12 Example of the fit to the measured data for the as-received SMAT 120 s sample – Nyquist plot. Values calculated by the fitting program are marked by the crosses while experimental data is represented by the empty circles.

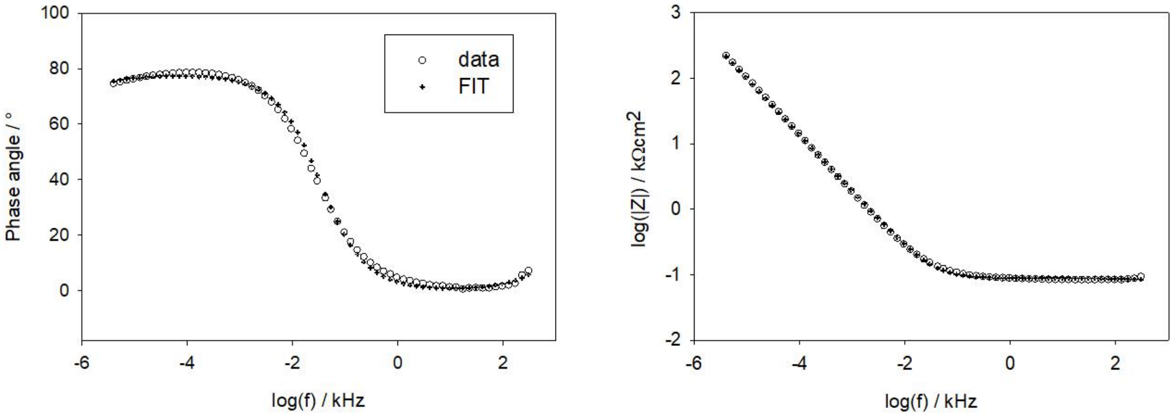

Figure 9.13 Example of the fit to measured data – Bode plots. Values calculated by the fitting program are marked by the crosses while experimental data is represented by the empty circles.

The results of fitting the EIS spectra for the as-received samples after 24 hours of immersion in 0.15 mol dm^{-3} NaCl are gathered in Tab. 9.3 which summarizes the results of the most representative series of measurements. Three of such series were made, during which commonly observed variations in obtained results occurred. Differences in results of the corrosion measurements with nominally identical materials were reported by, e.g., op't Hoog [22]. However, polarization resistance values $R_{p,\ reference} < R_{p,60s} < R_{p,120s}$ for the as-received samples and $R'_{p,\ reference} < R'_{p,60s} < R'_{p,120s}$ for polished samples were always preserved. The SMAT process strongly influenced the R_p of titanium.

It can be seen that values of the porous layer resistance, R_t, as well as, the inner barrier layer resistance, R_c, increase with the SMAT duration for the as-received samples. The value of $R_{t,120s}$ increases even by one order of magnitude in comparison to the value of $R_{t,reference}$ for the reference sample. Nevertheless, the value of the porous barrier resistance is negligible in comparison to the resistance of the inner barrier layer resistance for all samples, and practically it does not have any effect on the polarization resistance of titanium samples. The polarization resistance of the as-received SMATed Ti samples increased at least threefold in comparison to the reference sample.

Polishing the samples led to an overall increase in corrosion resistance. This is understandable because polishing resulted in a smoother surface finish in comparison to the as-received samples which resulted in the reduction of the effective surface that was exposed to the electrolyte during the EIS tests. Polishing made it possible to obtain surfaces in the same state, with roughly the same thickness of the oxide layer before the immersion in the electrolyte. This is reflected in almost the same values of the porous barrier resistance R_t calculated for the polished SMATed and reference samples. In the case of the sample SMATed for 120 s, the resistance of the inner barrier layer, and thus the polarization resistance $R'_{p,120s}$, increased threefold in comparison to the reference sample. While for the sample SMATed for 60 s, the twofold increase in resistance $R'_{p,60s}$ is observed in comparison to the reference sample.

An increase in corrosion resistance of USSP cp titanium in the electrolyte similar to this applied in the present study, i.e., Ringer's Solution was reported by Agrawal et al. [23]. These authors peened titanium with fairly similar conditions to those applied in the present study, i.e., with the treatment time of 30, 60, 90, 120 s, using 3 mm steel balls at the fixed frequency of 20 kHz and the amplitude of 80 μm. They attributed better corrosion resistance of USSP titanium to the enhanced formation of a passive oxide protective film due to the presence of a large number of grain boundaries on the surface of Ti. However, Jindal et al. [24] reported a drastic decrease of corrosion resistance of USSP cp titanium in Ringer's Solution in comparison to the non-treated specimen. These authors treated titanium with 8 mm steel balls at a frequency of 50 Hz for 45 min. They linked a decrease in the corrosion resistance of peened titanium, which occurred despite nanostructured surface, to inhomogeneity in dislocation density and residual stresses at the surface which hindered the formation of the uniform oxide layer. It can be seen that the different corrosion responses in the two aforementioned cases are due to different surface roughness, the density of crystal lattice defects, and the magnitude of residual stresses. So in the case of SMAT or USSP, the peening parameters have a great influence on the corrosion resistance of the treated material.

It can be seen that despite the rougher surface (specified by the parameter R_a in Chapter 9.3.1) of as-received titanium SMATed for 120 s is more corrosion resistant than the sample SMATed for 60 s. It is noteworthy that increased roughness is connected with a larger surface area of the sample that is exposed to the electrolyte during EIS measurements. Increasing the surface of the electrode is associated with a decrease in its resistance. Both as-received and polished specimens owe better corrosion resistance, in comparison to corresponding references, to a larger number of nucleation sites for passive film formation, i.e., grain boundaries, dislocations, and twins. The presence of such structural inhomogeneities was confirmed by the EBSD picture and the PALS measurements in Chapters 9.3.2 and 9.3.4 respectively. The better corrosion resistance of the as-received and the polished samples SMAted for 120 s, in comparison to the ones SMATed for 60 s coincides also with a slightly higher value of the shorter positron lifetime and its slightly higher intensity which is related to a higher dislocation density.

The obtained results indicate the positive effect of the SMAT on the corrosion resistance of the titanium samples. Increasing simultaneously both the SMAT duration and the vibration amplitude causes an increase of polarization resistance of titanium which resulted in its more noble corrosion behavior. The results show also that even after removal of the original oxide layer formed during contact with air, the microstructure that was created in the samples promotes the formation of a tight barrier layer on their surface. This, in turn, results in superior corrosion resistance in comparison to the corresponding reference sample.

Table 9.3 Results of the electrochemical experiments carried out on Ti samples subjected to SMAT duration 0, 60, and 120 s in 0.15 mol dm^{-3} NaCl solution.

sample	R_t **[Ωcm^2]**	R_c **[MΩcm^2]**	R_p **[MΩcm^2]**
reference	143.7	1.53	1.53
SMAT 60 s	167.2	4.84	4.84
SMAt 120s	190.1	5.29	5.29
reference polished	181.5	8.61	8.61
SMAT 60 s polished	180.4	13.6	13.6
SMAT 120 s polished	179.5	22.1	22.1

9.4 Summary

The applied experiment methods made it possible to study gradient microstructure in grade 2 titanium created by SMAT with different parameters of the process. Titanium was treated for 60 s and 120 s, with vibration amplitudes 13 ± 2 μm and 27 ± 2 μm, respectively. SMAT caused an increase in the surface roughness of titanium specimens. Processing with the SMAT increased the roughness parameter R_a from about 1 μm for the reference sample to 1.65 μm and 3.07 μm for 60 s and 120 s of SMAT duration, respectively.

The crystallite size determined by XRD is lower than 100 nm which confirms the refined microstructure induced by SMAT. A significant decrease in the grain size close to the surface for the sample SMATed for 120 s and then gradually increase of their size with increasing distance from the treated surface is visible in the EBSD image. While the microstrain for the sample SMATed for 60 s is negligible, the microstrain value for the sample SMATed for 120 s is evidence of a significant local distortion of crystal lattice planes. The considerable difference in the microstrain between the two samples studied is corroborated by the difference in the microhardness measured as close to the surface as a dozen of micrometers. This indicates that plastic deformation of the surface layer of titanium caused by 60 s of SMAT with sonotrode amplitude of 13 μm is much smaller than that caused by SMAT with these processing parameters twice as high. In the case of magnesium, this difference was not so pronounced which is connected to the dissimilarity of mechanical properties of these two metals despite their common hcp crystal structure which implies similar mechanisms of plastic deformation.

PALS measurements enabled the determination of the total depth of the SMAT affected layer in titanium samples. A significant increase in the mean positron lifetime values in comparison to the bulk was observed, which indicated a large number of lattice defects introduced by SMAT. At the surface, the mean positron lifetime takes similar values for both samples. In the case of specimen SMATed for 60 s, the mean positron lifetime decreases with the distance from the treated surface and reached the values for the reference sample at the depth of about 250 μm, which can be treated as the total range of SMAT induced changes. For the sample SMATed for 120 s, the shape of the positron lifetime depth profile is slightly different than for sample SMATed 60 s. After an initial decrease near the surface, the mean positron lifetime increased reaching its maximum at the depth of about 180 μm. After that, positron lifetime decreased to the depth of about 400 μm, which can be considered as the total depth of SMAT induced changes.

Two positron lifetime components were derived from positron lifetime spectra for both samples. The presence of a longer component indicated the presence of vacancy clusters containing about 3 or 4 vacancies. The shorter positron lifetime component was attributed to the annihilation of positrons trapped at dislocations or when its value decreases deep in the sample also to the annihilation of positrons in the regions free of defects. For the sample SMATed for 60 s, the shorter lifetime, τ_1, decreased to the values slightly higher than the reference lifetime already at the depth of 30 μm at which the longer component intensity exhibits a maximum. The longer component disappears at a depth greater than 200 μm. In the case of Ti SMATed for 120 s, the values of the first component remained almost constant up to the depth of about 150 μm, then it decreased with the increasing depth from the treated surface to the value obtained for the reference sample. The intensity of the longer component increased initially and after reaching a maximum it decreased and disappeared at the depth of 350 μm.

For both samples, the distance from the surface at which the shorter component of the positron lifetime approaches the value for the reference defect-free samples coincides with the depth at which the microhardness comes near its reference value. This indicates that the increase in microhardness is connected mainly to the increase in dislocation density. The presence of vacancy clusters does not affect significantly the microhardness. The vacancy clusters are present at the distance from the treated surface at which the induced strain is much smaller than close to the surface. It may be connected to the deformation mechanism of titanium which at high strain deforms mainly by dislocation slip and at low strain by twinning.

EIS measurements indicated the positive effect of the SMAT on the corrosion resistance of the titanium studied. Increasing simultaneously both the SMAT duration and the vibration amplitude resulted in more noble corrosion behavior of titanium samples. The results show also that even after removal of the original oxide layer that was formed during the SMAT, the microstructure created in the sample surface layer promotes the formation of a tight, corrosion-resistant barrier layer on their surfaces. This, in turn, translates to superior corrosion resistance in comparison to the corresponding reference sample. The better corrosion resistance of the as-received and the polished samples SMAted for 120 s, in comparison to the ones SMATed for 60 s coincides with a slightly higher value of the shorter positron lifetime and its intensity which is related to a higher dislocation density.

References

1. J. Kansy, Nucl. Instrum. Methods Phys. Res. A 374 (1996) 235.
2. M. Jamesh, T.S.N. Sankara Narayanan, P.K. Chu, et al. Front Mater Sci 7 (2013) 285.
3. Y. Zhu, Y. Guan, Z. Wang, et al. Surf. Coat. Technol. 317 (2017) 38.
4. L. Zhu, Y. Guan, Y. Wang, et al. Int. J. Adv. Manuf. Technol. 89 (2017) 1451.
5. K. Zhu, A. Vassel, F. Brisset, et al. Acta Mater. 52 (2004) 4101.

6. M. Wen, G. Liu, J.-f. Gu, et al. Appl. Surf. Sci. 255 (2009) 6097.
7. S. Bahl, B.T. Aleti, S. Suwas et al. Philos. Mag. 98 (2018) 2095.
8. O. Unal, A.C. Karaoglanli, R. Varol, et al. Vacuum 110 (2014) 202.
9. M.Wen, G. Liu, J. Gu, W. Guan, et al. Surf. Coat. Technol. 202 (2008) 4728.
10. L. Zhu, Y. Guan, Y. Wang, et al. Int. J. Adv. Manuf. Technol. 89 (2017) 1451.
11. F. Lukáč, J. Čížek, J. Knapp, et al. J. Phys. Conf. Ser. 674 (2016) 012007.
12. J. Yli-Kauppila, P. Moser, H. Kiinzi, et al. Appl. Phys. A 27 (1982) 31.
13. J. Čížek, O. Melikhova, Z. Barnovská, et al. J. Phys.: Conf. Ser. 443 (2013) 012008.
14. H.L. Chan, H.H. Ruan, A.Y. Chen, et al. Acta Mater. 58 (2010) 5086.
15. A.Y. Chen, H. H. Ruan, J. Wang, et al. Acta Mater. 59 (2011) 3697.
16. N. M. Nancheva, K. Saarinen, G. S. Popov, Phys. Stat. Sol. (a) 95 (1986) 531.
17. J. Dryzek, M. Wróbel, Tribol. Lett. 55 (2014) 413.
18. I.Miloseva, G. Zerjava, J.M.C. Morenob, et al. Electrochim. Acta 99 (2013) 176.
19. J. Pan, D. Thierry, C. Leygraf, Electrochim. Acta 41 (1996)1143.
20. W. Simka, M. Mosiałek, G. Nawrat, et al. Surf. Coat. Technol. 213 (2012) 239.
21. F. James, M. Roos, Comput. Phys. Commun. 10 (1975) 343.
22. C. op't Hoog, N. Birbilis, Y. Estrin, Adv. Eng. Mater. 10 (2008) 579.
23. R.K. Agrawal, V. Pandey, A. Barhanpurkar-Naik, et al. Ultrasonics, 104 (2020) 106110.
24. S. Jindal, R. Bansal, B.P. Singh, et al. J. Oral Implantol. 40 (2014) 347.

Chapter 10: Thermal stability of nanocrystalline materials

The problem of thermal stability of NC materials limits their potential applications and narrows possible processing techniques. During past years, the thermal stability of SMATed materials has attracted the attention of researchers [1-4]. The literature results show that the thermal stability of the materials depends strongly on the properties of the material itself. For example, pure NC metals may experience drastic grain size growth even at room temperature [5], while nanometer grains of alloys with precipitates are more stable [1]. Annealing of defects is connected to changes in microstructure and properties of materials. Positron annihilation can shed light on the thermal stability of crystal lattice defects created in the material during plastic deformation.

The following Chapter presents the results of studies of the thermal stability of NC materials produced by SPD techniques. PAS technique was used to evaluate the thermal stability of SMATed grade 2 Ti and AISI 316L stainless steel. For comparison purposes, specimens of Ti were pressed in a uniaxial hydraulic press and the additional samples of NC Ti were prepared by HE.

10.1 Methods

PALS measurements were performed with the ^{22}Na isotope using the fast-fast spectrometer based on BaF_2 scintillators with a time resolution of 270 ps. The analysis of the obtained spectra with more than 10^6 counts was made with the LT program [16].

DB spectra were measured at room temperature using HPGe detector with 1.2 keV energy resolution at 511 keV.

10.2 Titanium

10.2.1 Sample preparation

Samples of SMATed grade 2 titanium were cut from the same plate, whose preparation process has been described in Chapter 9.

Additional samples of grade 2 titanium were prepared with the use of the HE method. HE is the production method of the bulk NC materials, which consists of extruding the metal billet through a die by a liquid pressure [7]. During such a process, the dimensions of the shaped element are reduced. When the stress in the billet exceeds the value of the material’s yield strength and frictional resistance is overcome, the plastic deformation process begins. Then the billet is extruded through the die hole [8]. HE application results in the production of ultrafine-grained and NC metals.

Grade 2 titanium specimens were prepared in form of rods of 10 mm in diameter, in one HE pass (specimens denoted as nTi), and by the combination of HE and rotary forging (specimens denoted as gTi). The research materials were prepared at the Institute of High Pressure Physics UNIPRESS of the Polish Academy of Sciences. The parameters of the process are gathered in Table 10.1. The rods were cut by a low-speed metal saw to obtain the samples for the positron annihilation measurements in the form of 2 mm thick cylinders. Both rod and saw blade were water-cooled. The samples were etched in an acidic solution of 85%H_2O + 10% HNO_3 + 5% HF to remove the surface layer deformed during cutting.

Other samples of grade 2 titanium were compressed in a uniaxial hydraulic press up to 12 % of thickness reduction.

Samples were subjected to an isochronal annealing process with a step of 25 °C and an annealing time of 1 h. After each step of annealing, the samples were cooled with the furnace, and the PALS measurements were performed at room temperature. The annealing was performed in the flow of nitrogen gas.

Table 10.1 Parameters of the HE process.

sample	pressure [MPa]	diameter reduction
nTi	1120	517 %
gTi	1060	310 %

10.2.2 Results and discussion

Figure 10.1 shows the dependence of the S-parameter on the temperature of isochronal annealing of titanium specimens prepared by the HE method. The positron lifetime values measured for the initial samples are gathered in Tab. 10.2. For both samples, only one lifetime component was sufficient to obtain in deconvolution of the spectra with χ^2 close to unity. The difference in the positron lifetime values points out some difference in the defects caused probably by different methods of deformation. Both values are close to those reported for dislocations in titanium [11]. For comparison, there is also shown the dependence for the sample compressed in the uniaxial hydraulic press. The level of deformation of this sample was chosen in such a way so that the value of the S-parameter was similar to the NC titanium samples. However, in this case, the positron lifetime spectrum deconvolution gives two distinct components. The shorter one is slightly shorter than the lifetime for dislocations which may indicate that in addition to positrons annihilating localized at dislocations there is some contribution from positrons annihilating in regions free of defects. The longer component is characteristic for vacancy clusters with intensity similar to that registered for the SMATed samples. However, the mean positron lifetime, 183 ps, is slightly lower than registered for them.

Table 10.2 Positron lifetime values measured for the initial samples of Ti prepared by HE and compressed in the hydraulic press.

sample	gTi	nTi	Ti compressed (12%)	
lifetime [ps] **intensity [%]**	176(1) 100	169(1) 100	166(1) 87.3(1.3)	300(8) 12.7(1.3)

In the case of HE titanium, it can be seen that the values of the S-parameter for both nTi and gTi specimens start to decrease above 100 °C. This decrease is more pronounced for the gTi sample for which it starts from the higher value. It takes place up to 225 °C. For annealing temperatures between 225 °C and 350 °C, the S parameter remains almost constant. For the sample nTi, this decrease is much smaller but in the end, the S parameter values for both samples are similar in the temperature range between 225 °C and 325 °C. Then a sharp decrease of the S-parameter is visible for both specimens to the temperature of about 500 °C. Annealing above this temperature does not cause significant changes.

In the case of compressed titanium, the S-parameter behaves quite differently in comparison to those obtained for HE titanium. Above 100 °C, a sharp decrease in the S-parameter is visible up to 250 °C. Then a gradual decrease of the S-parameter is observed up to the temperature of about 475-500 °C, above which it remains roughly constant.

The dependencies of the S-parameter on the annealing temperature can be compared with that obtained by Serra and de Diego for titanium deformed by rolling (28% thickness reduction) [10]. They distinguished partial recovery which took place at 400 °C for which the positron lifetime drops from the initial value of 194 ps to 167 ps and the second stage of recovery or recrystallization when the positron lifetime decreases further to the bulk value at 850 °C. The sample gTi shows similar behavior. There is a visible partial recovery, the temperature range of roughly constant S-parameter values, and a final decrease of the S-parameter. The main difference is that in the present studies, the temperature at which the bulk value of the S-parameter is reached is much lower, i.e., about 500 °C. This temperature may be treated as indicating the second stage of recovery or recrystallization. This discrepancy may be connected to different annealing regimes or the temperature at which the deformation was performed. Serra et al. deformed their samples at -20 °C. In the present case, the deformation took place at room temperature and the annealing step was much lower, i.e., 25 °C comparing to 100 °C in ref. [10], therefore, the total annealing time was much longer.

The first stage in the present measurements may be related to the annealing of some defects with longer positron lifetimes. This stage is hardly visible for the nTi sample which exhibited the shorter initial positron lifetime. It is most pronounced for the compressed sample for which the positron lifetime revealed the presence of vacancy clusters. According to Hood et al., vacancies in Ti migrate already at 250 K and they create vacancy clusters, which dissolve at 300 K [11]. It seems that the steep decrease of the S-parameter marking the first stage of recovery is caused mainly by the disappearance of vacancy clusters. The density of dislocations after this stage indicated by the values of the S-parameter is much lower for this sample than for two HE samples. The PAS studies of annealing behavior of NC titanium obtained by HE indicate that dislocations induced by plastic deformation are stable to about 350 °C.

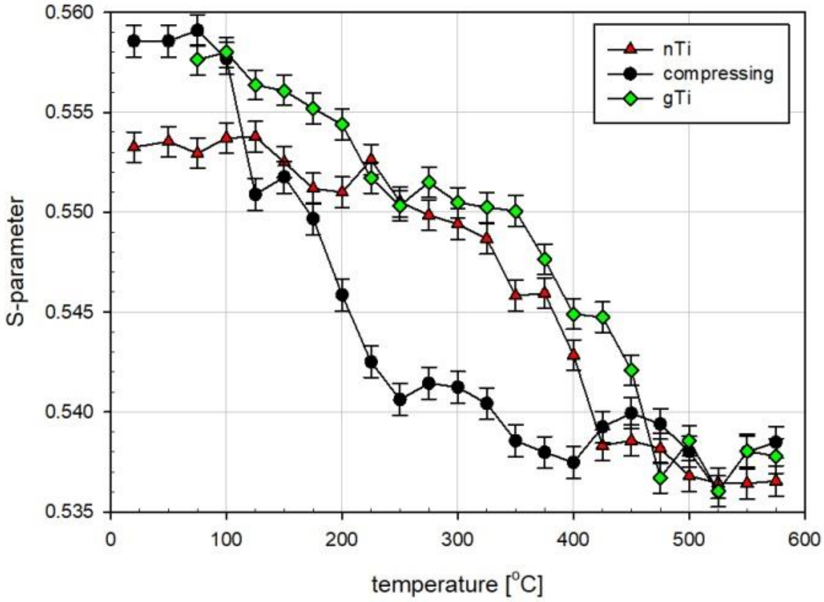

Figure10.1 Temperature profiles of the S-parameter measured for the HE and the compressed specimens of Ti.

Measurements analogous to those for HE titanium were performed for the SMATed titanium. Figure 10.2 presents the dependence of the mean positron lifetime as a function of temperature in the process of isochronal annealing of the SMATed titanium specimens. The obtained temperature dependencies of the mean positron lifetime are similar for both SMATed specimens. The mean positron lifetime takes the highest values for the as-received samples, and then it decreases with the increase in the annealing temperature to the value close to that obtained for the reference sample. It can be seen that the decrease of the mean positron lifetime progresses in two steps. The first step is when it starts to decrease in the temperatures ranging from 100 °C to 200 °C. Then, for both samples, a more gradual decrease of the mean positron lifetime is observed to the temperature of 325 °C. Above this temperature, the registered mean positron lifetime for both samples approaches the value obtained for bulk Ti ~ 144 ps (see Chapter 9). Because it is still slightly higher than 144 ps, it seems that some dislocations, which influence positron annihilation, are still present in the samples.

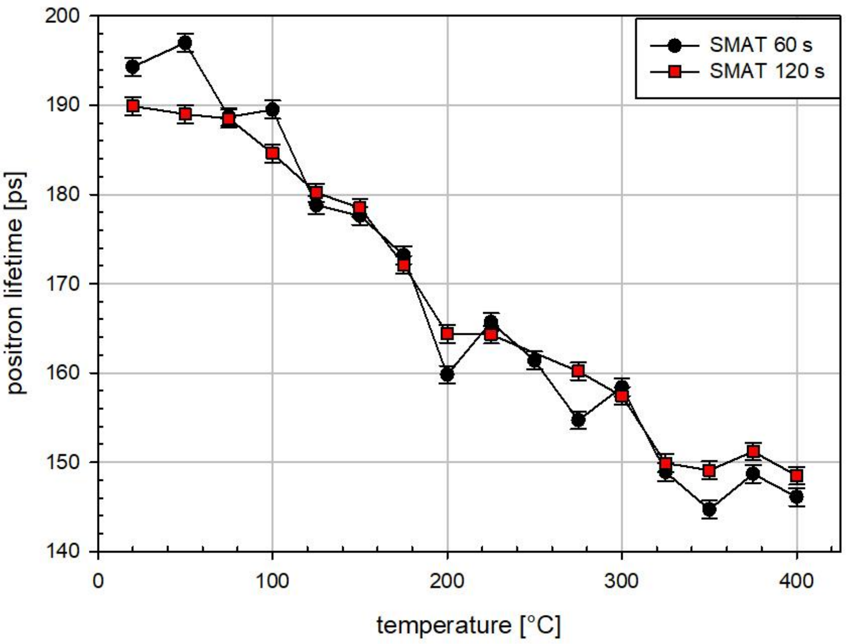

Figure 10.2 Mean positron lifetime in the function of temperature during isochronal annealing measured for SMATed specimens of Ti. Solid lines are the guide for an eye.

Two components in the positron lifetime spectra, described by their lifetime values τ_i and intensities I_i for i =1,2, were observed for both samples. Their behavior also indicates two stages distinguished in the mean positron lifetime temperature dependency. Figure 10.3 presents the dependencies of the lifetime values of these components and the intensity of the longer component I_2 as the function of temperature ($I_1 = 1 - I_2$, expressed as a percentage). Analysis of the behavior of the positron lifetime components indicates that for both SMATed specimens, the shorter lifetime τ_1 (Fig. 10.3 b)), behaves similarly, and starts to decrease from about 176 ps, after annealing at 50 °C. Then its values remain fairly stable, up to the temperature of 150 °C. Then, another decrease in values of τ_1 is observed between 175 °C – 200 °C. Above this temperature, τ_1 takes the values in the range 146 - 154 ps. The longer lifetime τ_2 exhibits some spread around 300 ps with some decreasing tendency when the annealing temperature increases (Fig. 10.3 a)). The intensity of this component, I_2, exhibits some increase reaching its maximum of about 20% after annealing at 100 °C (Fig. 10.3 c)). Then after annealing at higher temperatures, I_2 sharply decreases to about 5%. Above 300 °C, the second component disappears.

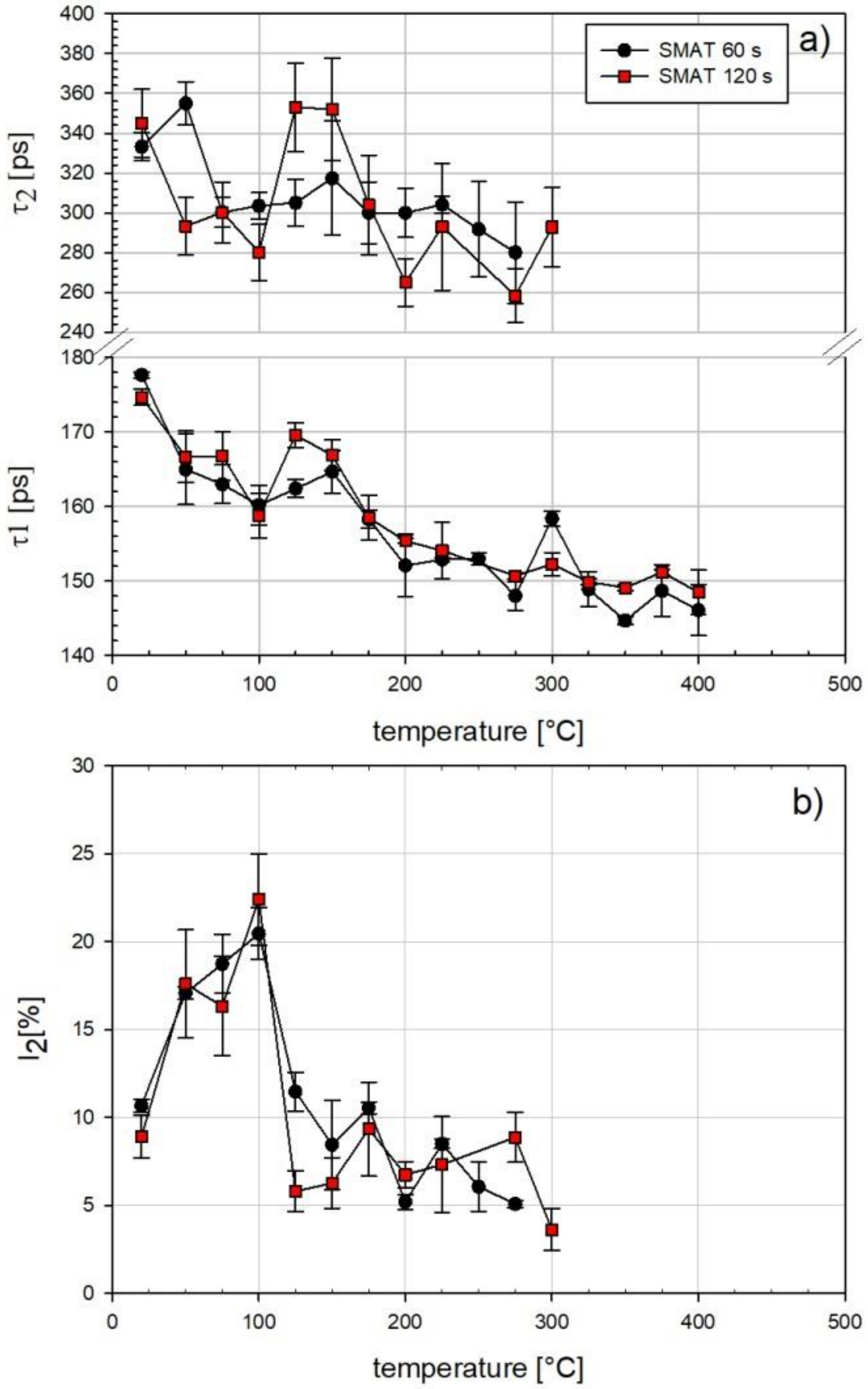

Figure 10.3 Temperature dependencies of the positron lifetime components, τ_2 (a), τ_1 (b), and intensity I_2 (c), of the longer component ($I_1 = 1 - I_2$) obtained from the deconvolution of the positron lifetime spectra measured for the SMATed Ti.

The dominant deformation mechanism of titanium, as well as other hcp metals, is mechanical twinning. However, interfacial dislocations are also being introduced by slip transmission of matrix dislocations through the twins [12]. The shorter component can be attributed to the annihilation of positrons trapped at dislocations [11]. At higher annealing temperatures, its values are intermediate between those characterized for dislocations and bulk material. The LT program failed to resolve these two annihilation channels. Decrease in τ_1 indicates that more positrons annihilate in the undisturbed crystal lattice. Then the volume fraction of the regions without dislocations increases as a result of the recovery of the deformed material. The longer lifetime component originates from the annihilation of positrons trapped in vacancy clusters containing about 3 or 4 vacancies according to the theoretical calculations performed by Čížek et al, [13]. The increase of its intensity at low annealing temperatures points out an increase in the number of clusters. The following sharp decrees denote the dissolving of the major part of the vacancy clusters. However, some small amount of vacancy clusters is retained up to 300 °C.

By combining data from Figs. 10.2 and 10.3 the two stages of defect annealing can be distinguished. The first one takes place in the temperature ranging from about 100 - 125 °C to about 200 °C. In this range of temperature, a rapid decrease in the values of the mean positron lifetimes for both samples is visible. The values of mean positron lifetime decrease for both specimens from about 190 ps to about 166 ps. The shorter component, which was attributed to the annihilation of the positrons trapped in the dislocations, remains fairly stable up to 150 °C. The second stage of defect annealing starts at 225 °C. It can be seen that the mean positron lifetime above this temperature decreases more gradually in comparison to its decline in the first stage. The component, attributed to dislocations, remains roughly at the same level in the remaining temperature range, for both samples. The longer component decreases gradually with increasing temperature and disappears after annealing at 275 °C, marking thus, the annealing of most of the point defects. Similar behavior of positron annihilation parameters during isochronal annealing of NC titanium was reported by Kwon and Kim [14]. They observed two-staged annealing of crystal lattice defects in cold-rolled high purity titanium during isochronal annealing. The reported by them peak temperatures of the first and seconds stage ranged between 150-200 °C and 450-500 °C respectively. However, there should be taken into account the fact that for high purity metals, the kinetics of recovery and recrystallization may differ from that for commercial purity metals.

It is interesting to compare the presented above results with those obtained by Zhang et al. [15]. They studied the annealing properties of SMATed commercial purity titanium using microhardness measurements and optical observations of the cross-sectional microstructure. They concluded that the surface layer has certain heat stability when it is annealed below 350 °C. Surprisingly, it fits very well with the result for NC HE titanium samples. The compatibility with the PALS results for the SMATed samples is a bit worse. However, in the case of the SMATed samples, the presence of vacancy clusters obscures the whole picture as it does for the compressed sample.

What is more, the PALS results may shed light on the reported in ref. [15] result that the corrosion resistance of their samples at 150°C was better than that of the as-received SMATed cp-titanium. On the other hand, it arises from the PALS studies, that at this temperature the number of vacancy clusters significantly decreases. However, the confirmation of the influence of vacancy clusters in plastically deformed titanium on corrosion resistance requires further research.

10.3 AISI 316L stainless steel

10.3.1 Sample preparation

The specimen 100 mm × 100 mm × 4 mm in dimensions was cut from a sheet of AISI 316L stainless steel. Before SMAT, the specimen was annealed at 400 °C in a vacuum (~10^{3} Pa) for half an hour and then slowly cooled inside the furnace to room temperature. SMAT was carried out for 60 s and 120 s with the same parameters, as described in Chapter 7.1. After SMAT, the plate was cut into smaller pieces 10 mm × 10 mm in size.

Samples were subjected to an isochronal annealing process with a step of 25 °C and an annealing time of 1 h. After each step of annealing, the samples were cooled with the furnace, and the measurements were performed at room temperature. The annealing was performed in the flow of nitrogen.

10.3.2 Results and discussion

Only one positron lifetime was resolved in the measured positron lifetime spectra. One of the possible explanations for this is the presence of crystal lattice defects with similar positrons lifetimes. The finite time resolution of the spectrometer used did not allow them to be distinguished. The obtained lifetime values can be treated as the mean positron lifetime $\bar{\tau}$.

Figure 10.4 shows the dependence of the mean positron lifetime as a function of temperature in the process of isochronal annealing of SMATed AISI 316L steel. The value of the mean positron lifetime measured on the surface of the specimens are equal to 159 ± 1 ps and 165 ± 1 ps for specimens SMATed for 60 s and 120 s respectively. These values of the mean positron lifetimes are comparable with those for positron annihilating trapped at vacancies in dislocation line [16]. They are much higher than those obtained for the LSP steel (~135 ps) in Chapter 8 which indicates higher plastic deformation of the subsurface layer.

The obtained temperature dependencies of the mean lifetime are similar for both SMATed specimens. In the initial stage of heating, up to 200 °C, the value of the lifetime does not change for both SMATed samples. Then a gradual decrease in the value of the lifetime is visible up to 475°C, at which it reaches a value close to this obtained for the reference sample annealed for 1 h at 1000 °C in the flow of nitrogen, i.e., τ_{bulk} = 107 ± 1 ps (see Chapter 8.3). However, after annealing at this temperature, the mean positron lifetime is still slightly higher than for the reference indicating the presence of some residual dislocations.

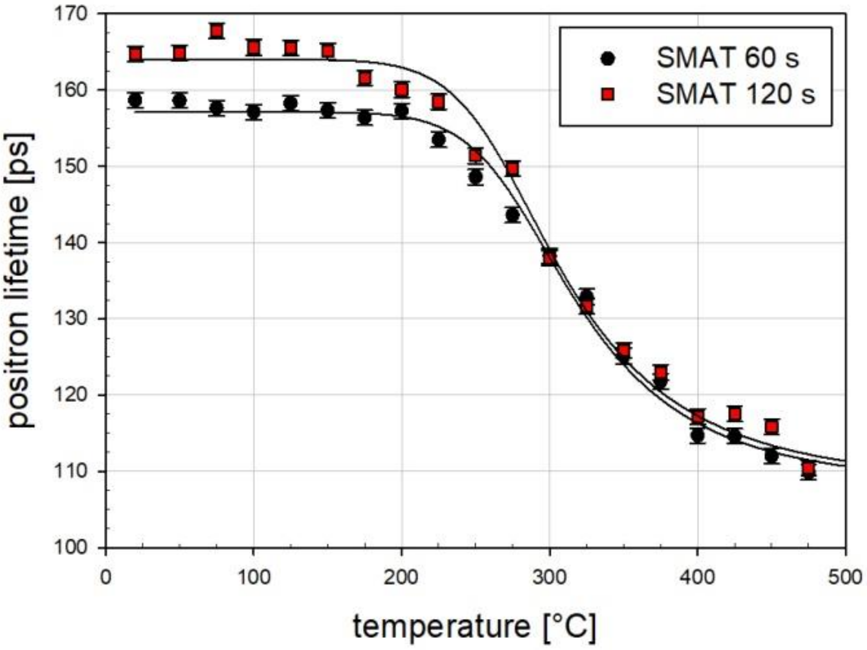

Figure 10.4 Mean positron lifetime in the function of temperature during isochronal annealing measured for SMATed specimens of AISI 316L stainless steel. Solid lines are the guide for an eye.

It can be concluded that the decrease in the mean positron lifetime value for temperatures greater than 200°C observed in Fig. 10.4 is related to a decrease in the concentration of defects in the material during annealing. It can be assumed that the decrease in the mean positron lifetime is connected mainly to the annealing of vacancy type defects (migration of vacancies to the grain boundaries) which were generated during plastic deformation, while some dislocations are still present.

The positron lifetime value close to the bulk lifetime indicates that the dislocation density is low. It may be connected also to the presence of grain boundaries. It should be noted that the dependencies depicted in Fig. 10.4 are very similar to those obtained by Sarnek for NC steel 316L deformed by single cold HE [17]. Then, the thermal stability of SMATed steel is similar to those prepared by HE.

Summary

In the case of HE and compressed specimens of titanium two stages of defect annealing were distinguished. During the first stage, defects with longer positron lifetimes, i.e., vacancy clusters were annealed. It may correspond to the first recovery state. This stage is hardly visible for the nTi sample because the concentration of vacancy clusters for this sample is lower than for other samples as indicated by the mean positron lifetime value. It is most pronounced for the compressed sample for which the positron lifetime revealed the presence of vacancy clusters. The steep decrease of the S-parameter marking the first stage of defect annealing is caused mainly by the disappearance of vacancy clusters. The density of dislocations after this stage indicated by the values of the S-parameter is much lower for this sample than for two HE samples. The PAS studies of annealing behavior of NC titanium obtained by HE indicate that dislocations induced by plastic deformation are stable to about 350 °C.

Two positron lifetime components were resolved for the SMATed titanium. The first component was attributed to the annihilation of positrons trapped at dislocations. The second, longer component originated from the annihilation of positrons trapped in vacancy clusters containing about 3 or 4 vacancies. The process of defects annealing also takes place in two stages. However, the mean positron lifetime behavior is in between of those observed for the HE titanium and the compressed titanium samples. The first stage for both SMATed and compressed specimens was characterized by a much greater decrease in positron annihilation characteristics than in the case of HE samples. The second stage of defect annealing was characterized by the gradual decrease of annihilation parameters for both SMATed and compressed samples, while for the HE Ti more rapid decrease in annihilation characteristics was observed.

The measurements of the mean positron lifetime as a function of temperature in the process of isochronal annealing made it possible to study the temperature stability of SMATed AISI 316L steel. The obtained temperature dependencies of the mean lifetime were similar for both SMATed specimens. The decrease of positron lifetime values above 200 °C marks the decrease in the concentration of defects in the material during annealing. However, after annealing at 475 °C the mean positron lifetime is still slightly higher than that for the well-annealed reference sample indicating the presence of some residual dislocations.

References

1. W. Liu, C. Zhang, Z. Yang, et al. Appl. Surf. Sci. 292 (2014) 556.
2. H.-W. Chang, P.M. Kelly, Y.-N. Shi, et al. Surf. Coat. Technol. 206 (2012) 3970.
3. R. Huang, Y. Han, J. Alloys Compd. 554 (2013) 1.
4. Y. Liu, B. Jin, J. Lu, Mater. Sci. Eng. A 636 (2015) 446.
5. A.K. Giri, K.A. Darling, S.M. Walsh, Structural power, energy, actuation, and mobility in intelligently directed systems enabled from nanocrystalline metals, in S.M. Walsh, M.S. Strano (eds.): Woodhead Publishing in Materials, Robotic Systems and Autonomous Platforms, Woodhead Publishing, 2019, 449-474.
6. J. Kansy, Nucl. Instrum. Methods Phys. Res. A 374 (1996) 235.
7. L. Guo, H. Yang, Deformation Rules and Mechanism of Large-Scale Profiles Extrusion of Difficult-to-Deform Materials, in S. Hashmi, G.F. Batalha, C.J. V. Tyne, B. Yilbas (eds.): Comprehensive Materials Processing, Elsevier, 2014, 291-319.
8. H. Garbacz, K. Topolski, M.Motyka, Hydrostatic extrusion, in H. Garbacz, I.P. Semenova, S. Zherebtsov, M. Motyka (eds): Micro and Nano Technologies, Nanocrystalline Titanium, Elsevier, 2019, 37-53.
9. F. Lukáč, J. Čížek, J. Knapp, et al. J. Phys.: Conf. Ser. 674 (2016) 012007.
10. A. Serra, N. De Diego, Phys. Stat. Sol. (a) 110 (1988) 409.
11. G. M. Hood, R. J. Schultz, J. A. Jackman, Radiat. Eff. 90 (1985) 149.
12. X. Tan, H. Guo, H. Gu, *et al. Metall Mater Trans A* 29 (1998) 513.
13. J. Čížek, O. Melikhova, Z. Barnovská, et al. J. Phys.: Conf. Ser. 443 (2013) 012008.
14. H.I. Kwon, I.S. Kim, Scr. Metall. Matter. 32 (1995) 607.
15. C. Zhang, X. He, X. Lan, et al. Mater. Sci. Forum 695 (2011) 162.
16. E. Kuramoto, T. Tsutsumi, K.Ueno, et al. Comp. Mater. Sci. 14 (1999) 28.
17. M. Sarnek Ph.D. Thesis, IFJ PAN Kraków 2016.

Thesis summary

The main aim of the presented thesis was to examine gradient microstructures with the top nanocrystalline layers produced in commercial purity magnesium, grade 2 titanium using SMAT, and in 316L stainless steel using LSP. The samples were subjected to SMAT with two sets of processing parameters: with the duration of 60 s and the vibration amplitude of 13 µm, and with the duration of 120 s and the vibration amplitude of 27 µm. The increase of both the process duration and the vibration amplitude caused the increase of the energy imparted to the surfaces of the specimens. The PAS methods were combined with microhardness tests, EBSD, XRD, surface roughness tests with the use of the optical profilometer, and corrosion resistance tests to evaluate the impact of SMAT and LSP on the properties of the materials studied.

In the case of magnesium, it was found that SMAT causes an increase in the dislocation density and grain refinement, which increases the hardness of the subsurface zone. The mean positron lifetime values indicate that positrons are trapped in vacancies on dislocation lines and dislocation jogs. A twofold increase in both the duration and the vibration amplitude of SMAT influences the shape of the obtained depth profiles of the mean positron lifetime, which reflects the induced defect depth distribution. In the case of the sample SMATed for 120 s, the plateau of the high mean positron lifetime values extended from the surface to the depth which coincides with the thickness of the highly deformed layer revealed by EBSD. Such plateau was not observed for the shorter SMAT duration with the lower vibration amplitude. However, the influence of the processing parameters on the total depth of defect distribution or the hardened layer was small.

Electrochemical measurements have shown that the microstructure induced by SMAT increases the susceptibility of magnesium to anodic oxidation, which leads to the increased formation of a hydroxide layer with passivating properties on its surface and, consequently, translates into better corrosion resistance compared to the reference sample. This was confirmed by the VEP measurements which indicated a thicker oxide layer formation on the surface of the sample SMATed for 120 s.

PALS measurements made it possible to examine microstructural changes induced by LSP in AISI 316L steel. Obtained values of the mean positron lifetime indicated the creation of clusters of two to five vacancies that were formed near the irradiated surface. The VEP beam results enabled the estimation of the dislocation density near the treated surface which was of the order of 10^{14} m^{-2}. The XRD analysis revealed the formation of martensite in the tested samples.

The experimental methods used made it possible to study the gradient microstructure in titanium created by SMAT with the same processing parameters as were used in the case of magnesium. A significant increase in the mean positron lifetime was observed compared to the reference sample, which indicates a large number of lattice defects introduced during SMAT. Two positron lifetime components were distinguished in the positron lifetime spectra. The longer component indicated the presence of vacancy clusters of approximately 3 or 4 vacancies The shorter component was attributed to the annihilation of positrons trapped in dislocations or, when its value decreased at a larger distance from the treated surface, also to positron annihilation in defect-free regions. For both samples, at some depth, there is present a layer with a higher concentration of vacancy clusters. It occurs inside the material at the depth for which the dislocation density is low. For the sample SMATed for 120 s, the vacancy cluster layer is shifted deeper in comparison to specimen SMATed for 60 s. It is connected to the fact that unlike for magnesium, the defect distribution in titanium treated for 120 s is almost twice as deep as that in titanium treated for 60 s.

The EIS measurements showed a positive effect of SMAT on the corrosion resistance of the tested titanium. The simultaneous increase in both the SMAT duration and the vibration amplitude resulted in better corrosion resistance compared to the shorter treatment time.

As it was mentioned above, for the SMATed magnesium and titanium as well as for the LSP steel 316L, PAS allowed the determination of the total range of the subsurface layer affected by the treatment. It is worth mentioning that to my knowledge, defect distributions in the deformed layer created by SMAT in magnesium and titanium have not been determined before. The total depth of the layer with the defects induced is more than twice larger for magnesium in comparison with titanium. Moreover, one can find some common features of the defect distributions found in the SMATed magnesium and titanium, and these materials subjected to sliding friction. It may be explained by the fact that in both cases a large amount of plastic deformation is localized within a small volume of material close to the surface.

Additionally, the temperature stability of the SMATed titanium samples and those prepared with the use of HE and compressed using a hydraulic press were studied. For this purpose, the measurements of the S parameter and the mean positron lifetime as a function of temperature in the isochronal annealing process were carried out. Two stages of defect annealing were distinguished for the titanium specimens. The first stage is connected to the disappearance of vacancy clusters and takes place between 150 °C and 200 °C. It is especially visible for the samples for which the vacancy cluster concentration indicated by the intensity of the longer positron lifetime component is higher, i.e., for the compressed and SMAted samples. For the HE samples, for which the vacancy cluster concentration is low, the second stage of the defect annealing is visible as a sharp decrease of the positron annihilation characteristics at temperatures above 350 °C. For the SMATed samples, the second stage has the form of a gradual decrease of the mean positron lifetime.

The influence of SMAT on the properties of materials studied, especially their corrosion resistance was studied. The final results show the correlation between the defect concentration and corrosion resistance of the materials studied. The surface nanocrystallization methods used improved the corrosion resistance of magnesium and titanium.